UNIVERSITÀ DEGLI STUDI DI PALERMO
Dottorato in Scienze Molecolari e Biomolecolari
Dipartimento Scienze e Tecnologie Biologiche Chimiche e Farmaceutiche (STEBICEF)

Settore Scientifico Disciplinare SSD CHIM/09

Advanced electrospun matrices based on polysaccharide derivatives for applications in regenerative medicine

IL DOTTORE
SALVATORE FEDERICO

IL COORDINATORE
CH.MA PROF.SSA PATRIZIA DIANA

IL TUTOR
CH.MA PROF.SSA GIOVANNA PITARRESI

IL CO TUTOR
CH.MO PROF. FABIO SALVATORE PALUMBO

CICLO - XXXIII
ANNO CONSEGUIMENTO TITOLO - 2021

Index

1. Introduction

1.1 Tissue engineering

The failure of organs and tissues represents common human healthcare problems (Langer and Vacanti, 1993). Classical solving approaches are autologous or allogeneic transplants. Autografts represent a golden standard in some field, like skin regeneration, offering excellent adhesion to host tissues with low rejection risks. Moreover, autographs are expensive, considering lengthy hospital stays, painful, induce scar formation, and the patient's morbidity limits them. Allografts suffer from limited availability, high-risk of immune rejection, and they could represent a transmission route of diseases (Pereira *et al.*, 2013). Tissue engineering is a wide section of regenerative medicine that aims to gain a full or partial repair of organs and tissues damaged from mechanical trauma, congenital diseases, or ageing effect and offers promising solutions to overcome transplant limits, i.e. donor's paucity, producing *in vitro* non-immunogenic organs and tissues. The first definition of tissue engineering belongs to Skalak and Fox (1988), stating as "the application of principles and methods of engineering and life sciences toward the fundamental understanding of structure-function relationships in normal and pathological mammalian tissues and the development of biological substitutes to restore, maintain, or improve tissue function". All regenerative strategies have assumed multidisciplinary principles from medical, biological, nanotechnology, and engineering knowledge exploiting the tricky interaction between advanced scaffolds, cells and biomolecules-mediated stimuli to restore human parts (Gomez-Florit *et al.*, 2020). These three elements are essential to the achievement of Tissue Engineering Regenerative Medicine strategies (TERM); thus, a historical overview of TERM strategies explains the importance of this sentence.

The first approach exploits the use of isolated cells or substitutes. Growth factors-loaded releasing systems can induce a biological response from the tissue, and they have been proposed to overcome the first approach's limitations, like rejection and cellular loss of

activity. A third alternative follows where cells have been seeded in or above biomaterial-based supports (Langer and Vacanti, 1993). Recent advanced strategies exploit scaffolds, cells, and bioactive molecules at once. In all living beings, cells reside in 3D matrices formed by a dynamic network of proteins, which constitute the main anchorage structure for their growth and activity. Native ECM is a dynamic 3D hydrogel composed of fibrous proteins, like collagen, fibrin, elastin, and polysaccharides, such as hyaluronic acid and chondroitin sulphate, heparan sulphate. Different ECM types can exist, depending on collagen and elastin concentration; they can differ for several orders of magnitude of stiffness and elasticity, thus defining different biomechanical functions. Once damaged, the organism spends many resources to induce ECM repair and restore the tissue's homeostasis. The microenvironment influences cells through physical and chemical stimuli locally. Principal factors of such microenvironment are represented by autocrine, endocrine or paracrine secretions, the nano or microscale of the native tissue, mechanical forces, and neighbouring tissues' stresses. Not all tissue can be self-regenerated, like musculoskeletal tissue and some nervous system portions. The impairment of tissues cannot be restored in some pathologic diseases and requires a boost to improve healing or self-repairing ability.

Scaffolds are high-sophisticated devices designed to mimic host tissues. They provide a first biochemical substrate for novel tissue generation inducing cells to produce their extracellular matrix (Bártolo *et al.*, 2008; Xue *et al.*, 2013), resembling a biological impulse for the regeneration. Scaffolds have been classified into different types considering their mechanical strength, stability, composition, porosity degree, and origin. Examples are porous sponges, widely used in bone regeneration, able to host osteoprogenitor cells and osteoblasts with an ideal pore size of 200-350 nm, or fibrous scaffolds with an aligned distribution of fibers for neural or muscular regeneration.

In native ECM, many cell-adhesion proteins play relevant roles in determining cell shape, function, and tissue integrity. The recognition of these proteins occurs by cell-surface

receptors, i.e. integrins. The clustering of integrins on a biomaterial promotes cell survival and proliferation and influences the stem cell fate (Martino *et al.*, 2009). Cell-binding domains are included in scaffolds to improve the cellular adhesion above biomaterial-based devices, as reported in several works (I. L. Kim *et al.*, 2013; Palumbo *et al.*, 2017; Tsaryk *et al.*, 2017).

The primary purposes of scaffolds are cell attachment, providing cellular binding sites, proliferation, and differentiation. These biological functions can be exerted by delivering and sequestering cells and growth factors and ensuring the free diffusion of nutrients, gasses, and waste products through a high-porous structure. Some devices hold additional cues, i.e. self-recruiting features, like chemoattractant release of bio-actives to increase the infiltration and population of a specific cell lineage and, consequently, favouring its expansion and differentiation. *Cell-homing* is the name of this phenomenon, and it can represent an exciting opportunity to increase the damaged tissue's therapeutic outcomes (Pacelli *et al.*, 2017). Cells are sensitive to a plethora of chemical and mechanical signals to manage the proliferative ability, apoptosis, and the start of anabolic or catabolic cellular processes. The chemical stimulation is a standard intercellular communication mediated by soluble chemokines, growth factors, cytokines, cell-adhesive molecules, and other mediators that permit most biological pathways, including self-renewal. Progenitor cells or stem cells can be stimulated to differentiate or "trans-differentiate" outside their lineage by chemical or biological exposure with drugs, chemicals, or biomolecules *stimuli* (Graney, Lurier and Spiller, 2018). The same effect should be artificially guided by the controlled release of these factors or induced by other scaffold properties (Jin, Molamma P. Prabhakaran *et al.*, 2013).

Stem cell therapy aims to treat degenerative diseases, cancer and repair damaged tissue where no other options are available. Moreover, tumour formation and abnormal immune response represent significant risks factors that may be referred to the type of stem cell, the

differentiation status, the proliferation capacity, and the administration route, thus determining the failure of the therapy (Herberts, Kwa and Hermsen, 2011); thus excluding totipotent and pluripotent stem cells. For these reasons, most clinically used stem cells are limited to multipotent cells, e.g. mesenchymal stem cells (MSCs), haematopoietic stem cells (HSCs) and endothelial progenitor cells (EPSs), adipose-derived stem cells (ASCs) isolated from postnatal adult tissues, like blood, bone marrow, adipose tissue or some areas of the brain and spinal cord.

The scaffolds employed for TERM applications should also exhibit an ECM-like architecture with high porosity to promote cell infiltration and growth, a controllable degradation rate, biodegradation, proper strength and stiffness to support mechanical stresses as close as possible to native tissue or organ. For example, MSCs commit to specific phenotypes with high sensitivity to support elasticity. Soft, stiffer, and rigid matrices (elasticity 1, 10, and 100 kPa, respectively) mimic neuronal, muscular, and bone tissues; thus, they induce a neurogenic, myogenic, and osteogenic differentiation of MSCs, respectively (Engler *et al.*, 2006). The cell-sensing ability seems to be attributed to specific myosin isoforms capable of starting a cascade of mechano-transducer and guiding toward a specific lineage specification.

Other relevant properties regard the scaffold's surface, such as a pattern with an interconnected structure to provide cell guidance, alignment and migration, proper surface roughness, charge and wetting properties. Cells can respond to topographical features as small as 5 nm, so it is essential to achieve surface patterns at a nanoscale resolution (Metavarayuth *et al.*, 2016).

An aligned electrospun scaffold of poly-(L-lactide) (PLA) and a randomly-deposed scaffold with the same material have been produced by electrospinning technique and proposed for *in vivo* application as *in situ* tendon regeneration (Yin *et al.*, 2015). Briefly, the aligned fibrous scaffolds promoted tendon-like tissue formation at four weeks post-implantation. In

contrast, the randomly-oriented fibrous scaffold group induced chondrogenesis and subsequent tissue ossification of MSCs at the implantation sites, confirmed by *in vitro* results and histological stainings. The study has highlighted the vital role of the actomyosin cytoskeleton in the lineage commitment of MSCs, and it has illustrated the relationship between topographic cues of the scaffold and tissue formation.

High porosity favours cell infiltration, the transport of nutrients, and the diffusion of regulatory factors. The degradation rate of the support should match the rate of tissue regeneration, encouraging the remodelling of the restored area. The surface properties influence cell adhesion, proliferation, migration and scaffold remoulding. Some biomaterials, like gelatin or collagen, can be enzymatically degraded by cells allowing new tissue deposition. The event determines a loss of the scaffold's mechanical stiffness, which should be supported by the neo-tissue formation (Gaharwar, Singh and Khademhosseini, 2020).

Materials used for the fabrication of scaffolds should also be biocompatible, biodegradable, non-toxic, and they should not activate the native immune system. Regenerative devices are often biomaterials-based scaffolds that can exert multiple structural and biological functions. Biomaterials, also known as “soft-materials”, are extensively used for regenerative medicine and tissue engineering purposes. The main properties of “soft materials” allow proposing innovative and fascinating strategies to resolve unsatisfied therapeutic needs (Chong *et al.*, 2007).

Biomaterials, like biopolymers, have been intended as substances able to interface with physiological systems. They can be obtained from living beings, namely for proteins and polysaccharides, or synthesized and modified in common laboratories, like polymeric derivatives, ceramics, and new alloys. Natural polymers have been often used for these purposes because they can be processed in biodegradable scaffolds, and they do not induce any immune responses in the host. Examples of natural polymers are alginate, collagen,

chitosan, hyaluronic acid, poly(hydroxybutyrate), gellan gum, silk, and most of their chemical derivates, which preserve native biocompatibility (George *et al.*, 2020).

The macromolecular designs of biomaterials guide the adhesion or proliferation of host cells promoting native organ's functionality (Gomez-Florit *et al.*, 2020). The biophysical characteristics of biomaterials, like structure, stiffness, and topography, alter the local microenvironment through changes in pH or temperature and manage the presence of enzymes, cells, ions or radical species (Bettinger, Langer and Borenstein, 2009; Gaharwar, Singh and Khademhosseini, 2020).

The success of bioengineered tissue follows two ways: *ex vivo* and *in situ* method. In the first case, the biodevice has been colonized with patient-derived cells, allowing their growth and expansion before implanting in the host body. The second method regards cell-instructive biomaterials loaded with known biomimetic and chemoactractive molecules (Gaharwar, Singh and Khademhosseini, 2020). Compared to *in situ* regenerations, the primary complications of the *ex vivo* method lie in the need for complex cell culture conditions, expensive, time-consuming procedures, and lower shelf life. The lack of a massive amount of endogenous cells from particular tissues, e.g. cardiac and nervous system, represents another critical limitation for the *ex vivo* approach by determining the method's inability for these purposes.

In situ tissue regeneration can be executed following two strategies:

• Stimulation of endogenous cells via extracellular signals using immunomodulators or bioactives;

• Reprogramming cells fate via intercellular interaction of biomolecules.

In the first case, biomaterials modulate the immune response, facilitating endogenous cell homing and novel tissue development (Figure 1a). Once implanted, serum proteins cover the scaffold by altering its surface and signalling immune cells to secrete pro-inflammatory o anti-inflammatory cytokines or chemokines. In the second case, direct reprogramming of

cells occurs by activating or silencing targeted specific genes at different levels by delivering specific microRNA or mRNA (Figure 1b).

Stimulation of endogenous cells via extracellular signals using immunomodulators or bioactives or via reprogramming cells fate via intercellular interaction of biomolecules.

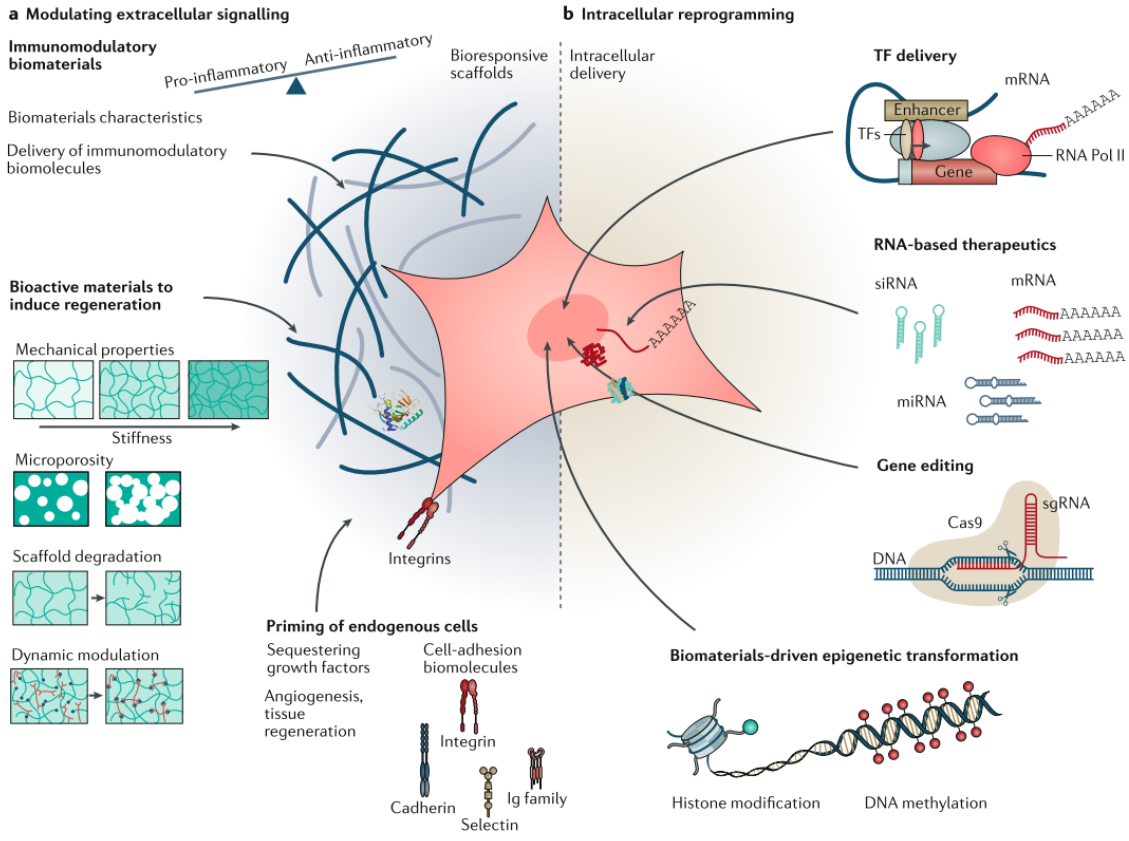

Figure 1. In situ tissue regeneration approaches. a) Extracellular signals with bioresponsive scaffolds; b) Intracellular reprogramming by gene delivery and editing [Gaharwar, Singh and Khademhosseini, 2020]

Several bioactive macromolecules can be included in scaffolds for *in situ* tissue engineering. Growth factors and adhesion proteins allow cell communications guiding their growth, differentiation, migration, metabolism and proliferation as reported in many works; examples are the basic fibroblast growth factor (bFGF) (Delgado-Rivera *et al.*, 2009), the epithelial growth factor (EGF), the vascular endothelial growth factor (VEGF) (Lai *et al.*, 2014), the nerve growth factor (NGF), and the platelet-derived growth factor (PDGF) (Bai *et al.*, 2018). Such incorporation in biodevices improves their biofunctionality. Moreover,

the proper spatio-temporal release in the cellular microenvironment should be achieved to maximize the healing. The inclusion of factors can be executed by physical adsorption (weak interactions), i.e. hydrogen bonds, hydrophobic affinity, encapsulation, or chemical immobilization, introducing solid bonds with the matrices. The physical absorption is a weak interaction, so it causes a burst release of the active. A practical alternative is a direct encapsulation inside the matrix. Otherwise, the chemical approach prevents the washing out of the bioactive agent, and it can establish a predetermined release of signalling molecules according to a specific kinetics (Zhao *et al.*, 2017).

In light of these conclusions, suitable exemplary supports for *in situ* tissue engineering approaches include biomaterial-based scaffolds focusing on nanofibrous membranes, as in-depth described in the following sections.

1.2 Nanofibrous devices for regenerative medicine purposes

The processing of materials in nanofibers is ubiquitous in nature; in fact, natural fibers can be found in plants and animals with relevant structural functions. In tissue engineering, nanoscaled fibrillar scaffolds have been widely used as artificial devices like temporary substitutes, playing a role in controlling the release of active factors or regulating various aspects of cell behaviour (Ogueri and Laurencin, 2020). The loading of active molecules in electrospun nanofibers is performed by adopting different techniques, such as co-axial, multi-jet or co-electrospinning, emulsion, and secondary carrier electrospinning (Sónia P. Miguel *et al.*, 2019).

The high nanofibers surface can also be modified by physical adsorption, layer-by-layer assembly and chemical immobilization of biomolecules, as discussed above. By combining these strategies, the encapsulation of multiple biomolecules can be finely tuned. Depending on the therapeutic role of a biomolecule, the drug release profile can be tailored through the incorporation method used, as illustrated in Figure 2.

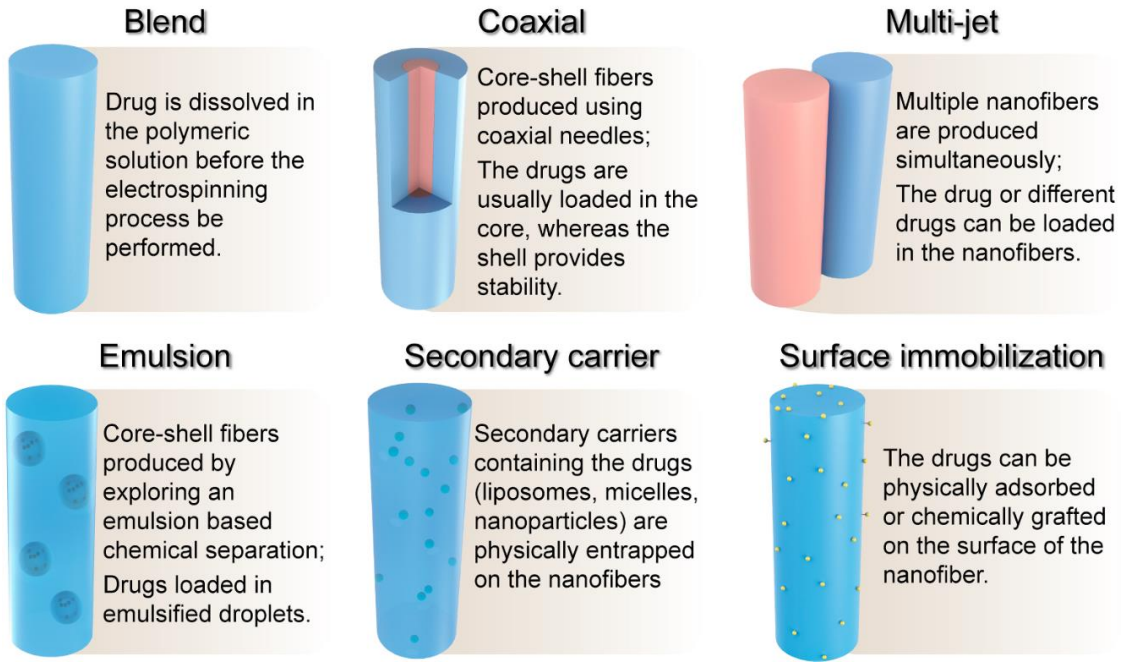

Figure 2. Illustration of most common incorporation strategies of bioactive molecules [Miguel et al. 2019]

For example, the physical adsorption of biomolecules is often associated with burst releases and short diffusion times, whereas the co-axial electrospinning with sustained release profiles. The incorporation of different molecules into nanofibers by the same method generates drug release profiles dependent on each molecule's singular diffusion coefficient. In these cases, the rate of biomolecule diffusion out of the polymeric matrix will be affected by polymer swelling, erosion, dissolution, diffusion or distribution inside the matrix, and drug-polymer weight ratio.

Many methods have been proposed to process biomaterials in nanostructures, such as phase separation, melt-blowing, self-assembly, template synthesis, and electrospinning. Different applications, costs, yield, and dimensional scale of scaffold have distinguished every method. Among them, the electrospinning of biomaterials is one of the most used, with the highest processing yield and an excellent nanometric precision scale.

1.3 Fundamentals of electrospinning (ES)

Electrospinning (ES) is a non-mechanical process for producing non-woven nano fibrillar tissues from polymeric solutions or melts widely used in research and industry for their versatility, scalability, and potential application in different fields. Despite other spinning methods, including microfluidic, ES allows producing nano-scaled fibers with a high area-to-volume ratio and porosity, retained as most relevant features for drug delivery and tissue engineering purposes (Contreras-Càceres *et al.*, 2019).

The most straightforward equipment includes a high-voltage power supply, a syringe pump, a spinneret and a conductive collector. The technique applies a strong electrical tension at the nozzle's tip as a driving force to create a continuous liquid charged jet. Once a polymeric droplet has been experienced such high voltage, it becomes highly electrified under the influence of the electrostatic repulsion of surface charges and coulombic force exerted by the power supply. As results of these forces, the polymer droplet shape changes from spherical to conical named Taylor's cone. The event happens when the electric field overcomes the surface tension of the polymer dispersion, permitting the elongation of the jet. The generation of fibers occurs after stretching, elongation and drying of the jet onto the grounded collector (Liao *et al.*, 2018). The solution's surface tension, needle diameter, and distance between the spinneret and collector influence the critical voltage range to generate nanofibers from the solution.

The diameter and the morphology of fibers depend on several parameters, such as solution's properties, instrumental parameters, and environmental factors (Rahmati et al., 2020). The polymeric solution concentration is a critical factor for the ES process, which determines the viscosity of the solution mainly. Polymer chains entangle very tightly in concentrated solutions. The entanglement is vital for fiber formation during electrospinning, and the concentration at which entanglement occurs is called entanglement concentration. Four regimes can be identified: dilute, semidilute I, semidilute II, and concentrated. Changing

the complex viscosity helps to identify the best viscosity range for electrospinning, as represented in the blue oval in

Figure 3.

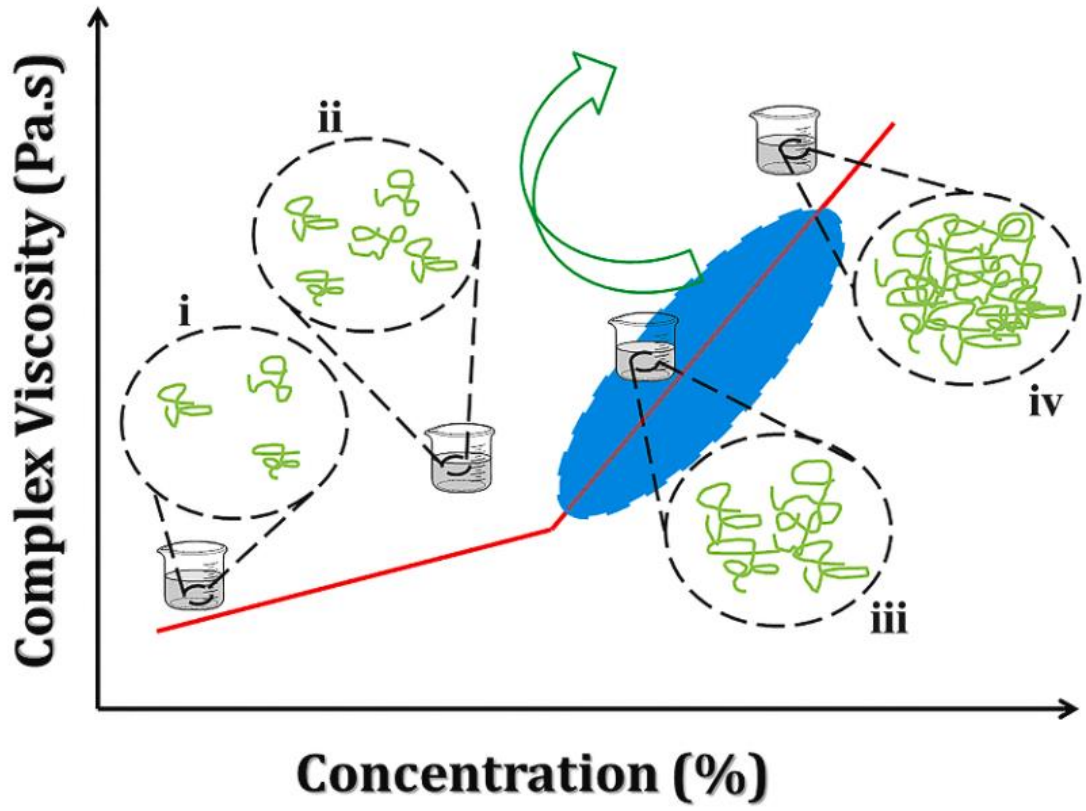

Figure 3. Representation of four regimes of a polymer solution. i) dilute; ii) semidilute I; iii) semidilute II; iv) concentrated solution.[Rhamati et al.,2020]

In dilute and semidilute I conditions, there are no strong interactions between polymeric chains, and the solution does not show viscoelastic behaviour. Beyond the third range, stronger and stronger entangles occur, representing the appropriate value of concentration and complex viscosity of the dope solution showing a viscoelastic behaviour.

Other solution properties regard the molecular weight of the polymer, the surface tension of the used solvent, and the electrical conductivity of the solution. Too low-molecular-weight polymer solutions tend to generate beads instead of fibers, while very high-

molecular polymer solutions produce fibers with a high average diameter. Once the charged jet is formed, the elongation of the jet describes a spiral shape of supercoiled structures which diameter grows over and over due to charge density fluctuations, named as bending and whipping instabilities (Figure 4a).

The low surface tension of the solvent facilitates the desolvation process, while high surface tensions cause jet instabilities, like the Rayleigh axisymmetric instability that results in the splitting of the liquid stream into tiny droplets and then deposed as beads (Figure 4b). The surface tension of the fluid is usually low enough to avoid this Rayleigh instability. The electric field can induce axisymmetric instability (Figure 4c) with decreasing charge density of the solution, which causes the modulation in surface charge density of the jet and forms undesirable beads along the fiber axis (Khalil and Lalia, 2013).

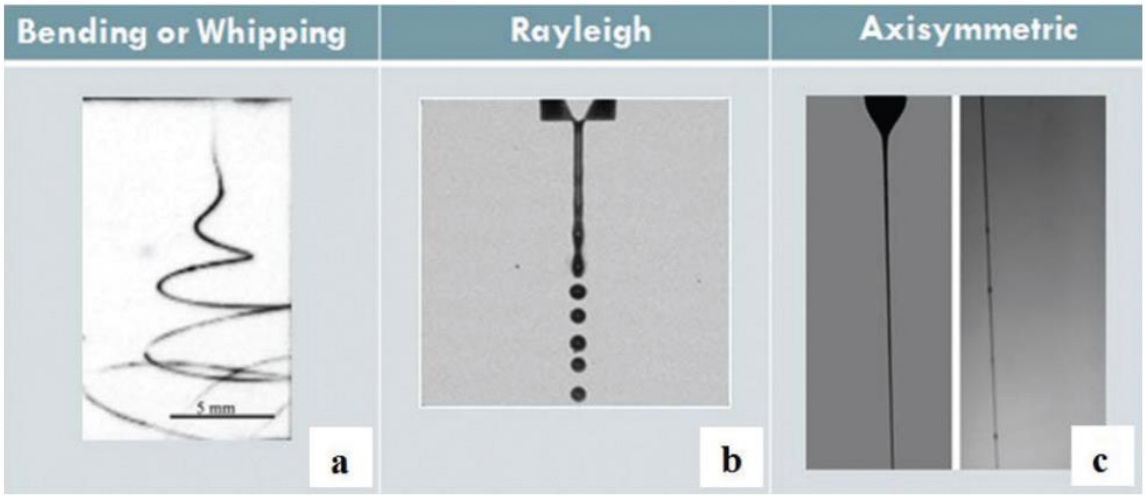

Figure 4. Most common charged jet instabilities during electrospinning processing [Khalil et al., 2013]

It is demonstrated that the average diameter of fibers tends to increase according to the greater conductivity of the solution.

Processing parameters can be resumed as electric field, distances between spinneret and collector, and feeding rate of the solution. The voltage needs to overcome a threshold value to generate fibers; namely, it needs to overcome the surface tension of the polymer solution.

Too high voltages can disrupt the jet in tiny droplets. The feed rate must be tuned according to the solvent evaporation. The complete removal of any traces of solvents occurs by applying a low flow rate or higher voltages.

The relationship between electric field strength value and spinneret-collector distance is an inverse proportionality. The distance between spinneret and collector affects the jet path towards the collector; it should be enough (10-20 cm) to guarantee the adequate solidification time of fibers, avoiding the generation of fused fibers.

Ambient parameters are humidity and environmental temperature. High humidity negatively influences the solidification time and prolongs the charged jetting. The external temperature affects the viscosity of the solution and the morphology of the scaffold. At low-temperature, viscosity increases, favouring the generation of beads, while increasing the temperature reduces the polymer solution viscosity generating tiny fibers (Rahmati *et al.*, 2020).

The collector design also influences the deposition of fibers. Most common collectors are rotating mandrels, flat panels, and patterned collectors. In rotating mandrels, a critical rotational velocity helps the fabrication of aligned fibers. The use of flat panels determines a radially focused deposition of the polymer, while patterned collectors allow reaching predefined geometrical deposition.

Specific TERM applications require the aligned orientation of fibers where scaffold guides the growth of cells along a predefined direction, such as the regeneration of neurites (Koh *et al.*, 2008; Xie *et al.*, 2009; Qu *et al.*, 2013), tendon regeneration(Yin *et al.*, 2015), or in muscle tissue regeneration (Gilbert-Honick *et al.*, 2018). The study of differentiation of C2C12 and H9c2 cell line cultured above supports with different topographical cues (Figure 5) shows how nanofibers permit a faster regeneration of multinucleated myotubes with higher cellular density from the organization of myoblastic (C2C12) and myocardium-derived cell line (H9c2) along the direction of fibers (aligned nF) (Ricotti *et al.*, 2012) than

random fibers (random nF) or cells cultured on the empty flask (polystyrene and flat PHB).

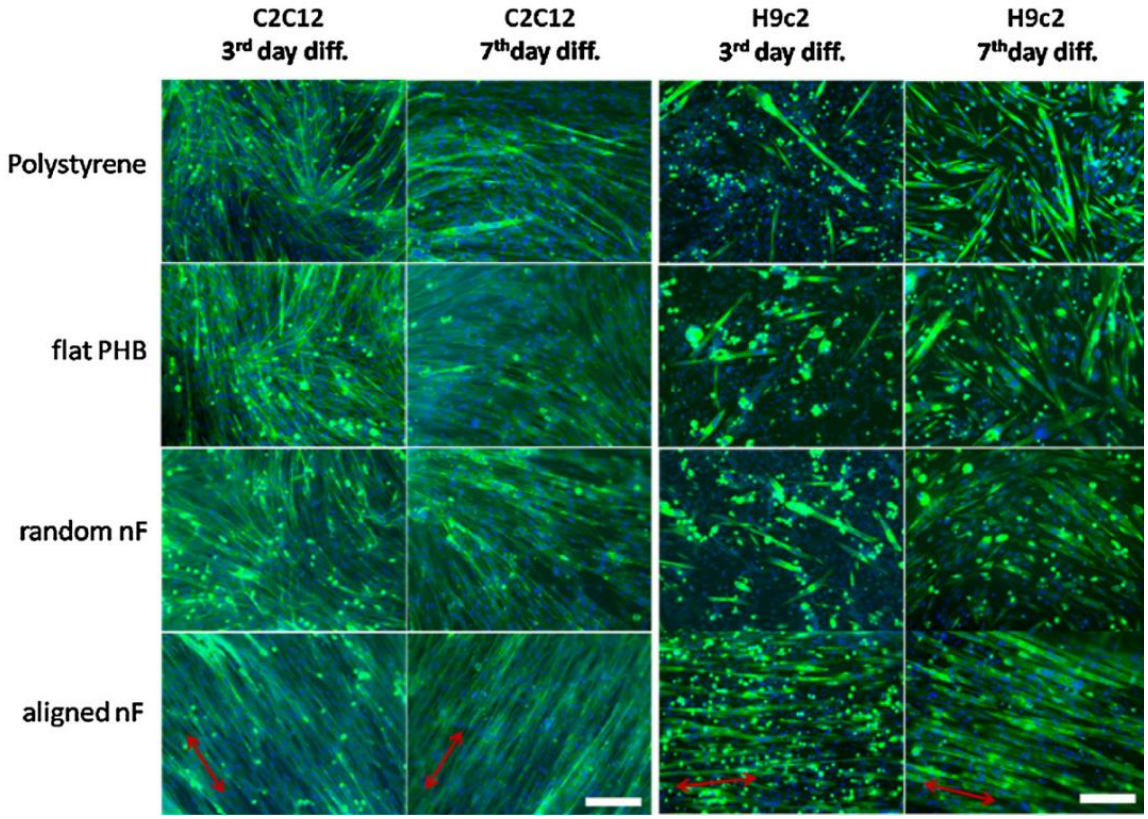

Figure 5. Nuclei and F-Actin staining of C2C12 and H9c2 cells after three and seven days of cell culturing above aligned polyhydroxybutirrate (PHB) nanofibers (nF). Cells are cultured on polystyrene, PHB films, random and aligned nanofibers. The arrows indicate the fiber direction. Scale bar is 200 µm. [Ricotti et al., 2012]

Random fiber orientation is for other biomedical purposes, such as wound dressing, where products are used as bandages (Monteiro *et al.*, 2015; Shan *et al.*, 2015; W. Jiang *et al.*, 2015).

In many works, membranes can be biofunctionalized with therapeutic agents or covered with adhesion proteins to improve the bio-integration in the damaged tissue. Electrospun membranes (EM) have been applied as hemostatic and permeable devices permitting the gaseous exchange, absorbing exudates, for wound dressing purposes (Wang and Windbergs, 2017; Mohammed *et al.*, 2019; Scaffaro, Gulino and Lopresti, 2020) e.g., or they have been employed as delivery systems for bioactive molecules or drugs in the wound area or organs (Meinel *et al.*, 2012; Thakkar and Misra, 2017; Chen *et al.*, 2018; Cheng *et al.*, 2018). The

high biocompatibility of polysaccharides holds several benefits in the TERM field, gaining successful results in many applications, such as dermal (Sheikholeslam *et al.*, 2018), cartilaginous (Coburn *et al.*, 2012), and bone regeneration, or for the reconstitution of more complex organs like liver or heart (Kitsara *et al.*, 2017).

The ES of polysaccharides is as attractive as it is challenging. Successful manufacturing and the use of polysaccharide-based biodevices are reported in the following sections.

1.4 Electrospinning processing of composite biomaterials

Blending biomaterials is a method to increase the processability of materials and improve scaffolds' main features. Different combinations of biomaterials could be better integrated with the host body supplying the damaged tissue closely. Blends can be classified as homogeneous and heterogeneous, considering the miscibility of the components. Miscible blends are clear solutions and show a singular glass transition, while the others are cloudy and exhibit every glass transition of an individual component (Hanumantharao and Rao, 2019).

Homogeneous and heterogeneous blends can be processed by ES generating different scaffold's morphologies. Variant methods for processing multiple materials at once are the co-axial electrospinning or the co-electrospinning of two different solutions using a dual syringe pump system, as reported in Scheme 1.

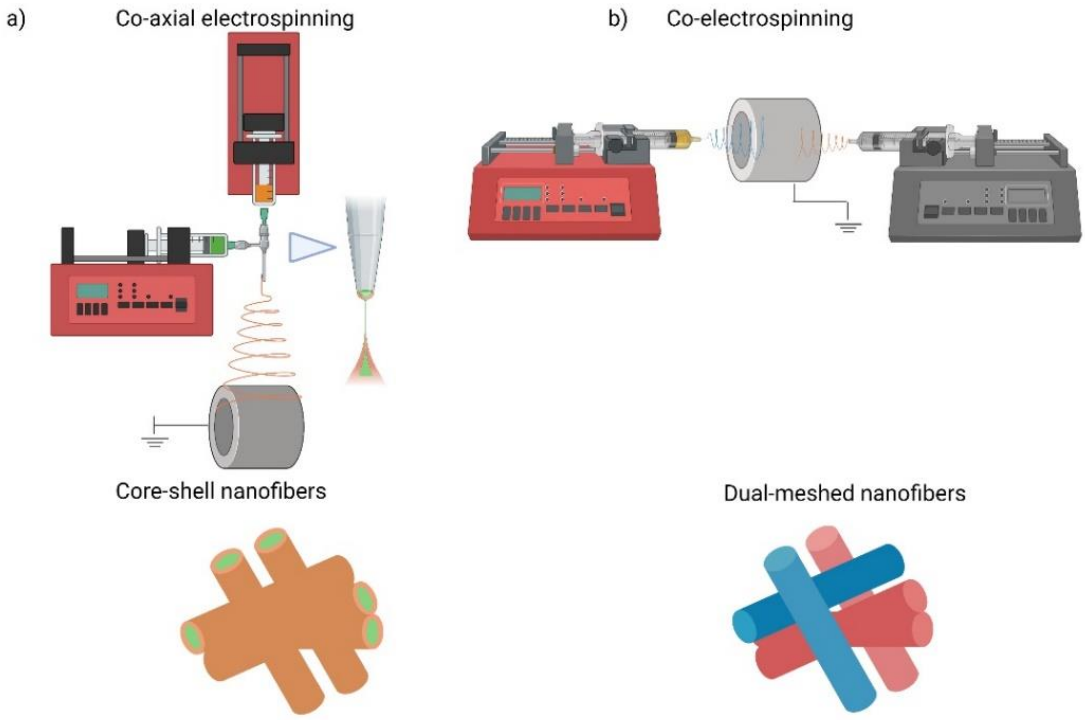

Scheme 1. Illustrative scheme of electrospinning technique. a) Co-axial processing; b) co-electrospinning

Results are core-shell nanofibers in the first case and hybrid meshes in the second one.

The co-axial nozzle processes the core solutions and the shell solution simultaneously in a laminar flow without mixing them. Co-axial electrospinning represents a one-step encapsulation method that can be used to entrap fragile water-soluble bioactive agents, such as growth factors, enzymes, nucleic acids or bacteria in core-shell nanofibers. The co-axial electrospinning permits reducing the direct contact of these agents with organic solvents or avoiding the stress imposed by emulsification processes.

In general, core-shell nanofiber advantages reside in a more sustained release of encapsulated factors over simple electrospun nanofibers offering protection to bioactives during processing and *in vivo* degradation from enzymes of the damaged area. For example, epidermal growth factor (EGF) has been encapsulated in core-shell fibers composed from gelatin solution in a polycaprolactone-based shell and compared to a blended-spinning product using the same materials (Jin, Molamma P Prabhakaran, *et al.*, 2013). Results have

showed the adequate protection of the active from co-axial electrospinning set up and a sustained release of EGF up to 15 days. The scaffold has preserved the bioactivity of EGF, and it has determined the highest differentiation of adipose-derived stem cells to epidermal lineages among the group.

Nanofibrous composites also include fillers, such as graphene oxide, beta-tricalcium phosphate, ferromagnetic nanoparticles, zinc oxide, hydroxyapatite, halloysite nanotubes, or silica, and other inorganic materials able to impart new specific properties to the fibers. These elements can be uniformly distributed in the fiber meshes, or they can decor only the surface. The advantages of incorporating fillers are the generation of chemical bonds to crosslink the membrane, the change in the orientation of polymeric chains, the improvement of mechanical strength, or electrical conductivity. Resuming, fillers can facilitate the electrospinning processing of specific solutions or impart additional features to the final products.

1.5 Asymmetric electrospun membranes

The goal of global research is to offer new advanced scaffolds to better fit with clinical needs. These supports must mimic both the chemical composition and the physical architecture of native ECM to promote cell adhesion, proliferation and differentiation. The hierarchical organization of the musculoskeletal tissues is a clear example of a biological structure with an intrinsic gradient and a specific architecture. For the design of mammalian tissues, anisotropic aspects must be considered during scaffold's fabrication; in fact, it has become popular to exploit heterogeneous structures, namely by controlling the distribution of pore' shape or the molecular organization of the material along a predetermined direction (T. Jiang *et al.*, 2015).

An anisotropic structure exhibits different values of a particular feature, i.e. optical properties, thermal and electrical conductivity, depending on the direction considered; for

example, the compression resistance of a wooden axis varies according to the direction and the side of the application for carrying heavy loads (Mitchell and Tojeira, 2013). One of the most challenging issue for scaffolds regards the control on cell penetration by regulating the pore size distribution and influencing the cell motility rate into the biomaterial network. Topographic anisotropy of constructs also influences cell alignment and functions. Contact guidance refers to the phenomenon that cells adjust their orientation and align along the patterns that they are cultured on (Metavarayuth *et al.*, 2016). The most studied topographical aspect is the roughness of the uppermost layer measured in terms of protrusions or depressions at the surface (Figure 6) by the atomic force microscope (AFM). It is a type of scanning probe microscope able to measure many surface properties with a high resolution at a nanometric scale. The alignment of fundamental units supports the linear adhesion of cells without distortions, maximizing the proliferation.

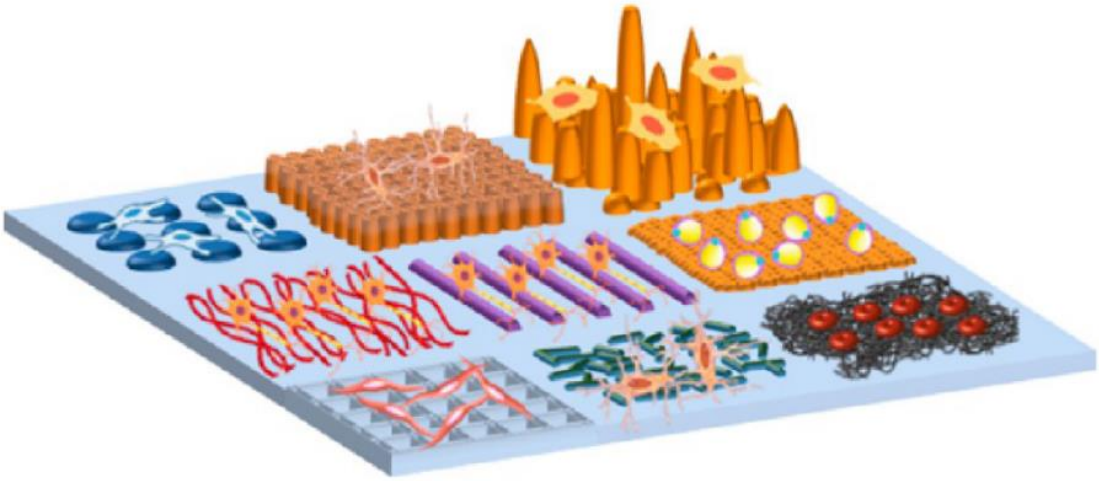

Figure 6. Illustration of cellular interactions with different nanopatterned surfaces [Metavarayuth et al. 2016]

Cells are sensitive to orientation, texture, and physical properties of the adhering structure, such as wettability and mechanical strength. In light of these considerations, anisotropic properties can also be obtained in multilayered composite scaffolds.

Some bilayer skin substitutes products are commercially available, such as Biobrane® (UDL Laboratories, Inc, Rockford, Illinois), Integra® (Integra Life Science Corp, Plainsboro, New Jersey), and Transcyte® (Advanced Tissue Sciences, La Jolla, California), but they are not fully capable of restoring skin native properties.

A next-generation of electrospun scaffolds could be both hybrid and asymmetric, thus employing variegated biomaterials and exploiting top qualities of every component included in the formulation (Morgado, Aguiar-Ricardo and Correia, 2015). For example, multilayered scaffolds can simultaneously exert many functions, e.g. one layer governing the release of active drugs, while the other provides mechanical properties to the whole scaffold and performs control over permeability rate or bioadhesion. Asymmetric membranes have been commonly used for skin regeneration (Sónia P Miguel *et al.*, 2019) as well as for the production of engineered small vessels (Zhang *et al.*, 2013, 2015), mimicking their histological organization. In the case of skin regeneration, two portions can be distinguished such as a very dense outer layer, employed as an infiltration barrier for physical, chemical, and bacterial agents, and a porous structure with high swelling ability able to absorb exudates from wounds preventing any tissue inflammation and debris accumulation. Other requirements of the sub-layers are appropriate pore interconnectivity inside the matrix, water absorption in the range of 100-900% and high wettability, displaying a water contact angle lower than 90°. The water vapour transmission rate (WVTR) of the ideal wound dressing membrane should be around 2000-2500 g/m^2 per day. Commercially available products such as Comfeel $^{(R)}$, Dermiflex $^{(R)}$, Tegaderm $^{(R)}$ are wound dressing devices which do not satisfy such requirement. The permeability of oxygen is also essential for the wound healing process; in fact, the activity of some enzymes which convert O_2 in hydrogen peroxide should be compromised, impairing the restoration of the damaged area. The suitable O_2 permeation is around 450-1850 L/m^2 per day.

Electrospun bilayer membranes have been produced by fabricating a layer with hyaluronic acid and polycaprolactone blend and another one with chitosan, zein, and salicylic acid (Figueira *et al.*, 2016). The HA/PCL dual membrane has been designed with an upper layer providing structural integrity to the whole membrane and a bottom layer exerting bacteriostatic, fungistatic activities and allowing cell adhesion and proliferation of normal human dermal fibroblasts. The electrostatic interactions between the negative charges of the upper membrane (due to carboxyl functions of glucuronic acid residues) and the positive charges of the deacetylated chitosan (derived from amine groups) have provided the adhesiveness of the two-layer. The porosity of the upper layer results lower enough to avoid bacterial contamination (around 90%), while the porosity of the bottom layer favours the cell accommodation and the spreading (around 162%). The combined effect of chitosan and released salicylic acid determines the bacteriostatic activity of the system for up to five days.

Another set of asymmetric membranes can be constituted by hydrogel layers and electrospun layers in a sandwich-like assembling. The modularity permits tuning the size of the scaffold depending on the specific application stacking hydrogel and nanofibers alternatively. For example, adipose-derived mesenchymal stem cells (ASCs) have been incorporated into scaffold based on heparin/fibrin hydrogels and PLGA nanofibers for tendon regeneration (Manning *et al.*, 2013). Nanofibers have been collected on a custom rotating mandrel to mimic the anisotropy of tendon ECM and stacked above a thicker hydrogel. Eleven-layered support has been generated by the repetition of alternative deposition (Figure 7).

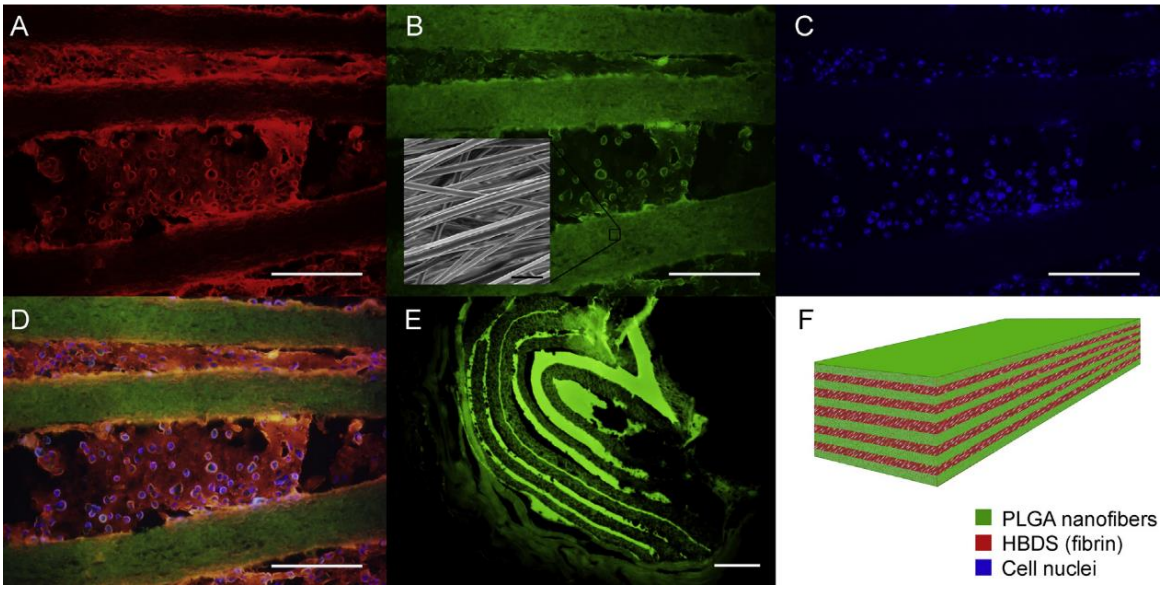

*Figure 7. A representative nanofiber scaffold with 11 alternating layers of aligned electrospun PLGA nanofiber mats separated by heparin/fibrin hydrogel (HBDS)containing 1 * 10^6 ASCs. (A–D) PLGA was labelled with FITC (green), the heparin/fibrin hydrogels were labelled with Alexa Fluor 546 (red), and the ASC nuclei were labelled with Hoescht 33258 (blue) (scale bar = 200 µm). (B, inset) SEM image of the scaffold displaying PLGA nanofiber alignment. (E) Micrograph showing the scaffold in vivo at 9 days after implantation in a tendon repair.); the PLGA was labelled with FITC (green) (scale bar = 100 µm). (F) A schematic representation of the layered scaffold.[Manning et al., 2013]*

The hydrophilic part retains ASCs and the platelet-derived growth factor (PDGF), causing an initial burst release and a following sustained release for up to nine days. The heparin-binding ability and the diffusion limitation through nanofibers have determined the release profile. PLGA nanofibers have improved the handling of the whole scaffold, supporting mechanical stresses and stretches when applied by surgeons. Cells result viable after 9 days after the *in vivo* applications with a scarce expression of inflammation genes. The presence of the growth factor has increased the cellular infiltration, but the phenotype has not been determined.

For constructing a biomimetic vascular microenvironment, nanofibrous asymmetric scaffolds have been proposed with a biomaterial gradient of heparin-chitosan and PCL co-electrospinning (Zhang *et al.*, 2013). The gradient of heparin-chitosan has been exploited to immobilize an increased VEGF amount along the cross-section of the device from the

luminal surface towards the adventitia portion (Figure 8a). Covalent bonding and bioaffinity binding to heparin molecules have established the gradient; thus, they had potentially enhanced the biophysical housing of endothelial cells, favouring both their proliferation and exerting anticoagulation properties. During the first 10 hours, the scaffold has showed a burst release of the GF and has prolonged up to 70 hours. *In vitro* studies have demonstrated the ability of the scaffold to be populated by endothelial cells from luminal side and vascular smooth muscle cells onto adventitia surface with a better infiltration degree with respect to the control with no gradient distribution of VEGF (Figure 8b).

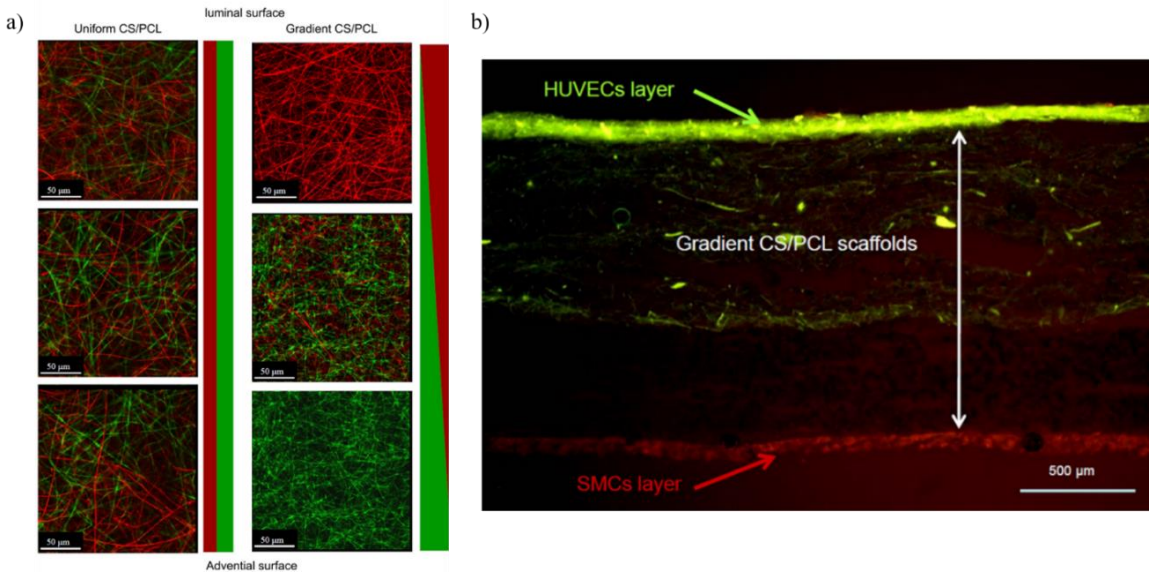

Figure 8. Asymmetric electrospun membrane. a) Laser confocal images along the depth of the scaffold showing the uniform or gradient deposition of heparinized-chitosan (red fibers) and PCL (green fibers) stained with rhodamin and FITC, respectively. Scale bar 50 µm. b) Fluorescent cross-section of cellularized scaffold structure showing HUVEC cell on the lumen surface and vascular smooth muscle cell on adventitia surface. [Zhang et al., 2013]

Anisotropic properties can be achieved by varying the chemical composition of the scaffolds along a direction. The efforts in the design of these products can be beneficial for TERM strategies. It should include a different chemical reactivity of a similar polymer, or blending two biomaterials, including polymers or fillers, modifying their ratio progressively. Recent goals are reviewed in the following sections.

1.5.1 Electrospun membranes based on natural polysaccharides and chemical derivatives

Electrospun nanofibers based on polysaccharides and their derivatives represent a consolidated approach in tissue engineering and regenerative medicine to accomplish advanced biomedical devices for several purposes. Polysaccharides are homopolymers or copolymers of monosaccharides findable in plants, animals, seaweeds and microorganisms. Polysaccharides differ in chemical composition, ionic character and molecular weight influencing their final biomedical applications and electrospinning processing.

Electrospun polysaccharide nanofibers show great potential in many tissue engineering applications despite the more challenging processing conditions required (Mendes, Stephansen and Chronakis, 2017). Polysaccharides can be divided into three categories according to electrospinning performances, the first one can form fibers, the second one forms a jet without fibers, and the third class, which includes most of the polysaccharides, cannot form a stable jet.

Rheological studies have supported this distinction (Stijnman, Bodnar and Hans Tromp, 2011). The intrinsic viscosity [η] is the ratio of a solution's specific viscosity to the solute concentration, extrapolated to zero concentration. It reflects the capability of a polymer in solution to enhance the viscosity of the solution. The intrinsic viscosity [η] is related to hydrodynamic volume V_h by the following equation:

(1) $$V_h = \frac{2}{5}[\eta]M$$

where M is the molar mass of the polymer, one of the most discerning parameters for electrospinning processing. The overlap concentration, c*, represents the transition between dilute and semidilute I unentangled regime, and it has been defined as the concentration inside the hydrated polymer coil of dissolved polymer. It is calculated as follows :

(2) $$C^* = M/ V_h = \frac{5}{2[\eta]}$$

In particular, the reported shear flow rheometry study (Figure 9a), namely the study on the variation of viscosity in dependence of increasing shear rate, shows that the best spinnable polysaccharide blends have a weak shear thinning behaviour at high shear rates (> 100 s^{-1}). Explicative examples are represented by flow curves of 40% w/v dextran solution, 15% w/v pullulan solution, and 50% w/v maltodextrin DE2 solution reported with filled marks in Figure 9a.

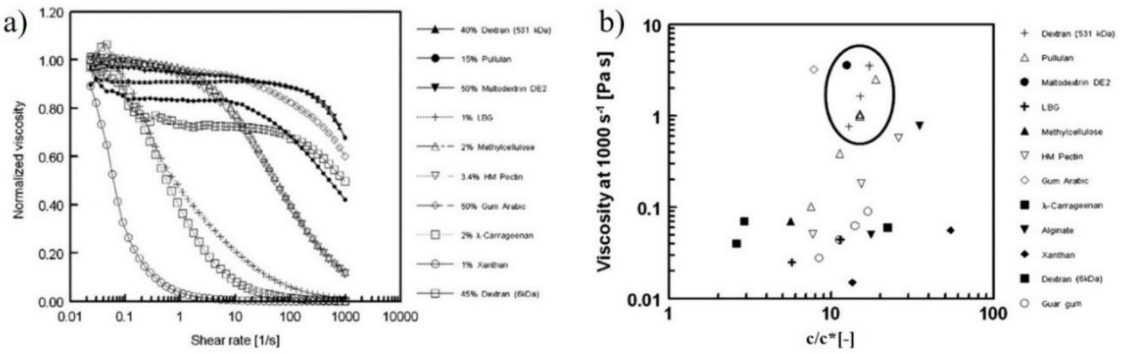

Figure 9. a) Flow curves of polysaccharide solutions. Spinnable samples are reported with filled symbols; b) Viscosity at 1000 s^{-1} as a function of polysaccharide concentration in units of overlap concentration c. [Stijnman et al., 2011]*

When shear viscosity, at the shear rate of 1000 s^{-1}, has been plotted as a function of the concentration (units of the overlap concentration c*), it showed a cluster of spinnable blends in the range of 10-20 c/c* (Figure 9b). The entanglement concentration has been deduced from intrinsic viscosity, and it has been proportional to the concentration where hydrodynamic radius has started to overlap as the concentration of polymer increased. Moreover, the concentration above which entanglements occur depends on the polysaccharide's chain morphology; in fact, globular-like chains have fewer entanglements than random coil chains due to the reduced chain's mobility causing processing failure.

Membranes based on the most attractive polysaccharides, like chitosan or hyaluronic acid, are tough to process individually; thus, researchers proposed many solutions to overcome this limitation, such as introducing novel chemical groups, and derivatizations in order to modify the physicochemical properties of the polymer.

Chitosan is challenging to be electrospun due to the significant number of amino groups in its backbone, which determines strong hydrogen bonds reducing the movement of polymeric chains during the application of the electric field. Solutions adopted are salification of chitosan, using trifluoroacetic acid, or processing its blends in fluorinated solvents. Other standard methods are the blending with natural or synthetic polymers, such as polyvinyl-alcohol, collagen or gelatin or its chemical derivatization, like methacrylated or quaternized derivatives of chitosan (Du and Hsieh, 2008; Lehmann-horn *et al.*, 2014). In this case, the chemical derivatization offers an additional autocrosslinking feature to improve the membrane's hydrolytic resistance once applied and enhancing the native antimicrobial properties of the material.

Similarly, aqueous hyaluronic acid solutions (HA) show high viscosity, high conductivity, and surface tension even at low concentration. Electrospinning processing of these solutions can be achieved by enabling electro-blowing, an electrospinning technique where a gaseous flow aids the polymer jet. Another method is the use of dimethylformamide (DMF) and water blends to decrease the surface tension of HA solutions. Thiolation of hyaluronic acid is a method that permits the improvement of electrospinning performances as well as its application; thus, the synthesis of the derivative reduced the molecular weight of the polymer and allowed the crosslinking of the matrix in oxidative conditions. In a reported study, the thiolated polysaccharide has been mixed with inert polyethylene oxide as a sacrificial carrier, extracted by soaking membrane in water after disulfide bonds formation (Ji *et al.*, 2006). Then, the absorption of fibronectin on the nanofibrillar surface has enhanced the invasion and the adhesion of fibroblasts overcoming anti-fouling properties of HA derivatives and approving the scaffold's application in tissue engineering.

Heparin is a highly anionic charged polysaccharide capable of establishing specific interactions with growth factors, such as bFGF and VEGF, determining their storing, protection from pH and enzymatic degradation. The interest of using the growth factor

retention ability of heparin focused as a bioactive-eluting system for vascular injuries (Wang, Feng and Zhao, 2012). Two methods permit the use of heparin in the nanofibrous scaffold, e.g. the blending with synthetic carrier polymers or the coating above already-formed nanofibers by electrostatic interactions and covalent bonding. The modification of PLLA nanofibers with heparin promotes aortic endothelial cells infiltration in the scaffold *in vivo*, due to the anti-clotting property and bioactive-binding properties of heparin (Kurpinski *et al.*, 2010).

The stacking of different esters of β-glucan generated an attractive example of a scaffold (BGE-B) with a hydrophobic-increasing gradient for skin regeneration (Wu *et al.*, 2016). The hydrophobic butyrate ester of β-glucan has consisted of the skin layer, whereas β-glucan acetate represented the inner layer of the hydrophilic side. Once placed in water, the swelling ability of the hydrophilic layer determines a significant decrement of mesh density which promotes the infiltration of fibroblasts (NIH3T3s) and keratinocytes (HaCaTs). The unchanged morphology of the skin layer prevents bacteria penetration and controls the evaporation rate from the wound. In rats, used as *in vivo* models, showed the complete wound closure after 14 days (Figure 10). In particular, the scaffold reported a lower inflammatory response in the early days and a more native skin-resembling re-epithelization than control and gauze controls.

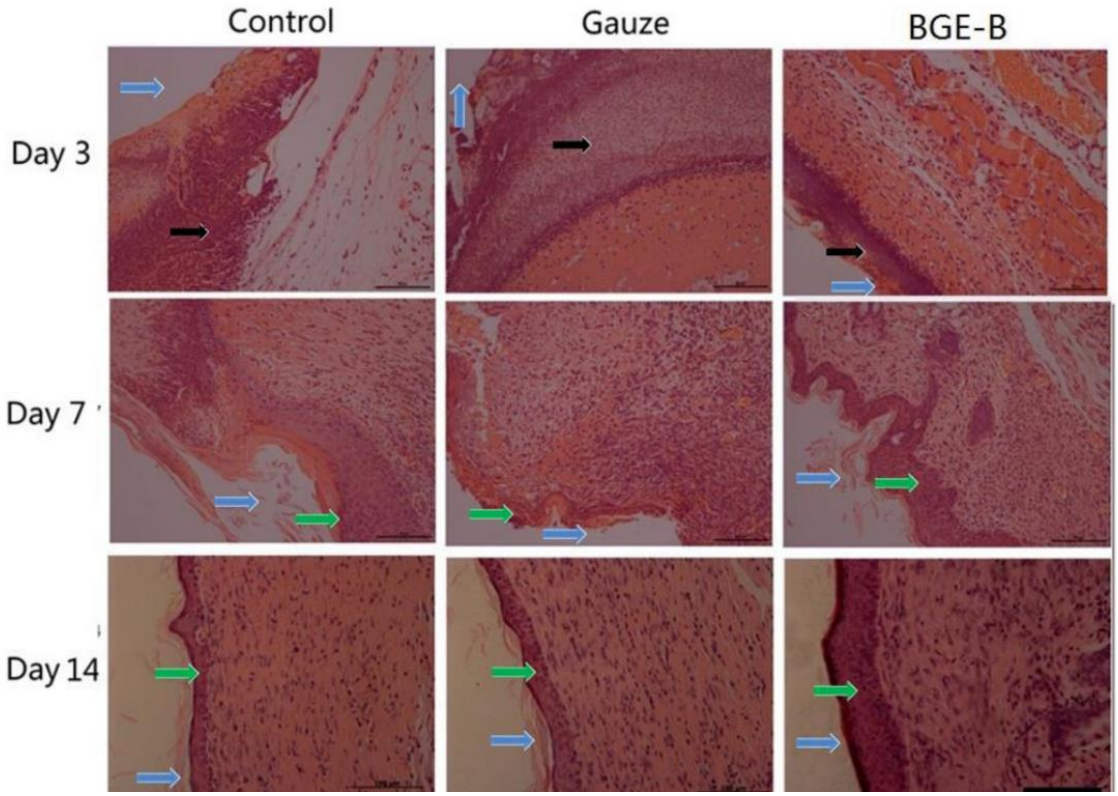

Figure 10. Histological analyses of dorsal skin sections stained with H&E after 3, 7 and 14 days of treatment. The scale bars are 100 μm for all the groups. Black arrows: inflammatory cells; green arrows: epithelialization; blue arrows: remaining materials. [Wu et al., 2016]

1.5.2 Electrospun membranes based on polysaccharides associated with electrospun synthetic polymers

The coupling of electrospun synthetic and natural polymers in multilayered devices manteins the benefits of both types of materials. For example, the polysaccharide layer gains the mechanical elasticity of the synthetic layer and provides higher biocompatibility. Some improvements in the bone regeneration field are reached covering poly(DL-lactide) nanofibers (PLA) with chitosan nanofibers (Cui *et al.*, 2010). In this work, chitosan deposition has implemented the growth of hydroxyapatite crystals on the nanofibrillar surface, and it has favoured osteoblasts (MC3T3) proliferation stimulating their osteogenic differentiation, as compared to results obtained from the pure synthetic matrix, in terms of increased mineralization as calcium deposits and increased alkaline phosphatases activity

(ALP) in a week. Another chitosan/PLA dual-layer membrane with aligned polysaccharide fibers showed a deeper infiltration and migration of epithelial cells than PLA membrane *in vitro* (Chen *et al.*, 2014). The *in vivo* performances of the device have demonstrated the absorption ability of exudates and the effective promotion of total skin tissue repair.

On the same trend, PCL nanofibers covered chitosan electrospun membranes incorporating aloe vera for skin regeneration purposes (Miguel *et al.*, 2017). Considering that proteins adsorption on the scaffold is one of the first events after application, the study evaluates the phenomenon on both surfaces. Albumin is the most abundant protein in serum, and it accumulates at the wound site. Once adsorbed, it is slowly replaced by fibronectin and vitronectin. As expected, the absorption of proteins occurred only above the hydrophilic side due to positive residues of chitosan and increased with time, modifying the surfaces and improving their roughness, porosity, and wettability.

The combination of these two layers generated a membrane with a lower water vapour transmission rate (1452 g/m^2 per day) than what considered close to the ideal values for wound dressing bandages (2000-2500 g/m^2 per day) to an adequate level of moisture and to prevent exudates accumulation; thus it should be considered slightly occlusive. The interest in the incorporation of aloe vera lies in the improvement of the antimicrobial properties of the membrane, in fact a greater reduction of colonies forming units effect against *S.aureus* and *E.coli* compared to plein PCL/chitosan membrane.

Stress strain curves and mechanical properties of such membrane has showed a close similarity to the native skin and the effect is mainly attributed to the presence of the PCL as top layer.

The absorption of chitosan and laminin onto PLA nanofibers represents another example of the increased results from the coupling of synthetic and natural materials in electrospun devices. The study has generated a bioactive scaffold to promote neurite outgrowth (He *et al.*, 2013). Laminin is a known protein able to improve the aspecific cell-adhesivity

properties of a surface and, here, is used as a neurite promoting ECM protein to mimic the biochemistry of nervous tissue. The coated device can promote a three-fold longer neurite outgrowth of DRG neurons (Figure 11 B-D) than pure PLA fibers (Figure 11 A). Furthermore, the coated-scaffold resulted as the only one able to induce the differentiation of neuronal stem cells as demonstrated by immunological staining as reported.

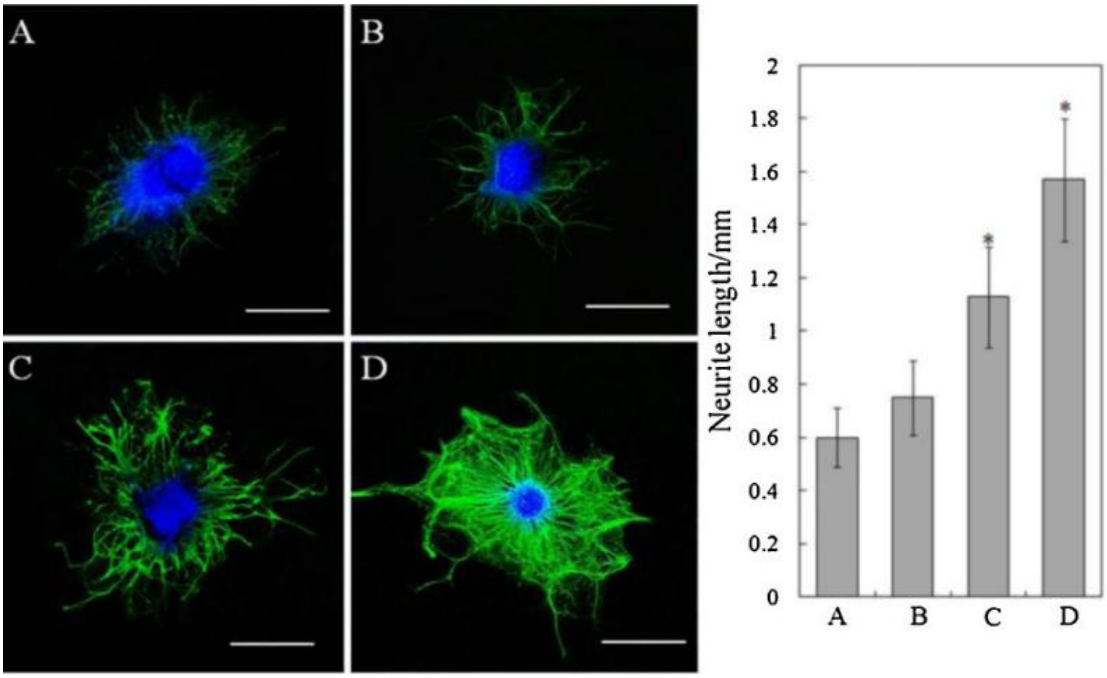

Figure 11. Laser scanning confocal micrographs and neurite length of DRG neurons after seven days of culture above A) PLLA nanofibers; B-D) PLLA coated with increasing laminin concentration. Neurites are stained with FITC and nuclei with DAPI. Scale bar 1 mm. [He et al. 2013]

1.5.3 Electrospun membranes based on polysaccharides and nanocarbon materials

Nanocarbon materials are referred to as forms of carbon below 100 nm. The only known allotropes forms of carbon were graphite and diamond until 1985. The discovery of fullerenes, carbon nanotubes (CNT), and graphene and the study of their technological properties represented the stimulus for the use of these materials in many fields, including biomedical purposes.

Many carbon-based nanocomposites have reinforced polymeric nanofibers enhancing electrical and thermal properties, leading to applications in the biology field. For example, biomedical grade nanodiamonds are used to improve the mechanical durability of blended chitosan/cellulose nanofibers for wound healing purposes (Mahdavi *et al.*, 2016). Incorporating the filler also determined a reduction of the average fiber diameter, and the mechanical strength increased. The elastic modulus of the sample reached values closer to skin elasticity (405 MPa) and reduced the percentage strain to failure. The enhancement could be attributable to the mechanical interlocking of polymer chains by nanoparticles because no chemical reactions between particles and polymers should occur.

Graphene is a single layer of carbon atoms arranged into a honeycomb lattice configuration, and it is considered a building block of carbon nanotubes, graphite and fullerenes. Related materials are graphene oxide (GO) and reduced graphene (rGO) with improved electrical features (Shin *et al.*, 2016; Kong *et al.*, 2018).

Graphene oxide is one of the most common graphene derivatives produced via chemical exfoliation of graphite characterized by easy processing, large scale production, and low fabrication costs. In the tissue engineering field, the main application of GO lies in the control of antimicrobial resistance in pathogens and low toxicity towards mammalian cells. The effect seems to be attributed to the generation of reactive oxygen species (ROS) able to destabilize bacterial membranes; thus, thanks to this nonspecific action on microbes; thus GO is often included in wound dressing scaffolds (Yang *et al.*, 2018). In other biomedical fields, GO can be used as a nanocarrier for drug delivery purposes due to the ability to establish π- π interactions with many drugs (Kansara *et al.*, 2019; Mauro *et al.*, 2019).

Carbon nanotubes are allotropes structures with a cylindrical structure where the walls are constituted of hexagonal carbon sp^2 hybridized, and they can be distinguished among single-walled (SWCNTs), double-walled (DWCNTs) and multi-walled (MWCNTs). All show an elastic modulus close to the diamond (1 TPa), thermal stability up to 2800°C, a thermal

conductivity two times than diamond and an electric capacity 3000 times higher than copper wire (Liu *et al.*, 2014). Most of the application in TE of CNTs occurred in association with electrospun synthetic biopolymers, especially polyesters.

Interesting results are obtained in cardiac and nervous regeneration, promoting electrical connections between cells of the damaged tissue portions. In recent work, hyaluronic acid aligned-nanofibers are doped with a low concentration of carbon nanotubes to increase the charge capacity of the fibers and to enhance the regenerative behaviour in neurons (Steel, Azar and Sundararaghavan, 2020). Under electrical stimulation (200 mV/mm biphasic 20 Hz AC square waveform), a faster elongation of neurites and the neuron number is demonstrated, and no cytotoxic effects are reported (Figure 12). The example shows the feasibility to endow electrical cues to hyaluronic acid at low concentrations (0.01% of CNT per milligram of polymer), improving tricky regeneration outcomes, like neurite elongation.

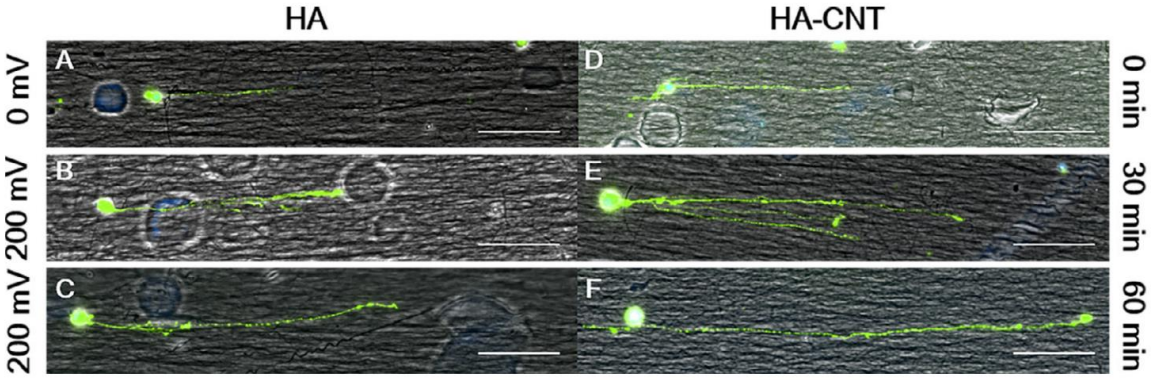

Figure 12. Merged fluorescence and brightfield micrographs (scale bar 50 μm) of dissociated dorsal root ganglia neurons fixed after 72 hours of culture in serum-free media supplemented with 50 ng/ml NGF. 24 hours after attachment, neurons were electrically stimulated for either 30 min (B, E) or 60 min (C, F) and compared to unstimulated neurons on HA and HA-CNT (A, D). [Steel, Azar and Sundararaghavan, 2020]

Moreover, the hard homogeneous dispersibility of these nanofillers in polymeric solutions suggests finding alternative ways of inclusion or decoration. The co-electrospinning technique is one of the most applied strategies for including these fillers in polysaccharide

nanofibers (Kong *et al.*, 2018). Another opportunity is represented by layer-by-layer self-assembling deposition to generate multicylindrical nanofibers (Luo *et al.*, 2013). The method permits to coat the external surface of fibers more times with different material. For example, cellulose acetate fibers expose negative charges on the surfaces. The soaking of such membrane in a chitosan solution, positively charged, determines the electrostatic self-assembling of the polymer on the surface, assuming positive residues, and then immersed in a negatively charged solution of multiwalled carbon nanotubes. Repeated cycles of immersions/rinsing have generated multicylindrical nanofibers of desired thickness. A low number of layers has already determined a mechanical improvement in terms of tensile stress and ultimate strain. Supports have showed a rougher surface which allows a huge adsorption of serum proteins and the spreading of fibroblast cells (L929); thus they are proposed for general tissue engineering purposes and the fabrication technique, namely the layer-by-layer deposition, should be proposed also for the entrapment of bioactive molecules.

1.6 Cellular differentiation induction and chemoattractant properties of advanced electrospun matrices

In regenerative medicine, the differentiative potential of pluripotent stem cells is a promising tool to restore full tissue functionality (Lehmann-horn *et al.*, 2014). In particular, mesenchymal stem cells (MSCs) reveal to be eligible for cellular therapy purposes; in fact, they can secrete bioactive molecules to differentiate in many cell lineages, such as osteocytes, stromal cells, chondrocytes, fibroblasts, myocytes, or astrocytes, as schematized in Figure 13. Paracrine signals regulate the differentiation of MSCs, including local stimulations like mechanical and electromagnetic signals. The similarity of electrospun membranes to the ECM, in terms of structural resemblance, mechanical stability, and porosity, provides strong cell-scaffold interactions. The interaction with fibers is exerted by many filopodia of MSCs; thus, the close and broad contact induces the desired differentiation quickly. The dynamic response of MSCs differentiation can be categorized considering applied external stimulus as exposure to growth factor or growth medium, physicochemical stimuli, electrical, and magnetic stimulation (Rajasekaran *et al.*, 2020).

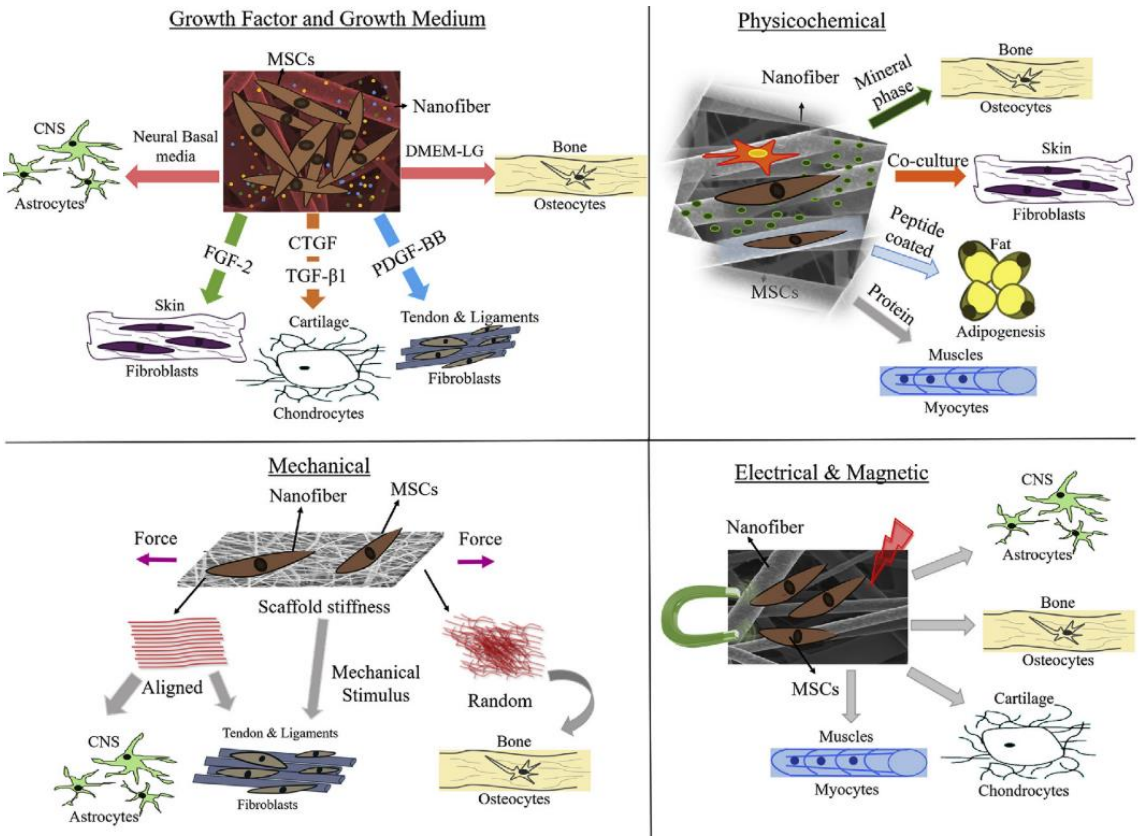

Figure 13. Representation of MSCs differentiation in different cell lines when in contact with nanofibers and exposed to different stimulation. [Rajasekaran et al., 2020]

The fibrogenic differentiation of MSCs has been obtained incorporating connective tissue growth factor (CTGF) and fibroblast growth factor (FGF-2) in silk fibroin (SF) solution covered by polylactide-caprolactone (PLCL) and polyethylene oxide (PEO) in core-shell nanofibers by coaxial electrospinning (Xu *et al.*, 2017). The two actives are included separately; in particular, the CTGF is in the core layer, while the FGF-2 is included in the shell, determining a dual release of the actives. FGF-2 release depended on the dissolution of PEO, while the release of CTGF is controlled by both diffusion, through the silk fibroin matrix, and dissolution of the shell. The set up determined a temporarily sequential release of factors; thus, the burst release of FGF-2 (about 50% of GF loaded after 1 day) helped the recruitment and the adhesion of MSCs and their spreading. The sequential slowly release of CTGF from the core directs the fibrogenic differentiation of MSCs effectively, as

demonstrated by quantitative gene expression levels of several fibroblast markers compared to active-free membranes, i.e. FSP1, COL1, and Vimentin reported in Figure 14.

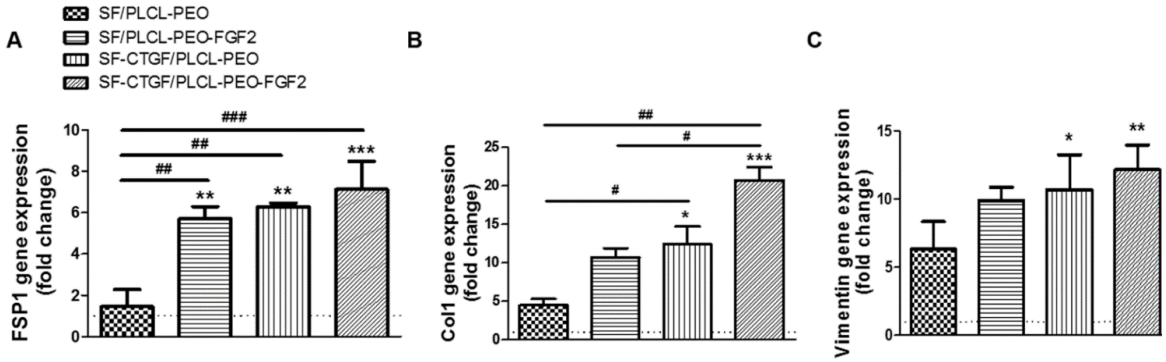

Figure 14. Quantitative gene expression levels of fibroblast markers a) FSP1; b) COL1; c) Vimentin. Significant differences with p<0.05, p < 0.01, and p < 0.001 are reported using #,##, and ###, respectively. [Xu et al., 2017]

Strategic approaches which exploit chemoattractant gradients to guide tissue regeneration, i.e. avoiding the use of external cell sources, have overcome classic stem cell-based therapies. Drawbacks associated with the use of heterologous stem cells strategies are invasive donor biopsies, time-consuming and costly procedures that can negatively affect the behaviour and the phenotype of cells; in fact, a common risk is represented by the malignant transformation of *in vitro* cultured cells. The use of body resources by host stem cell recruitment is safer and more effective with increased therapeutic outcomes (Pacelli *et al.*, 2017). The host cell recruitment uses different biological molecules, such as adhesive peptides, antibodies, nanomaterials, or chemoattractant gradients of growth factors.

Platelet-derived growth factor (PDGF) is the only GF approved by the FDA to treat lower extremity diabetic ulcers. It plays a critical role as an initiator and mediator of wound healing, acting as a chemotactic agent for neutrophils, monocytes, and fibroblasts regulating matrix deposition. PDGF is loaded in chitosan/fibrinogen electrospun scaffold by co-electrospinning technique as a wound dressing device that can influence the migration of fibroblasts and improve the wound healing rate (Yuan *et al.*, 2018). The migration is valued

with a cell migration kit (ORIS™) to assess the bioactivity of the growth factor (Figure 15). The kit uses barriers to create a central cell-free area in the culture well plates, so, after their remotion, cells migrate into the central area.

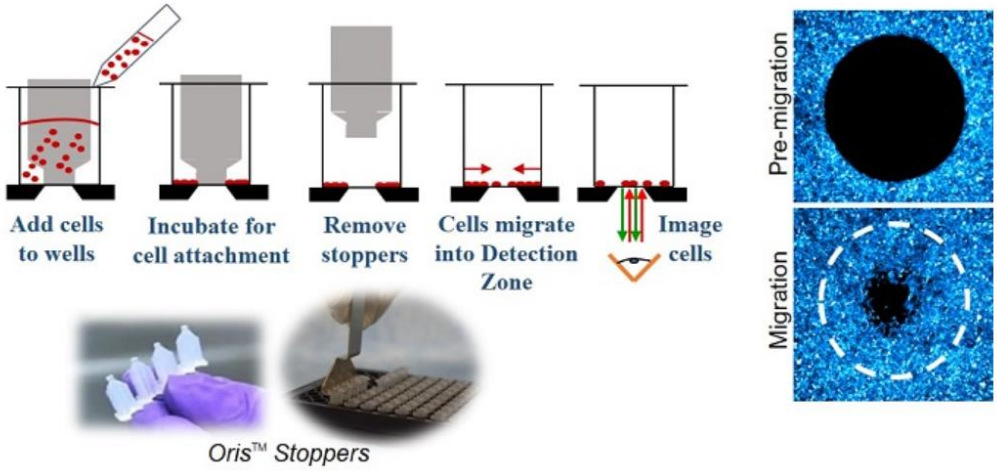

Figure 15. Cell migration assay by ORIS™ kit

In the cited work, the fibroblasts migration is tested using the eluates from PDGF-loaded chitosan/fibrinogen scaffolds, collected during *in vitro* degradation experiments with an increasing amount of growth factor loaded. According to the loadings, the rate of fibroblast migration results higher, demonstrating the preservation of PDGF bioactivity after electrospinning processing. *In vivo* performance of the scaffold should be further investigated as an enhancer of fibroblasts recruitment for wound healing purposes.

1.7 Application in regenerative medicine: wound dressing

Skin is the largest organ in the human body, and its extension can reach two squared meters. It consists of three layers, i.e. epidermis, dermis and hypodermis. There are also skin appendages, like hairs, sweat and sebaceous glands, and nails (Figure 16)Figure 16. Representative cross-section of skin and its hierarchical organization. All these elements contribute to the functionality of the whole tissue. The skin's primary function is to act as a barrier from chemical, physical, microbial agents and the thermoregulation of the body.

The epidermis is the superficial layer of the skin composed of proliferating basal and differentiated suprabasal keratinocytes interconnected by tight junctions. Other cellular elements present in the epidermis are Merkel cells (tactile epithelial cells), melanocytes (melanin-producing cells), and Langerhans cells (tissue-resident macrophages). The distribution of keratinocytes divides the epidermis into five strata, i.e. stratum corneum, lucidum, granulosum, spinosum and basale, as reported in Figure 16.

From stratum basale, cubic-shaped keratinocytes begin to multiply by mitosis, ascend towards the most superficial layers gaining a flattened shape, synthesizing keratin and activating apoptosis. The basement membrane connects the epidermis and dermis; a layer constituted of collagen can control the traffic of cells, cytokines and growth factors. In superficial strata of skin, keratinocytes lose nuclei and renew the older layer of the corneum stratum. Here, keratin and residual cellular structures reduce the water permeability of the skin. All around skin annexes, there are pockets where proliferative stem cells reside.

Under the skin, the dermis is distinguishable and consists of a superficial papillary region and a deeper reticular region. The first one consists of loose areolar connective tissue, and it is the primary source of nutrients and oxygen for the whole skin, thanks to the high capillary vascularization. The reticular region comprises a dense and irregular connective tissue composed of collagenous, elastic, and reticular fibers. In this region are located most of the skin appendages and small blood vessels.

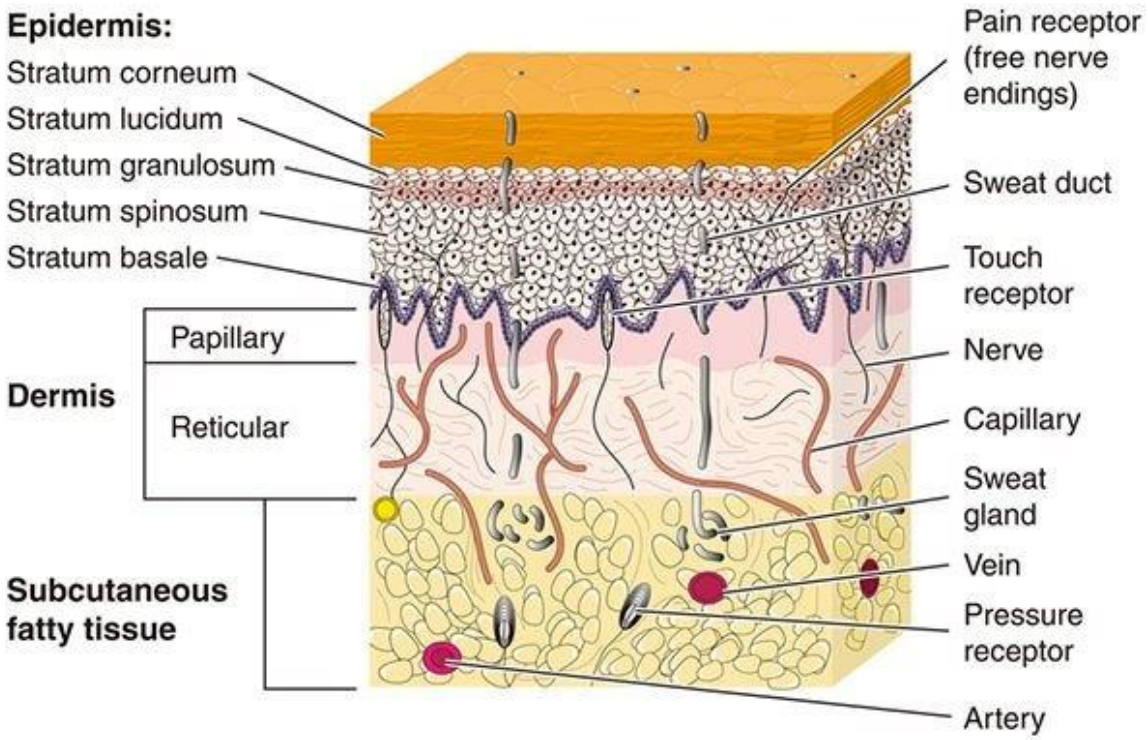

Figure 16. Representative cross-section of skin and its hierarchical organization

Extensive and in-depth injuries of skin represent a severe healthcare problem. Pathogens can easily access the body causing acute or chronic inflammations. Injuries can be classified considering the damage in partial-thickness and full-thickness wounds or classified as acute or chronic wounds. In a cross-section of the skin, superficial damage regard only the epidermis. Here, fibroblasts and stem cells resident in the dermis can rapidly regenerate the tissue ECM. Otherwise, in deep wounds, a substitute of skin is required, for example, for severe burns (Van Kilsdonk *et al.*, 2013). Historical therapeutic approaches are autologous and heterologous transplants with several applicative limitations and medical issues, like rejection.

The healing of wounds is a dynamic orchestrated process described by a multistep of ordered molecular and cellular signals. The progression of the physiological healing occours through four stages. After the injury, blood flows out, so the hemostasis phase takes place, stopping bleeding by platelets aggregation (Figure 17A).

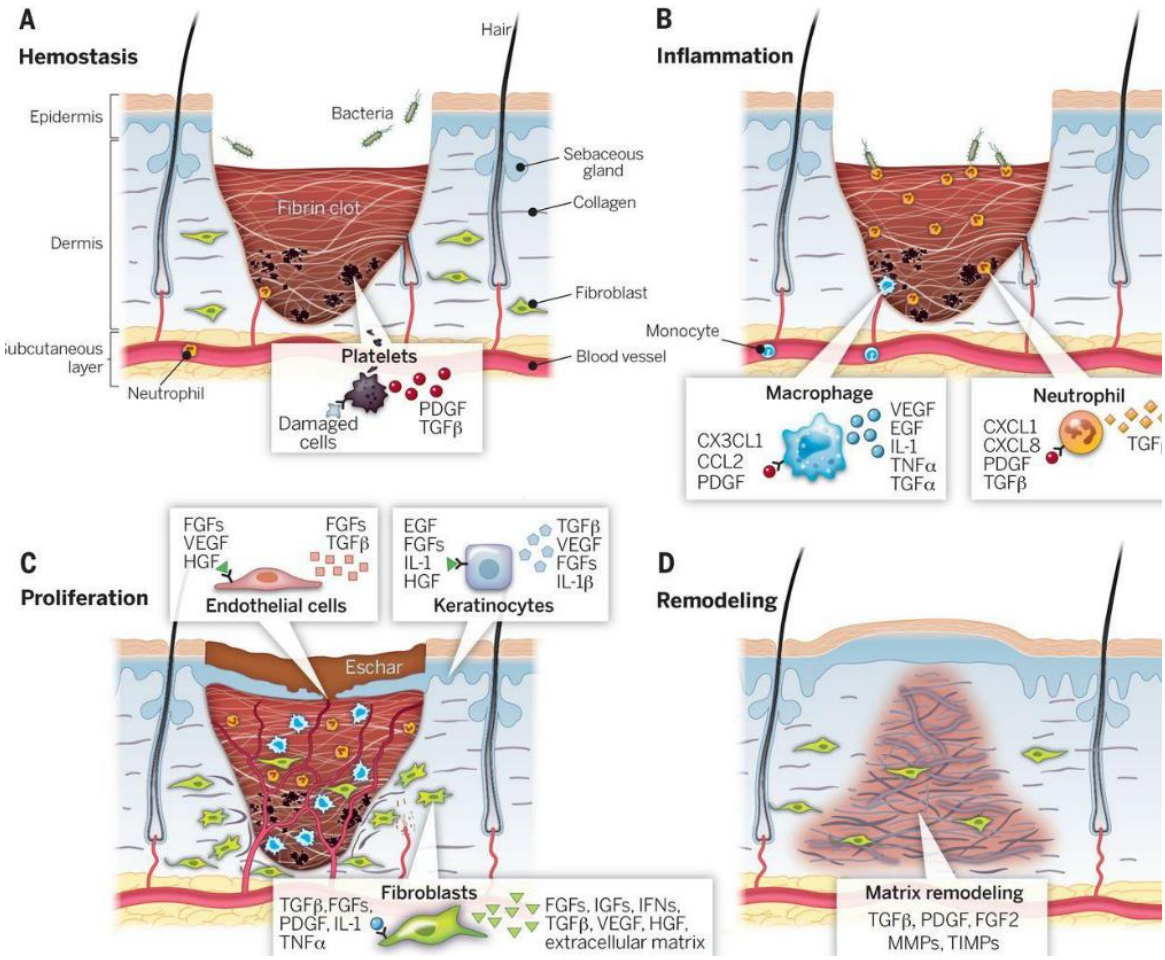

Figure 17. Schematic illustration of the healing process and phases, hemostasis and coagulation (A), inflammation (B), proliferation (C), and remodelling (D).[Sun et al. 2014]

Factors released from platelets determine the vasoconstriction and recruitment of leukocytes to begin the inflammatory phase (Figure 17 B). Neutrophils reach the damaged area, remove debris and bacteria, and amplify the immune response secreting interleukin IL-1, IL-6 and the tumour necrosis factor-α (TNF- α) (Figure 17 B). Monocytes have been recruited and matured into macrophages, enforcing the cleaning and releasing insulin-like growth factor 1 (IGF-1) and transforming growth factors α and β (TGF α TGF β) (Eming, Krieg and Davidson, 2007). After 24 hours, the proliferation phase initiates where fibroblasts produce metalloproteinases and ECM components, like collage type III, hyaluronic acid (HA) and fibronectin, remodelling the clot in a novel connective tissue (Figure 17 C). In this phase, re-epithelialization occurs, forming a new epidermis where

stem cells from follicles differentiate into epidermal progenitor cells. The neovascularization generates new vessels through angiogenesis. The connective tissue produced, called granulation tissue, is raw; thus, it is remodelled by secretion of collagen type III and ECM components from fibroblasts (Figure 17 D). During the final phase of the healing process, the granulation tissue contracts restructuring in a mature scar thanks to the activity of myofibroblasts, generated from the differentiation of fibroblasts through the secretion of platelet-derived growth factor (PDGF) (Darby and Hewitson, 2007). Other events of this phase are the substitution of collagen type III with organized collagen type I with higher tensile strength and the regression of vascular network and cell population, like healthy skin. Chronicity occurs when healing has not completed within three months. The chronicity of a wound can be classified into four groups, i.e. arterial insufficiency ulcers, diabetic foot ulcers, pressure ulcers and venous ulcers (Moura *et al.*, 2013). These pathologies share common clinical evidence like a prolonged inflammatory phase, increased metalloproteinases accumulation, and inadequate vascularization, preventing granulation tissue and re-epithelialization processes.

For the treatment of chronic wounds, several dressing strategies have evolved during years from simple gauze to advanced care systems, like living skin equivalents and bioactive-loaded products delivering cells, growth factors, vitamins, and anti-oxidant molecules (Castaño *et al.*, 2018).

Recent studies include polysaccharide-based electrospun membranes for the treatment of severe wounds. Electrospun matrices of hyaluronic acid and gelatin show a wound closure of second-degree burns in rats faster when compared to a product fabricated with similar biomaterials and commercially available as biomedical dressing (Ebrahimi-hosseinzadeh, Pedram and Hatamian-zarmi, 2016). The composition of the scaffold has helped the reconstitution of the burnt area. However, as previously discussed, improved therapeutic outcomes have been achieved by promoting the cellular repopulation of the area and

inhibiting microbial growth by incorporating additives, such as silver nanoparticles and antibiotics. Considering that an infection occurring during the healing process should compromise tissue regeneration (Han and Ceilley, 2017), it is usual to treat patients with antibiotics (such as gentamicin, ciprofloxacin, vancomycin, streptomycin) having activity against Gram-positive and Gram-negative pathogens through oral administration.

Nevertheless, this therapeutic approach presents several disadvantages, such as rapid elimination from the bloodstream, degradation, and narrow therapeutic windows (Sónia P. Miguel *et al.*, 2019). To overcome these limitations, topical administrations have been researched for wound dressings. Nowadays, the direct incorporation of these active ingredients into the electrospinning solution is widespread, offering high drug loadings, displaying a controlled release, and providing an aseptic environment. The drug interactions with the polymer could modulate the release of the active once in contact with physiological fluids. Wound healing purposes require an initial burst release during the first 24 hours and a sustained release until the healing ends, keeping the amount of the active above the minimum inhibitory concentration.

Some materials, like chitosan, own self-antibacterial properties; moreover, the inclusion of antibiotics amplifies the activity with no additional cytotoxic effects. For example, teicoplanin, an antibiotic drug of the glycoprotein class, is loaded in chitosan nanofiber for the prevention of severe Gram-positive infections as local drug delivery and wound dressing system able to interfere with the polymerization of the wall of peptidoglycan bacteria (Ajami, Shahroodi and Amiri, 2020). Both teicoplanin and chitosan show positive charge in physiological conditions; thus the electrostatic repulsions causes a burst release equal to the 60% of drug loaded during the first 24 hours and lasts until 14 days. The addition of the antibiotic has increased the wound closure rate in *in vivo* rats model as compared to the negative control.

A more useful choice is to design biodevices to achieve the recruitment of local cellular populations (Kim and Tabata, 2015). Such bioactive materials can instruct hosted cell, guiding and enhancing the healing and tissue integration(Lutolf, Gilbert and Blau, 2009). The Fibroblast Growth Factor (FGF) represents a family of growth factors having chemoattractant properties, promoting migration of fibroblasts, accelerating granulation tissue formation, re-epithelialization and tissue remodelling, thus enhancing regeneration efficiency (Behm et al., 2012; Barrientos et al., 2014). Moreover, the incorporation during electrospinning could alter the bioactivity of the factor itself; thus same papers have reported alternative strategies to decor nanofibers and to preserve the entire activity of the factor. For example, the electrospun PLGA membrane is covered with bFGF during a post-electrospinning treatment using polydopamine as a linker and a dip-coating method (Sun *et al.*, 2014). The surface modification of PLGA fibers, proposed in this work, substantially reduces the water contact angle of the membrane with no changes in terms of fiber morphology. The stimulating effect of the scaffold promotes the shortest re-epithelization time (14 days) concerning the control *in vivo*, i.e. rabbit ear wound model. The staining of new collagen deposed into the wound has quantified the re-epithelization degree that results close to the normal tissue. In chronic ulcers healing, the cell migration and the angiogenesis phase have been impaired, determining a severe healing time extension.

A scaffold should encourage the progression of healing by wisely controlling the release of stimulatory factors. For example, an electrospun membranes based on hyaluronic acid and collagen is produced by co-electrospinning of two polymers solutions (Lai *et al.*, 2014). For the production of this membrane, blends have loaded VEGF, bFGF, PDGF and EGF before the processing. The release kinetics of each factor have been studied and tuned to restore the skin from a chronic condition. In particular, EGF and bFGF have been directly dispersed within the nanofibers reflecting a rapid release due to fiber degradation.

In contrast, VEGF and PDGF have been included in gelatin nanoparticles to delay their releases in a proper timeframe according to the remodelling and re-epithelization phases of the healing, as of late stages of skin reconstitution. The amount of FGF and VEGF loaded has determined the chemotaxis of endothelial cells, and it has represented signal cues to guide the sprouting and the settling of these cells into vascular-like structures. Although the topical administration of GFs presents several drawbacks such as low *in vivo* stability, restricted absorption through the skin, and elimination by exudation, the loading in nanofibers still results as an attractive strategy for improving wound healing process.

1.8 Application in regenerative medicine: periodontal reconstitution

Periodontitis is one of the most prevalent chronic and destructive inflammatory diseases in humans. It consists of the destruction of tooth-surrounding tissue, and it has a multifactorial etiology. Periodontitis leads to the destruction of the periodontal soft and hard tissues, including alveolar bone, the periodontal ligament and root cementum. If untreated, it results in a progressive loss of periodontal bone and, subsequently, tooth loss due to the generation of a pocket as a favourable environment for the growth of aerobic pathogens. Once damaged, the periodontium has a limited self-regeneration (Lian *et al.*, 2019). The current approach is the Guided Tissue Regeneration, GTR. It is a method for preventing epithelial migration along the cemental wall through the placement of barriers to cover bone and periodontal ligament, thus temporarily separating them from the gingival epithelium. During the post-surgical healing phase, it prevents epithelial cells migration into the wound. It permits the recolonization of the root area by progenitor cells, located in the remaining periodontal ligament, from adjacent alveolar bone or blood, permitting their differentiation into a new periodontal supporting apparatus with the formation of new bone, periodontal ligament, and cementum.

There are three generations of GBR membranes following Gottolow's classification: non-resorbable, resorbable and resorbable with growth factors. An ideal barrier membrane should be biocompatible, non-toxic, non-carcinogenic, inert, non-antigenic, sterilizable, handy, rigid, suitable for specific clinical situations, retrievable in case of complication, and it should not be too expensive (Marinucci *et al.*, 2001).

In tissue engineering, the main properties of biomaterials allow the proposal of grand and fascinating strategies to lead to the resolution of unsatisfied therapeutic needs. Top qualities of every material are studied so, today, the research sets its targets towards the appropriate design of a new generation of scaffolds with improved effectiveness. These supports can be obtained by electrospinning technique, a method that can process a polymeric solution, emulsion or suspension, and carry drugs or bioactive factors in thin mats composed of nanostructured fibers (Caballé-Serrano *et al.*, 2019). Some drugs promote osteogenic differentiation; examples of them are simvastatin and dexamethasone(S. M. Kim *et al.*, 2013; Castro *et al.*, 2018; Muniz *et al.*, 2018; Rajeshwari *et al.*, 2019). In particular, statins present several pharmacologic effects beyond hypolipidemic effects, such as anti-inflammatory, immunomodulatory, antioxidant, promoter of angiogenesis and differentiation of osteoblasts and inhibitor of osteoclasts. Statins, for example, may attenuate periodontal inflammation by decreasing interleukin (IL)-1 beta and increasing IL-10 levels in patients with periodontitis, as demonstrated by several papers. In particular, a study (Santos *et al.*, 2017) evaluated the effect of simvastatin-loaded Natrosol gels in rats as animal models. The positive effect of simvastatin for periodontal disease is demonstrated considering the activation of plural mechanisms, such as the reduced secretion of pro-inflammatory cytokines and reduced secretion of some metalloproteinases, main accountable factors for periodontitis. The action of statins can also be related to the inhibition of osteoblast apoptosis by increasing the expression of modulator factors for the transcription of TGF-beta, an essential growth factor in bone formation. The disadvantages

of simvastatin use, highlighted in this study, have noticed the need to improve the drug administration. The gelled vehicles have not been considered appropriate, so simvastatin needs to be loaded in engineered scaffolds to avoid any side effects related to the administration for accidental oral ingestion, such as constipation, nausea or diarrhea.

Dexamethasone has been documented to exert osteogenic differentiation and of human periodontal ligament cells (hPDL). A study (S. M. Kim *et al.*, 2013) has evaluated the dose-dependent effect of this glucocorticoid on the expression of several genes involved in apoptotic and osteogenic processes of the human periodontal ligament. The range of applicability of this drug has been related to the physiological circulating levels of glucocorticoid, such as 100 to 1000 nM. Depending on dexamethasone concentration, alkaline phosphatase activity can be modified, reflecting a dose-dependent effect on osteoblasts. A negative effect of high dexamethasone levels has been valued as increasing apoptosis, decreasing the hPDL proliferation, and bone formation. This study has showed the importance of specific dexamethasone levels(Nguyen *et al.*, 2012). The main effects are the expression of specific markers of the osteoblastic phenotype in primary hPDL cells, and the suppression of antiapoptotic genes that probably promote differentiation in osteoblastic phenotype through bone-specific markers. Other researchers have documented the same effects explaining how the up-regulation of apoptotic genes and the down-regulation of antiapoptotic genes have promoted the differentiation and mineralization of these cells for periodontal diseases.

A bilayered membrane for periodontal regeneration has been investigated, combining PLGA and gelatine (Lian *et al.*, 2019). In particular, a layer consists of PLGA/gelatine loaded with dexamethasone in silica nanoparticles, while the outer layer is PLGA bearing doxycycline by a two-step electrospinning method. The membrane exerts both osteogenic and antibacterial functions. The PLGA/gelatine layer permits cell infiltration from periodontal ligament and the PLGA, loaded with an antibiotic, acts effectively as a barrier

to prevent epithelial cell infiltration from gingival side and reducing the microbial count. The inclusion of gelatine has helped the proliferation and the adhesion of bone-marrow derived stem cells (BMSCs). Sample loaded with plein silica nanoparticles and samples loaded with dexamethasone in silica nanoparticles determined an upregulation of the alkaline phosphatases activity (ALP) during the first seven incubation days. After 14 days, cell cultured above the dexamethasone-loaded bilayer nanofibers have showed the highest ALP levels. The quantification of calcium chloride after 21 days and the evaluation of immunofluorescence of osteocalcin, a distinctive marker of late stages of osteogenic differentiation, have confirmed the osteo-differentiation of BMSCs.

2. Aim of the thesis

The complete regeneration of damaged human tissues and organs is still a significant challenge. The integrative use of biomaterials, cells, and bioactive factors in all-in-one devices exploits all current knowledge of materials science, nanotechnology and stem cell biology to best mimic the complex hierarchical architecture of native tissues. The artificial microenvironment design must be properly tuned to match the physicochemical features of the target, offering adequate nanoscale patterns and biological domains for cellular interactions. Scaffolds must promote and guide the regeneration route by mimicking host signalling pathways through the controlled release and retention of drugs or growth factors. For these purposes, polysaccharides have been often used and proposed to manufacture bioengineered scaffolds for regenerative medicine applications due to high biomimetic characteristics. The efforts made by researchers have highlighted how the cellular interactions with electrospun biomaterials offer excellent performances to achieve the desired differentiation and integration with the surrounding tissue.

In the light of the Introduction, alkyl derivatives of gellan gum (GG) and hyaluronic acid (HA) have been investigated as novel bioactive electrospun membranes for wound healing and periodontal regeneration.

Gellan gum is an emerging polysaccharide from microbial origin widely used in tissue engineering with low cytotoxicity. Main properties regard the ability to form physical hydrogels whose mechanical stiffness can be tailored for bone, cartilage, muscle and brain regeneration (Stevens *et al.*, 2016; Palumbo *et al.*, 2020).

Hyaluronic acid is one of the main components of the natural extracellular matrix playing a pivotal role in cellular and tissue functions. This polymer has been widely used for engineered scaffolds, particularly hydrogels, due to its biological importance. HA offers several reactive groups onto the backbone for chemical derivatization, favouring the

processability of the polymer during scaffold's fabrication or improving *in vivo* performances of its supports (Highley, Prestwich and Burdick, 2016).

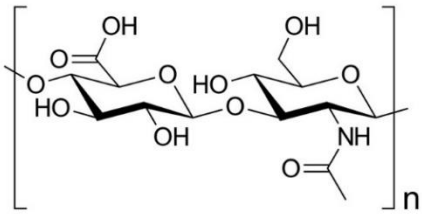

Hyaluronic acid

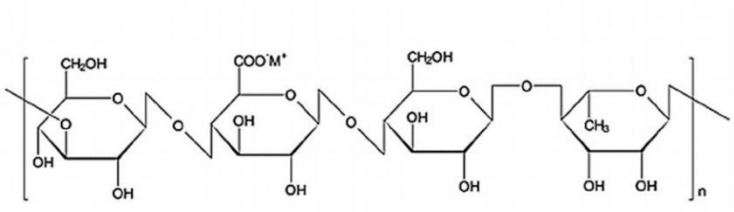

Gellan Gum

In this thesis, all the derivatives of these two polysaccharides have been produced via activation of the primary hydroxyl groups of β-glucose of gellan gum or N-acetyl-D-glucosamine of hyaluronic acid with bis(4-nitrophenyl) carbonate and the grafts of aliphatic chains at a different length. For hyaluronic derivatives, small moieties with free amino groups have been additionally inserted with the same chemistry.

Membranes based on the octyl- and dodecyl-derivative of gellan gum (GG-C_8 and GG-C_{12}) have been produced by electrospinning and characterized in terms of fiber distribution and orientation verifying the improved processability of the polymers compared to native gellan gum. Rheological analyses have studied the influence of alkyl derivatization on the spinnability of blends. The feasibility of the process regarded the octyl-derivative one, so the swelling ability of such scaffold has been analyzed under physiological conditions after crosslinking with calcium chloride at different concentrations.

To treat partial-thickness wounds, the membrane has been proposed to improve the cell homing at the damaged site, the adhesion of cells, and to encourage the regeneration of the extracellular matrix lost. Similar instrumental settings are used to incorporate the growth

factor FGF-2 in the octyl-based membrane (GG-C_8). The study has investigated physical interactions between the active and the polymer and how the ionotropic sensitivity of the GG-C_8 could be exploited to assess a suitable FGF-2 releasing profile. The fabrication of the bilayer biodevice has involved a hydrophilic layer covered by a synthetic polyurethane layer loaded with ciprofloxacin. Considering the crosslinking degree of the membrane, the dissolution rate and the releases of FGF-2 and ciprofloxacin have been valued with Franz cells. The antibacterial effect of the bilayer has been investigated against the inhibition of units forming colonies of *Staphylococcus aureus* in the timeframe compatible with the complete regeneration of the tissue. The chemoattraction ability of the scaffold and the cytocompatibility have been tested using cultures of human fibroblasts (NIH3T3) by a specific migration assay.

Electrospun membranes based on four chemical derivatives of hyaluronic acid at increasing hydrophobic character have been prepared and loaded with dexamethasone (a known osteoinductive drug) to induce osteogenic differentiation in pre-osteoblasts (MC3T3). The fibrillar supports have been characterized with a scanning electron microscope, and the hydrolytic and enzymatic degradation, as well as dexamethasone releases, have been tested after an autocrosslinking procedure.

HA membranes have been designed as guided-bone regeneration barriers for periodontal regeneration; thus, wettability properties and biological performances have been investigated. The proliferation of cells above membranes is valued up to seven days, and *in vitro* osteogenic induction is followed by quantifying the activity of alkaline phosphatases and evaluating the calcium content after one month of MC3T3 cultures.

The final aim of the thesis is to fabricate a hyaluronan based membrane with high antibacterial properties for the healing of chronic wounds. The proposed membrane consists of incorporating graphene oxide in an electrospun membrane of a hydrophilic derivative of HA loaded with ciprofloxacin. According to an external laser stimulation in the near-

infrared, the drug-releasing profile and hyperthermal features have been studied and related to the abiliity of eradicate bacterial infections and inhibiting the generation of biofilm. The cytocompatibility has been valued culturing fibroblasts for up to three days, and the membrane was valued as a wound dressing system.

3. Results and discussion

3.1 Fabrication of electrospun membranes based on alkyl derivatives of gellan gum

The primary purpose of this initial investigation is the generation of electrospun layers based on gellan gum alkyl derivatives as hydrophilic support for epithelial regeneration. In the first instance, the hydrophobization of the polysaccharide has been proposed to improve electrospinning processability. The study has aimed to generate three different nanofibrillar membranes at increasing hydrophobic behaviour; thus, the different physicochemical features, like hydrolytic resistance and drug-eluting properties, could be exploited for a better wound healing integration.

The study analyzes the feasibility of processing these materials through the electrospinning technique on the basis of the rheological behaviour of blends.

3.1.1 Hydrolysis of Gellan Gum and synthesis of its alkyl derivatives

Gellan gum (GG), commercially available in the low-acyl form called Gelzan®, has been hydrolyzed in alkaline conditions at pH 13 for 24 hours at 50°C. The product obtained, GG at low molecular weight, has been converted in the tetrabutylammonium salt, GG-TBA, through an ion-exchange column to favour the following derivatization procedures. The functionalization with alkyl moieties, octylamine and dodecylamine, occurs via the activation of hydroxyl functions of the polysaccharide backbone with bis(4-nitrophenyl) carbonate (4-NPBC) following a procedure reported in the literature (Agnello, Gasperini, *et al.*, 2017). The grafting of octylamine and dodecylamine and purification procedures have

generated two polymers labelled as GG-C_8 and GG-C_{12} with a derivatization degree of 17 mol% and 18 mol% (Scheme 2).

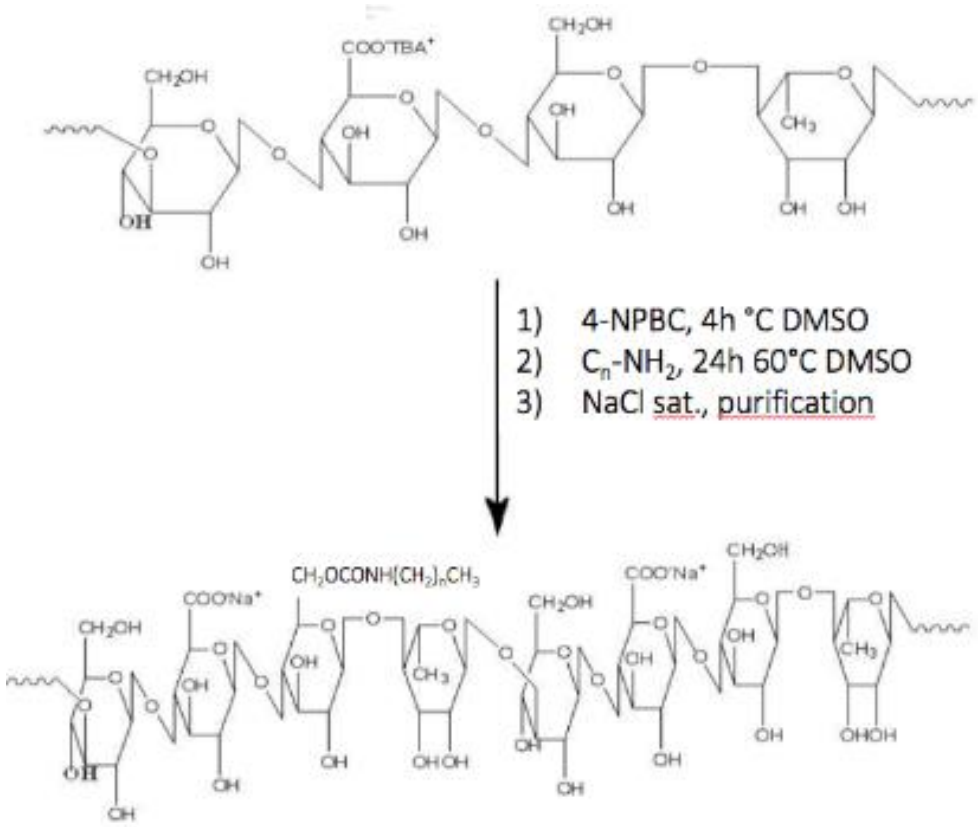

Scheme 2. Synthesis of alkyl derivative GG-C_8 and GG-C_{12}

The polymers obtained have shoswed a reduced ionotropic sensitivity and aqueous dispersibility compared to native Gelzan. This effect could be attributed to novel intramolecular interactions, i.e. hydrophobic associations, induced by aliphatic pendant chains, which interfered with native transition random coil-to-helix of gellan gum. The increasing entity of hydrophobic aggregations has been related to the length of grafted chains and the derivatization degree of the polymer, as more evident for GG-C_{12} sample. The alkyl graft has caused a reduction of GG-C_8 and GG-C_{12} molecular weight compared to starting hydrolyzed GG as resulted from SEC analyses (GG-C_8, 94.2 kDa, PDI 1.73; GG-C_{12} 91.5 kDa PDI 2.04, GG-TBA 96.7 kDa, 2.6 PDI).

3.1.2 Settings of electrospinning parameters

The three derivatives (GG-TBA, GG-C_8, and GG-C_{12}) have been tested as the main component of the aqueous blend for the generation of electrospun membranes and the effect of alkyl derivatization on processing performances was studied. In the light of the inability of processing pure aqueous dispersions of GG derivatives, as resulted from preliminary tests, a polymeric carrier has been added, i.e. the polyvinyl alcohol (PVA, 80kDa). As reported in the literature (Yang *et al.*, 2010), the lowest PVA (80 kDa) concentration in an aqueous solution is 6% w/v to generate a continuously charged jet.

PVA has been mixed with polymer blends in a weight ratio equal to 1:1 in deionized water. The ability to generate Taylor's cone and the deposition of solid material on aluminium foil have been chosen as principal evidence to select the final composition of blends. The concentration of polymeric blends GGx/PVA has been set at 5% w/v because higher values have not produced any membranes due to high viscosity and due to conspicuous instabilities of the charged jet (data not showed). Considering Taylor's cone generation ability for the GG-C_{12}/PVA blends, polymer concentrations have been further reduced to 4% w/v, keeping the same weight ratio between GG-C_{12} and PVA. Distance, applied voltage, and flow rate have been appropriately tuned and summarized in Table 1 for each blend.

Table 1 Optimized electrospinning conditions in deionized water

Sample	***Spinning distance (cm)***	***Applied Voltage (kV)***	***Flow rate (ml/min)***
GG/PVA 5%	*10.0*	*10.0*	*0.13*
GG-C_8/PVA 5%	*10.0*	*15.0*	*0.25*
GG-C_{12}/PVA 4%	*12.0*	*15.0*	*0.25*

The collected membranes have been visualized under a SEM microscope. Every test conducted with GG/PVA blend, Figure 18a, has showed large globular stains, which came from the dripping of the needle, and an irregular morphology with segmented fibers and blobs has been noted. This result could be related to the short polymeric chains and the reduced generation of entangles as displayed in Scheme 3.

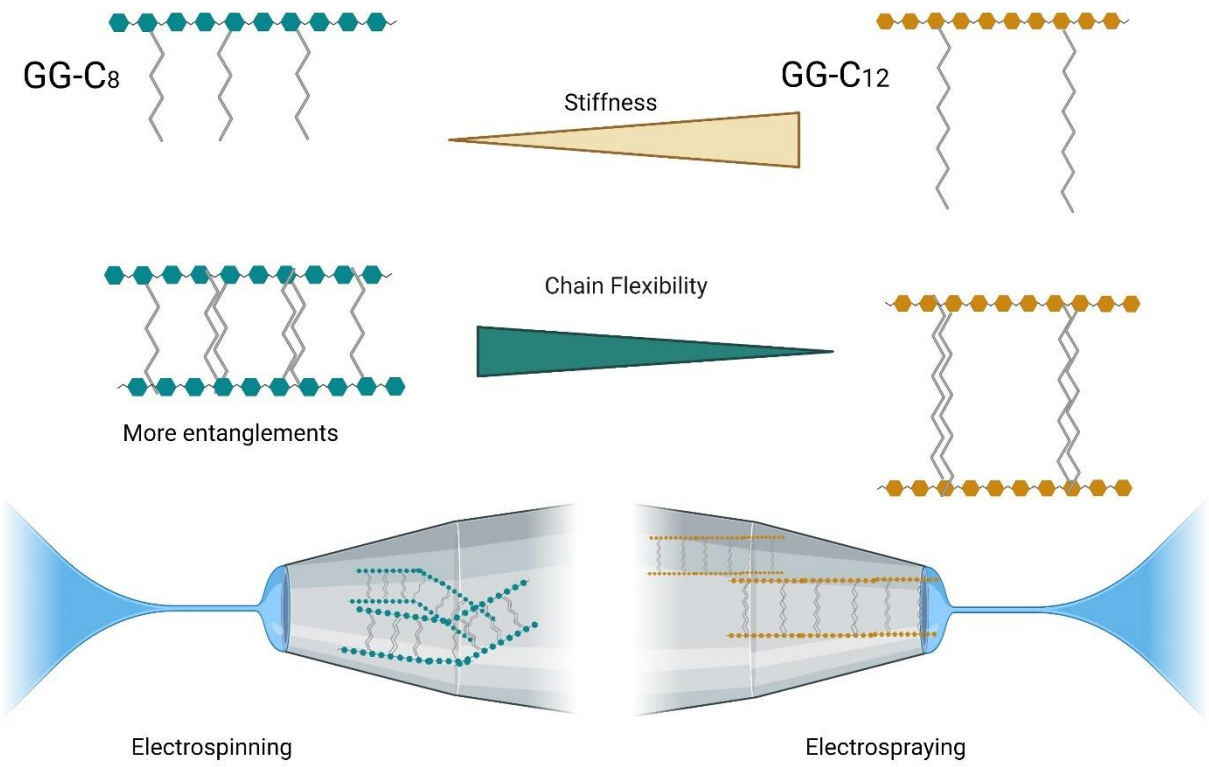

Scheme 3 Chain entanglements of gellan gum derivative in aqueous solutions.

The SEM micrograph of GG-C_8/PVA blend, processed as reported in Table 1, has been reported in Figure 18b showing a membrane with randomly deposed non-woven nanofibers. The pore size of this membrane has resulted to be 1.5 ± 0.6 µm.

The comparison of diameter size of fibers has highlighted the influence of applied voltages (15 and 20 kV) as shown in Figure 19. Although both applied voltages have generated nanofibrous mats with unimodal distributions (maxima centred at 200 nm), a narrower and more symmetric distribution has been observed, increasing the tension to 20 kV (Figure 19 blue bars). More than 66% of fibers have reported diameters in a small range (between 175

and 225 nm), demonstrating the suitable application of this membrane as a potential drug-eluting system with high control of the structure. By contrast, at lower values of applied voltage (15 kV), a wider range has been noted, where the half fibers counts have displayed diameters in the range 200-350 nm (Figure 19. red bars). In Figure 18c, the micrograph resulting from GG-C_{12}/PVA 4% w/v solution has been reported. All tests and those performed with optimized conditions (Table 1) have not determined any efficient deposition of nanofibrous matrices for GG-C_{12}/PVA 4% w/v solution. The effect should be attributed to the huge hydrophobic self-assembling degree of the polymer, which prevented the proper elongation of the charged jet.

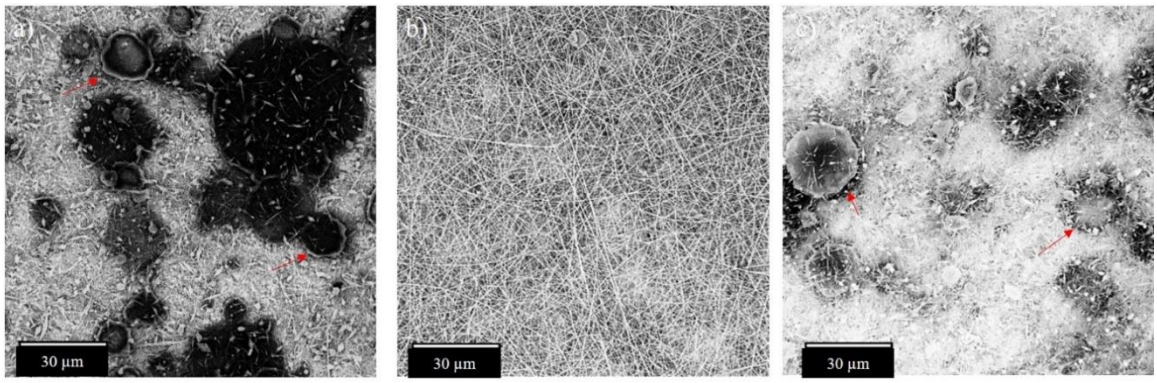

Figure 18. SEM micrographs of the electrospun mats from aqueous solutions. a)GG/PVA 5% w/v; b) GG-C_8/PVA 5% w/v; and c) GG-C_{12}/PVA 4% w/v. Red arrows indicated globular stains from dripping needle. Scale bar 30 µm

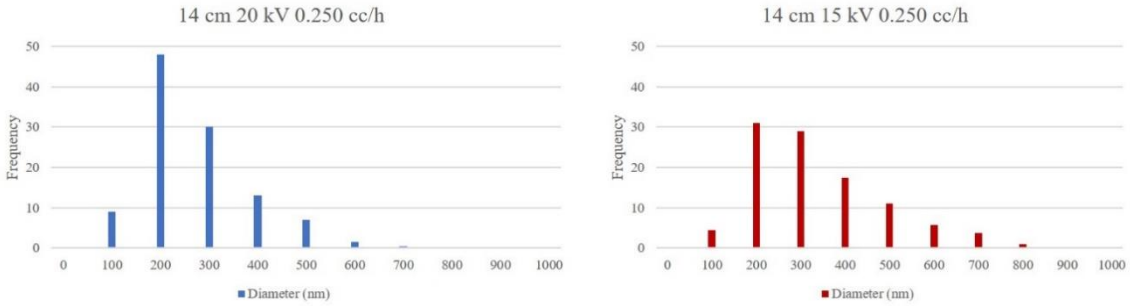

Figure 19. Dimensional distribution of nanofibers for electrospun mats of GG-C_8 /PVA 5% w/v in deionized water at 20 kV (blue bars) and 15 kV (red bars)

The improvement of spinnability of gellan gum derivatives has been tested by using the 95:5 v/v deionized water/ethanol mixture as reported previously in a similar work for other polysaccharides mixture (Ghafari *et al.*, 2020). Due to a vapour pressure higher than water, such volume ratio of the mixture has been wisely selected to favour the evaporation during ES processing and avoid the complete gelation of the polymers in dispersion. Although it represents a common strategy to improve the spinnability, it also reduces the blend conductivity. In Table 2, optimized instrumental parameters have reported.

Table 2. Ultimate electrospinning conditions in mixture water: ethanol 95:5 v/v

Sample	*Distance (cm)*	*Applied Electric Field (kV)*	*Flow rate (cc/h)*
GG	*10.0*	*10.0*	*0.20*
GG-C_8	*10.0*	*15.0*	*0.165*
GG-C_{12}	*12.0*	*10.0*	*0.25*

SEM micrographs have shown no improvements in spinnability, and no fibers have been collected for GG/PVA and GG-C_{12}/PVA blends (Figure 20, a-c). By contrast, GG-C_8/PVA 5% w/v dispersion (Figure 20 b) has generated a dense fibrillar matrix with a pore size of 1.8 ± 0.7 µm. The parameters listed in Table 2 have favoured the complete evaporation of both solvents for this sample. The analysis of the size distribution of fibers, Figure 21, showed unimodal behaviour with larger nanofibers (250-300 nm) compared to those obtained from aqueous blend.

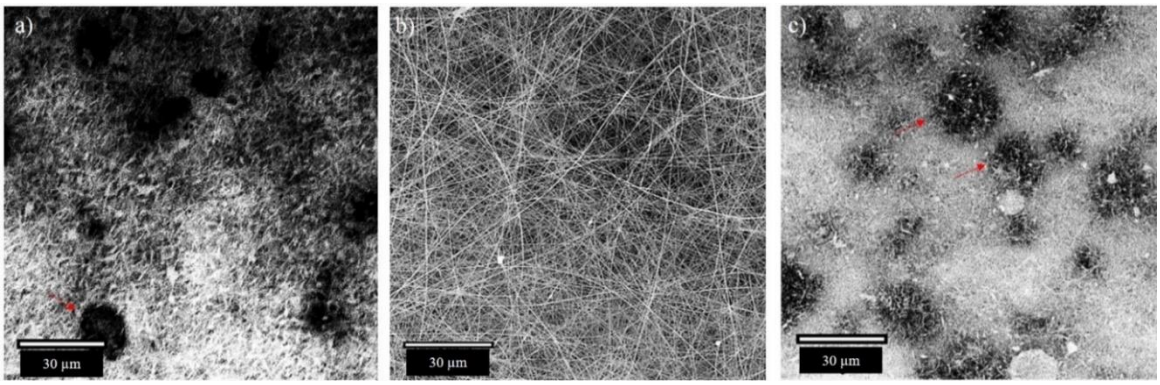

Figure 20. SEM micrographs of the electrospun mats from water:ethanol 95:5 v/v dispersions. a)GG/PVA 5% w/v; b) GG-C_8/PVA 5% w/v; and c) GG-C_{12}/PVA 4% w/v. Red arrows indicated globular stains from dripping needle

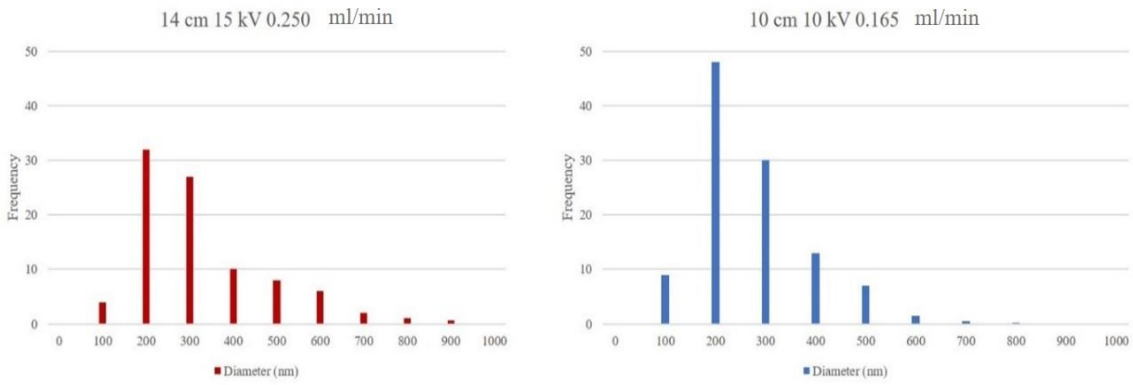

Figure 21. Dimensional distribution of nanofibers for electrospun mats of GG-C_8 /PVA 5% w/v from aqueous (red bars) and the binary mixture deionized water: ethanol 95:5 v/v (blue bars)

In particular, the use of different instrumental conditions ensured the electrospinnability of GG-C_8 blend by adjusting the distribution frequency of the mean diameters and the degree of homogeneity of the mats.

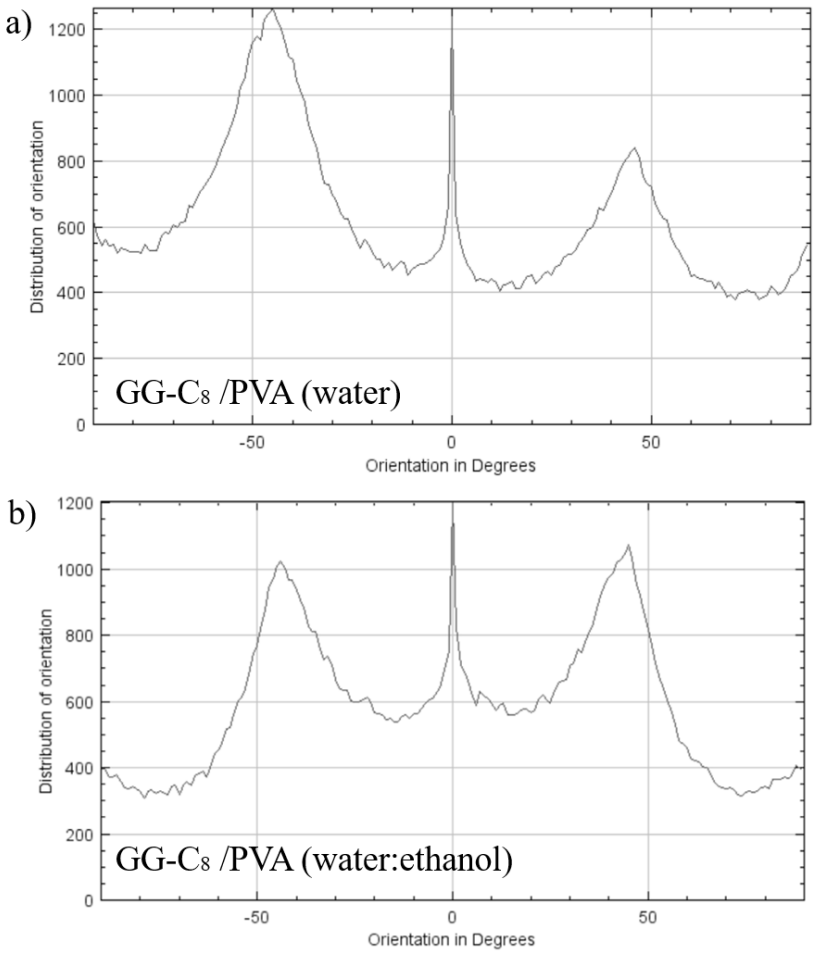

Figure 22. Orientation degrees of referred SEM micrograph in Figure 18 and Figure 20 for GG-C_8/PVA derivative processed in deionized water and in water/ethanol 95:5 v/v mixture.

A comparison of fiber orientation obtained from GG-C_8/PVA 5% w/v in water and water: ethanol 95:5 v/v mixture has been obtained from SEM micrographs and reported in Figure 22. The small addition of ethanol to the electrospinning blend GG-C_8/PVA (Figure 22 b) allowed a more homogeneous random deposition of fibers on the collector than the sample obtained from the deionized water dispersion (Figure 22 a).

During designing a scaffold for TERM applications, it is crucial to evaluate the swelling degree in an aqueous medium; in fact, the support should exert an essential role in solute transport and diffusion to maintain the viability of adherent cells. The swelling ability of GG-C_8 based membranes has been evaluated after 24 hours of immersion in Dulbecco's phosphate-buffered saline (DPBS) at pH 7.4 (Table 3) after ionotropic crosslinking with calcium chloride. The results, expressed as the weight ratio of the swollen to dried sample

(Q value) showed that the swollen weight is 9 and 6 times higher than the dry weight. As expected, the crosslinked membrane treated with $CaCl_2$ 1 M showed the lowest swelling degree due to the higher retention of Ca^{2+} ions and stability.

Table 3. Swelling degree expressed as Q value (swollen weight/dry weight)± standard deviation for crosslinked membranes with CaCl2 1 and 0.1 M in contact with DPBS pH 7.4 for 24 h

Scaffold	**Q value after 24 hours**
GG-C_8/PVA membrane (0.1 M $CaCl_2$)	9.1 ± 0.2
GG-C_8/PVA membrane (1 M $CaCl_2$)	6.7 ± 0.7

3.1.3 Viscoelastic behaviour of the polymeric dispersion in the binary mixture

The molecular weight, the temperature and the ionic strength of GG solutions influence The viscosity and gelation ability of GG. The thermally reversible gelation of gellan gum is one of the most relevant features of the polymer. The dispersion of the polymer occurs at 90°C, and, as the temperature decreased, free random coils start to interact in double-helices conformations and to aggregate in junction areas to form structured 3D networks. Contiguous carboxyl groups contribute to the gelation process by complexation of cations. An additional associative effect (hydrophobic aggregation) takes place in alkyl derivatives of gellan gum, whose intensity increases as a function of the length of the pendant chain, as demonstrable by pyrene assays (Agnello *et al.*, 2018). The hydrophobic aggregation interfers with the coil-to-helix transition of the GG partially, influencing the aggregation of GG coils in junction areas. In light of these considerations, rheological properties of polymeric dispersions in water/ethanol 95:5 v/v have been investigated. The graph, in Figure 23, highlighted differences bewteen samples that can be related to their ES performances. Considering the whole range of analysed frequency sweep (1 to 100 rad/s), blends have been classified in terms of descending complex viscosity as GG-C_8/PVA 5% w/v > GG-C_{12}/PVA 4% w/v > GG/PVA 5% w/v. At low frequencies, GG/PVA 5% w/v dispersion (black squares) has showed a Newtonian behaviour which could be related to a low density of interchain entanglements. This behaviour has probably determined the inability of processing such biomaterial by ES. GG-C_{12}/PVA 4% w/v in water/ethanol (red dots) has showed complex viscosity values higher than GG/PVA 5 % w/v but lower than GG-C_8/PVA. These data can be explained considering the stronger hydrophobic aggregation of the GG-C_{12} derivative in the GG-C_{12}/PVA blend, exalted by the non-solvent, which has caused a more intense chains aggregation but a high rigidity degree of the chains which has prevented the entanglements and hindered the spinnability of the blend. GG-C_8

sample (blue triangles) showed the highest value of complex viscosity reported. In this case, the addition of ethanol has favored tangles between polymer chains with a positive effects on its processability, compared to samples treated with water, and it has allowed to modulate the structure of the fibers in the membrane, in terms of size distribution and orientation.

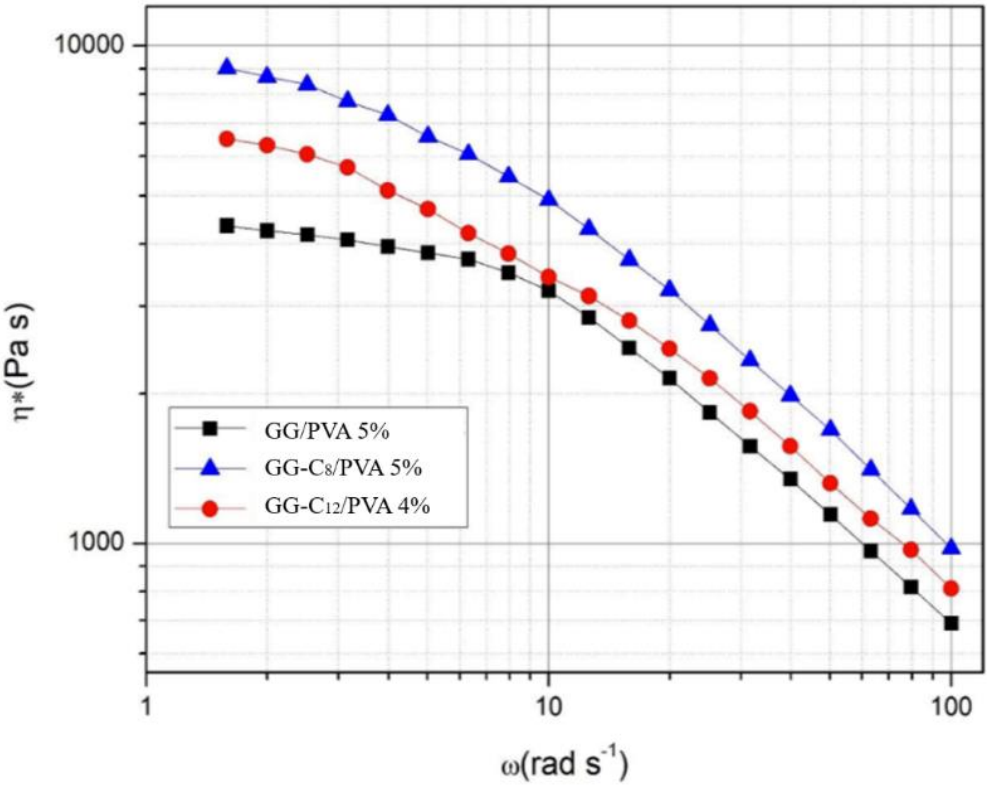

Figure 23. Flow curves of gellan gum and its derivatives in water:ethanol 95:5 v/v at 25°C

3.2 Asymmetric dual-layer device for in situ regeneration of skin

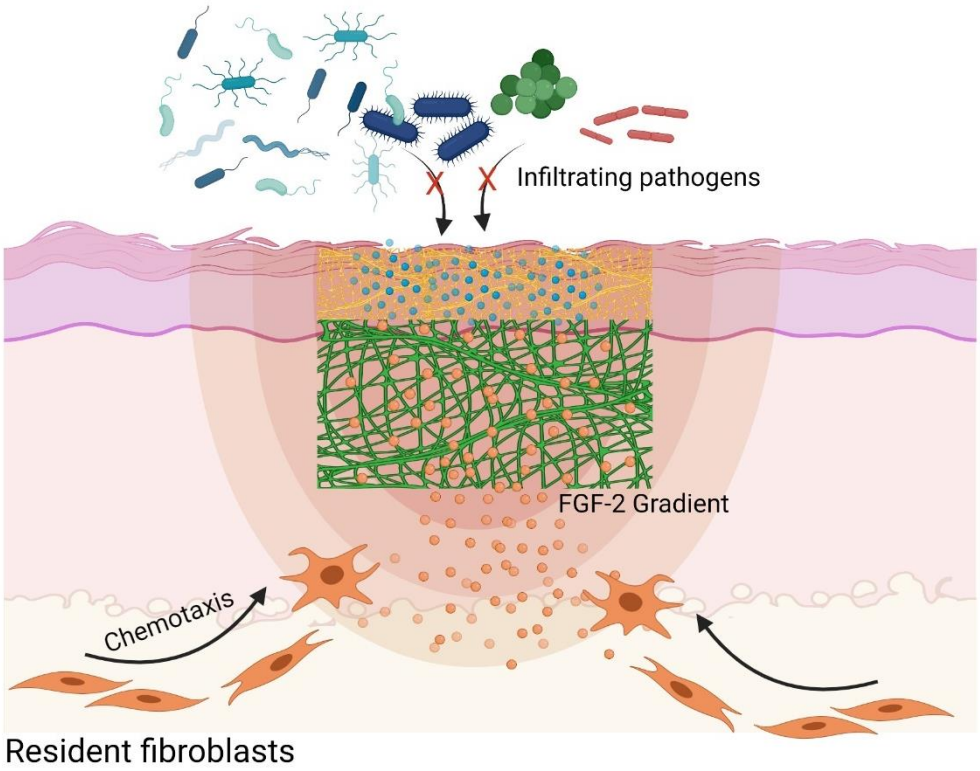

Scheme 4. Representation of asymmetric bilayer device for wound healing application. Dermal layer (GG-C_8) is the green network with orange particles (FGF-2) , skin layer (PCL/PU) isthe yellow network with blu particles (ciprofloxacin).

3.2.1 Set-up of electrospinning parameters, loading of bioactive molecules and fabrication of the double-layer electrospun membrane

Polysaccharide hydrocolloids represent a suitable choice to produce the dermal layer in an asymmetric membrane as discussed in the Introduction. In particular, polysaccharides produce a hydrated network over the tissues, which adsorb wound exudates, retaining moisture and avoiding excessive water loss (Saghazadeh *et al.*, 2018). Furthermore, hydrocolloids offer the opportunity to load bioactive factors, improving their stability (Malafaya, Silva and Reis, 2007; Lai *et al.*, 2014), controlling the release to the surrounding environment. Polar functional groups of hydrocolloids could interact with growth factors, thus reducing the rate of diffusion and sustaining their release. Gellan Gum has already been proposed as a mucoadhesive constituent for wound dressings and, like other ionotropic polysaccharides, has a good affinity for water

and has showed good biocompatibility (Souza *et al.*, 2014; Ismail *et al.*, 2019). Considering previous results of the processing gellan gum derivatives and in light of good physical behaviour concerning the octyl derivative of gellan gum, i. e. GG-C_8, this sample has been chosen as an appropriate main component of the electrospun dermal membrane (Agnello, Gasperini, *et al.*, 2017). GG-C_8 blends have been processed using a custom system. Scheme 5 illustrated the custom instrument employed.

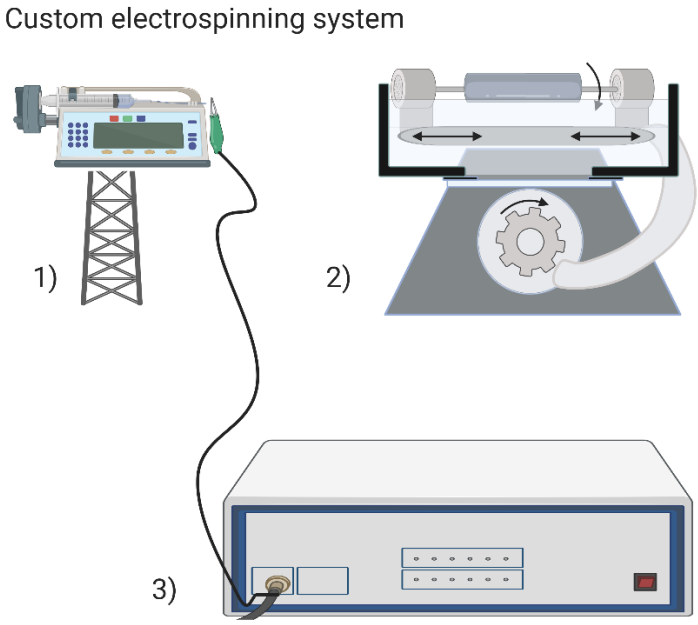

Scheme 5. Custom electrospinning instrument. 1) Syringe pump; 2) Translational and rotational cylindric collector; 3) Electrical generator

The electrospinning of the GG-C_8 derivative has been performed thanks to the presence of the polymeric carrier PVA added in an equal weight ratio concerning the GG derivative, in agreement with processing experience acquired and the results of other authors (Vashisth *et al.*, 2014). In previous fabrication tests, the 8-carbons derivative of gellan gum has showed enhanced electrospinning performances that have been correlated to the appropriate aggregation of chains, i.e. hydrophobic interactions, respect unfunctionalized polysaccharide and other derivatives with more extended alkyl chains. Since electrospinning of

polysaccharides in aqueous dispersion offers a safe strategy to avoid denaturation of bioactive factors (Jin, Molamma P. Prabhakaran, *et al.*, 2013; Lai *et al.*, 2014; Selcan Gungor-Ozkerim *et al.*, 2014; Miguel *et al.*, 2018), FGF-2 has been incorporated into the aqueous mixture of GG-C_8/PVA before electrospinning. A loading of FGF-2 equal to 11 ng ± 0.2 per mg of polymers (GG-C_8 plus PVA) has been achieved on the dried electrospun layer, representing a loading efficiency of 44%. SEM analyses have showed fibers with a diameter of 180 ± 10 nm and beads in electrospun GG-C_8/PVA layer both in the absence (Figure 24 a) and in the presence of growth factor (Figure 24 b).

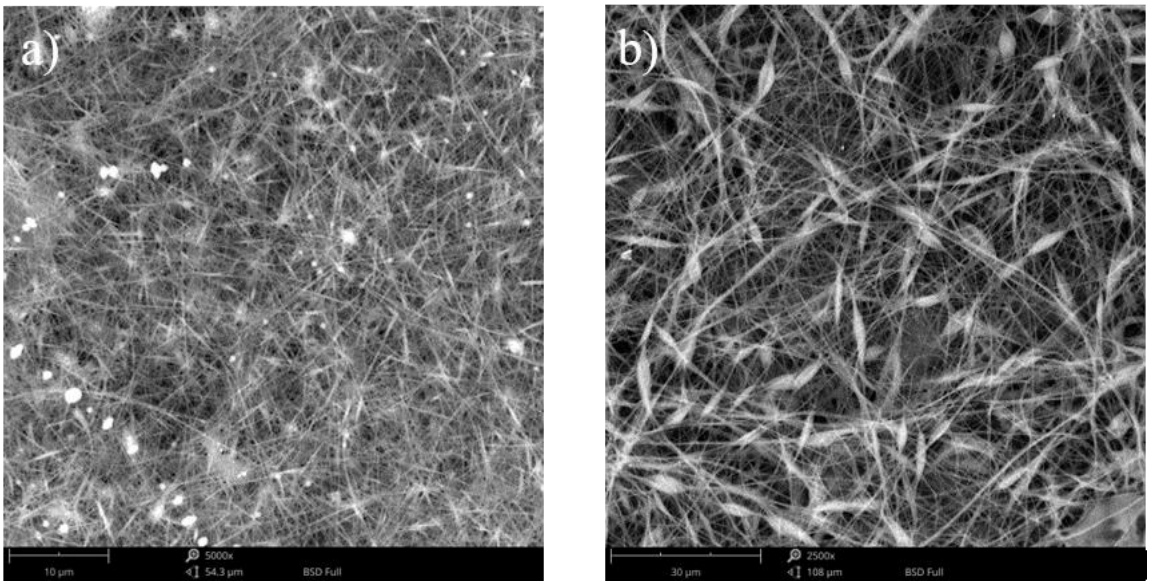

Figure 24. SEM micrographs of: a) GG-C_8/PVA electrospun layer; b) GG-C_8/PVA electrospun layer with FGF-2

The fabrication of the PU-PCL layer, also referred to as the skin layer, has been performed using a polymer concentration of 5% w/v in polar aprotic solvents, like N,N-dimethyl formamide (DMF) and dimethylacetamide (DMA). However, the use of DMF or DMA alone has produced wet electrospun mats (Figure 25 a). The addition of THF has improved the spinnability (favouring solvent evaporation), producing dry elastic mats with a fibrillar structure (Figure 25 b). Table 4 reports the best electrospinning conditions assayed for both hydrophilic and hydrophobic layers.

Table 4. Electrospinning conditions for the fabrication of hydrophilic and hydrophobic layers of the asymmetric membrane

Sample	***Solvent***	***Distance (cm)***	***Feed rate (ml/min)***	***Applied electric field (kV)***
GG-C_8/PVA 4% w/v	Deionized water	14	0.0085	22.5
PU-PCL 5 % w/v	DMF or DMA	10	0.009	17
PU-PCL 5 % w/v	DMF:THF 1:1 or DMA:THF 1:1	20	0.01	10

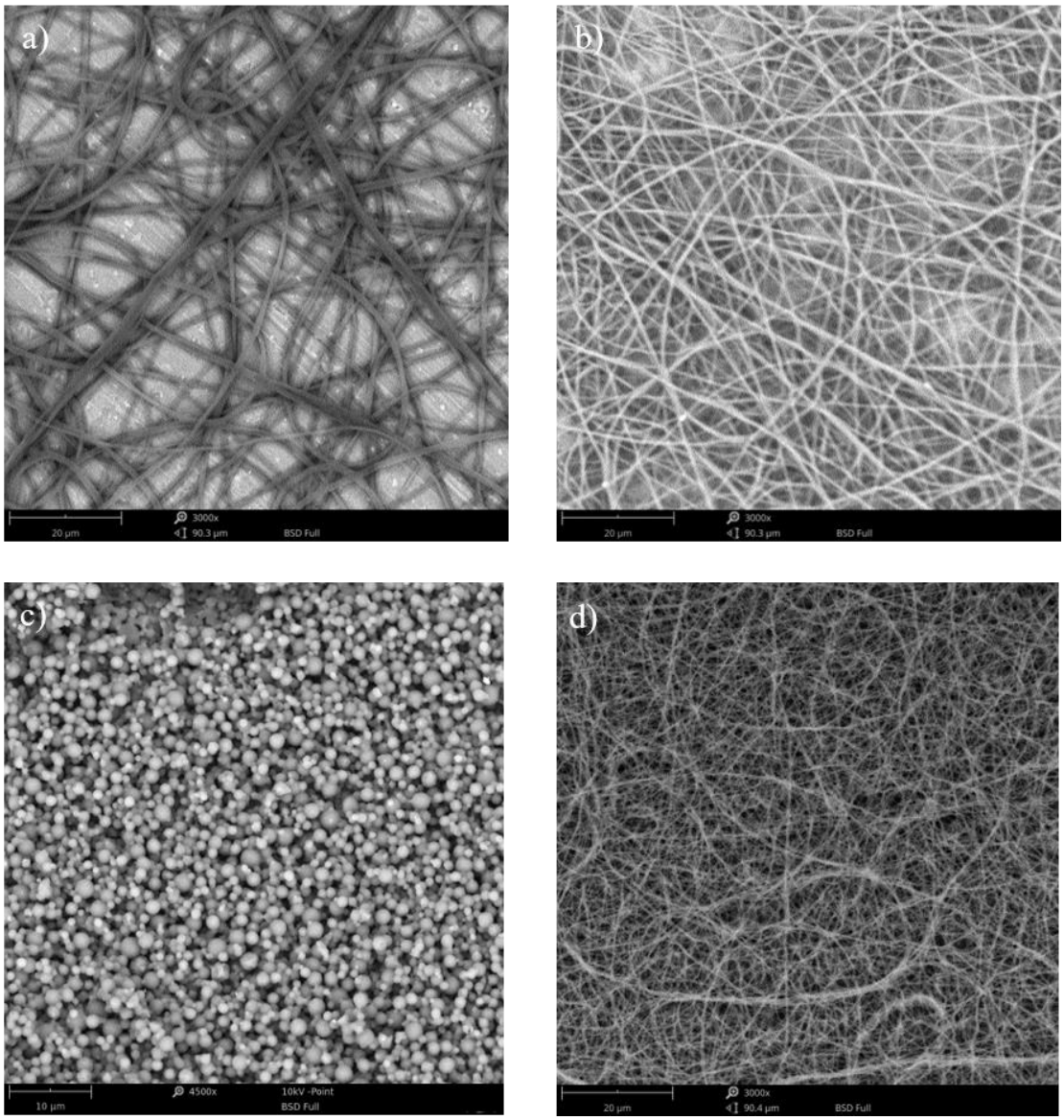

Figure 25. SEM micrographs of: a) PU-PCL electrospun layer from DMF solution; b) PU-PCL electrospun layer from DMF: THF 1:1 v/v mixture; c) dried CPX MPs produced by spray drying technique; d) PU-PCL electrospun layer loaded with CPX

Ciprofloxacin (CPX) is an antibiotic employed for the treatment of wound infections, acting against Gram-positive and Gram-negative pathogens with low minimum inhibitory concentrations (MIC) (Tsou *et al.*, 2005). Several examples of electrospun membranes containing CPX have recently been designed (Chen *et al.*, 2016; Shi *et al.*, 2018; Yang, Zhang and Zhang, 2019). It is known that loading of drugs into electrospun biomaterials can be carried out by physical absorption or by direct solubilization during the electrospinning procedure (Buck *et al.*, 2018). For CPX, a sustained drug release can be achieved by direct entrapment during fabrication, although the low solubility of the drug, as the zwitterionic form in the aqueous medium, limits this procedure. Once incorporated into the electrospinning mixture, CPX could crystallize, resulting in a less soluble species, thus producing a too low local antibiotic concentration, which might be related to the appearance of antibiotic-resistant strains (Ahire *et al.*, 2015; Buck *et al.*, 2018). These disadvantages could be overcome by the production of amorphous solid saline dispersions (ASSD), which allowed for more excellent solubility and faster dissolution of the drug, increasing the antibiotic concentration in aqueous solutions. Polyvinyl pyrrolidone (PVP) could stabilize the dispersion of amorphous solid salts by reducing the molecular mobility of the drug, thus increasing the energy barrier for recrystallization. In particular, the amorphous solid dispersion of PVP/ciprofloxacin hemisuccinate has been used to improve the water solubility of this drug (Mesallati and Tajber, 2017). Here, amorphous solid dispersions of PVP/ciprofloxacin hemisuccinate, produced and isolated as microparticles (CPX MPs) by spray drying technique (see Figure 25 c), have allowed the solubilization of the drug in the solvents used for PU-PCL electrospinning. The drug loading of CPX in microparticles has resulted in 55 ± 2 w/w%

A nominal concentration of ciprofloxacin of 2 % w/w (mg CPX/mg PU-PCL) has been loaded in the electrospinning solution. The total amount of drug detected in the electrospun product resulted in a reproducible loading efficiency of 100%.

The double-layered membrane, produced as reported in the Experimental section, has been shown in Figure 26. Preliminary tests have determined the deposition order of the layers. Briefly, once the polyurethane layer has been deposed on the collector, the following deposition of the polysaccharide layer has showed very low efficiency. In this case, the polyurethane layer probably acted as isolating electrical barrier, and no new optimized instrument parameters have been found. Moreover, the proper deposition order has resulted as PCL-PU layer above dermal layer because it has not required any parameter changes, especially for the ES of GG-C_8, and it has been selected as the final fabrication method. Figure 26 a and c show the complete asymmetric membrane, while Figure 26 b shows the SEM image of the membrane section. A thick hydrophilic layer of GG-C_8/PVP (400 μm) has been fabricated in contact with a thin hydrophobic PU-PCL layer (≅ 50μm).

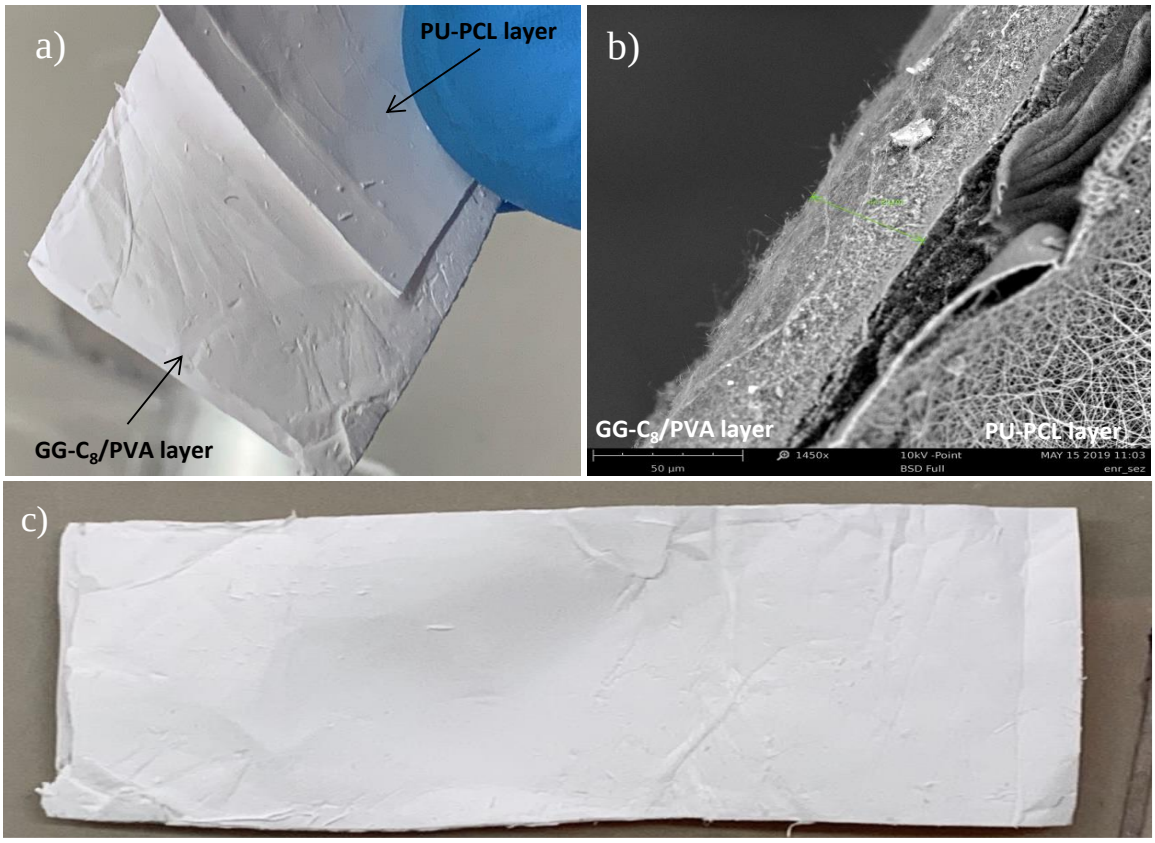

Figure 26. (a) Image of the folded double-layer electrospun membrane. (b) SEM image the cross-section between the two layers (c) Image of complete dried double-layer electrospun membrane

In Figure 26 b, the boundary between the two layers has been noted. Macroscopically (Figure 26 a and c), in dry conditions, the two layers are sealed, and their manipulation has not altered the integrity of the double layer. Once applied to the wound, the hydration of the dermal layer could reduce the adhesion between membranes, thus allowing the peeling-off of the epidermal layer; thus it can be removed without apporting any damage to the wound and it should be replaced by a new membrane for a prolonged treatment (Lin *et al.*, 2015).

3.2.2 Characterization of double-layer electrospun membrane

The swelling ability of prepared membranes was evaluated after 24 hours of contact with DPBS pH 7.4. The swelling degree, expressed as q value, resulted equal to 9.1 ± 0.2 and 6.7 ± 0.7 for membrane crosslinked with CaCl2 0.1 and 1 M, respectively. As expected, the more crosslinked membrane, treated with CaCl2 1 M, showed the lowest swelling degree due to the higher retention of calcium ions and stability. Water vapor transmission rate (WVTR) value of 3212 ± 300 g/m2·24 h was found for double membrane. As recently discussed(Xu *et al.*, 2016), a medium permeable wound dressing with a value of WVTR of 2000 g/m2·24 h allows proliferation and regular function of epidermal cells and fibroblasts. The found value of WVTR corresponds to a high permeability membrane; thus excessive evaporation of water from studied membrane should occur, but it resulted still efficient in maintaining maximum proliferation of epidermal cells and fibroblasts. Data on the degree of swelling and the WVTR studies suggested that the double-membrane proposed should absorb huge amounts of exudates thanks to the presence of the GG-C8/PVA hydrocolloid, reducing excessive water loss.

The dissolution of GG-C_8 and the release of the CPX and FGF-2 have been evaluated *in vitro* using Franz cells equipment. In particular, in order to mimic the application of the asymmetric membrane on the wound, the double-layer membrane has been placed on the orifice of the Franz

cell by applying the hydrophilic layer GG-C_8/PVA in contact with the PBS pH 6.8 and the hydrophobic PU-PCL layer in contact with air and conditioned at 35°C.

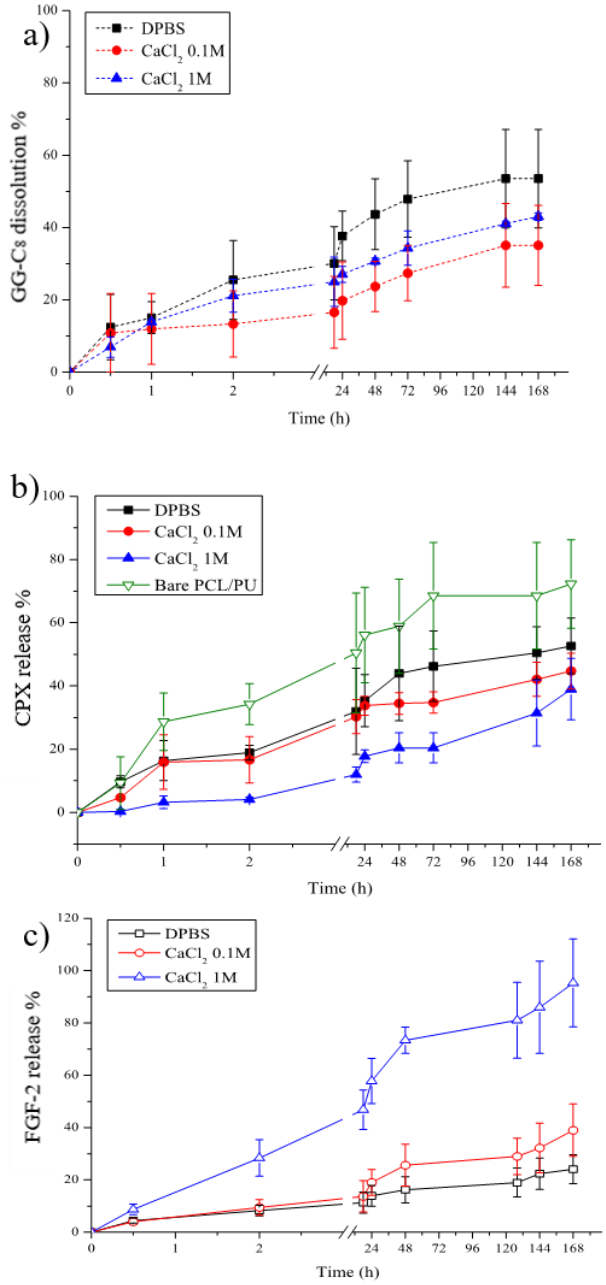

Figure 27. Franz cells experiments. a) GG-C_8 dissolution%; b) CPX release %; c) FGF-2 release % detected in the acceptor compartment as a function of time. Data are represented as mean values ± standard deviation

As showed in Figure 27, exploiting the ionotropic properties of the GG-C_8 derivative, it has been possible to control the dissolution of the polysaccharide layer and the release profiles of both CPX and FGF-2. After one week in DPBS pH 7.4, about 55 % of GG-C_8 dissolved, while the crosslinking with $CaCl_2$ significantly has improved the hydrophilic layer stability, reducing

its dissolution to 30 % and 40% respectively for samples crosslinked in $CaCl_2$ 0.1 M and 1 M ($p < 0.005$ from 24 to 168 h; differences between $CaCl_2$ crosslinked samples were not statistically significant). This trend resulted in agreement with previous works where it has been demonstrated that the insertion of C_8 chains has not interfered with the native ionotropic crosslinking of gellan gum (Agnello *et al.*, 2018) and that the strength of ionotropically crosslinked hydrogels based on gellan gum increased proportionally according to the calcium concentration only in a specific range (Tang *et al.*, 1994).

As represented in Figure 27 b, the CPX release profiles from double-layer membrane have been compared to the release of CPX from the PU-PCL layer alone; in particular, 70% of the loaded drug has been released from this latter sample after one week according to the amorphous state of CPX. In the double-layer membrane, the hydrophilic layer has progressively prolonged the release of the drug by significantly reducing its diffusion as a function of the increased crosslinking of the hydrophilic layer (50, 40, and 38 % of CPX release after one week, respectively for samples treated with DPBS, $CaCl_2$ 0.1 and $CaCl_2$ 1 M; $p < 0.005$, from 1 to 72 hours and $p<0.01$ at 144 hours and 168 hours comparing bare PU-PCL with samples treated with DPBS, $CaCl_2$ 0.1 and $CaCl_2$ 1 M).

As the $CaCl_2$ concentrations in the crosslinking medium raised as the rate of FGF-2 released increased. In particular, after one week, the growth factor released resulted equal to 20%, 40% and 100% for samples treated with DPBS, $CaCl_2$ 0.1 and $CaCl_2$ 1 M, respectively ($p<0.005$ comparing DPBS treated sample with $CaCl_2$ crosslinked samples). FGF-2 is a highly positively charged protein capable of interacting with the sulfate and carboxylate groups of polysaccharides (Malafaya, Silva and Reis, 2007; Nguyen *et al.*, 2017). The higher aggregation and the shielding effect on the glucuronic acid groups due to Ca^{2+} ions should explain the enhanced release of FGF-2 with the increased $CaCl_2$ concentration used to treat membranes.

The dissolution of GG-C_8 and the release profiles of CPX and FGF-2 has showed how the ionotropic behaviour of the gellan gum derivative could be effectively exploited to control the

release of active ingredients loaded in the double-layer membrane. In particular, two main factors have influenced the release of bioactive molecules: a) the ionic interactions between GG-C_8 and the growth factor, which are dependent on the concentration of $CaCl_2$, b) the compactness of the hydrogel dependent on the ionotropic crosslinking of GG-C_8, which regulates the diffusion of the antibiotic.

3.2.3 Cytocompatibility assay

NIH 3T3 cell line has been directly cultured above the hydrophilic layer of the double-layer membrane crosslinked with $CaCl_2$ 1 M, both free and loaded with FGF-2, until seven days. Cell metabolic activity has been evaluated through MTS assay, and results reported in Figure 28. Both samples investigated resulted compatible with the cells and, as expected, a significant increase ($p < 0.05$) in cell viability has been found for the sample containing the FGF-2 that has promoted cell adhesion ($p<0.05$) (Selcan Gungor-Ozkerim *et al.*, 2014; Bai *et al.*, 2018). On the other hand, obtained results have suggested that CPX release probably has not decreased the metabolic activity of fibroblasts.

Viability on FGF-2 loaded sample increased progressively during seven days of culture, reaching values comparable to that obtained on TCP, used as a comparison. The comparison with the growth factor-free sample has showed how FGF-2 significantly promoted adhesion and viability of cells after 1 and 3 days of culture ($p<0.005$) according to published results. (Selcan Gungor-Ozkerim *et al.*, 2014; Bai *et al.*, 2018). The data obtained also suggested that the release of CPX probably did not adversely affect the metabolic activity of the fibroblasts.

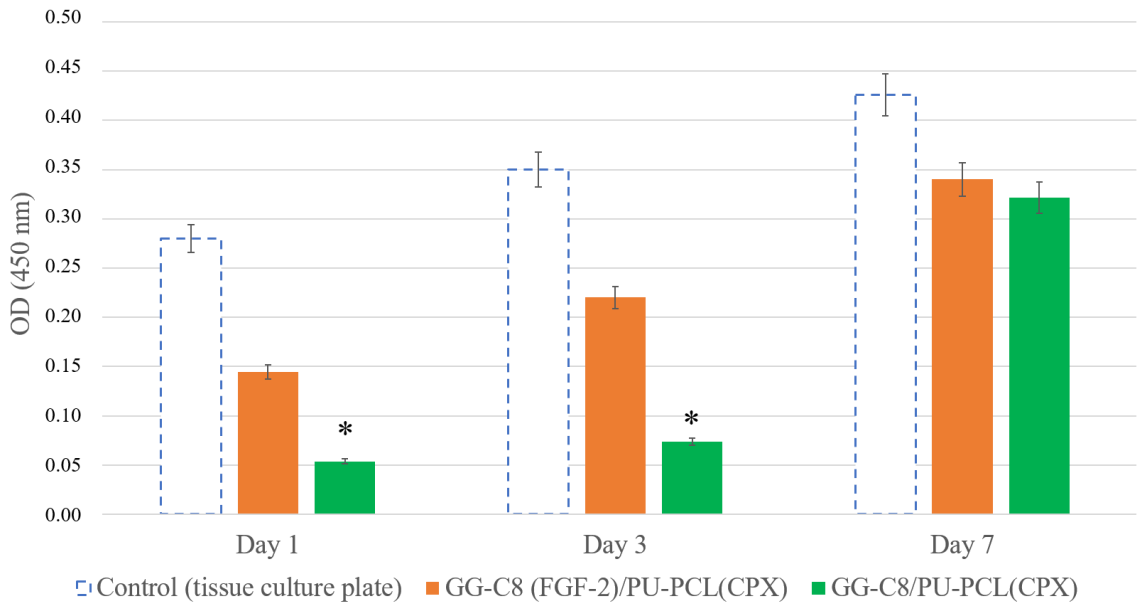

*Figure 28. MTS assay on NIH 3T3 fibroblasts cultured on FGF-2 loaded and FGF-2 free double-layer membranes as a function of time. Data represented as the mean value of absorbance at 492 nm ± SD, comparing as a control fibroblasts growing directly on TCP 48 well. The symbol * highlighted the statistically significant absorbances read on membrane free of FGF-2 compared to the membrane loaded with FGF-2 ($p< 0.005$)*

3.2.4 Antibacterial activity

Logarithmic (log) reduction has been used to quantify the antibacterial activity against *S.aureus* ATCC 25923 of starting membrane loaded with antibiotic CPX (2% w/w) (t0) and membranes recovered after 7 (t7) and 14 (t14) days from *in vitro* release experiments (Figure 29). The membrane having the fastest CPX release profile, i.e. the sample incubated directly in DPBS (without treatment with $CaCl_2$), has been assayed to detect the *in vitro* antimicrobial efficiency. The membrane has demonstrated a significant increase in log reduction after 48 hours of incubation showing a strong antibacterial activity according to the release profile, being about 50 % of drug released after this time. Instead, membranes recovered after 7 and 14 days of release resulted slightly active, thus suggesting that an almost complete release of antibiotic has been reached after this time. This evidence should be intended as a positive result; in fact, it is known that an immediate rapid release of antibiotic is necessary to achieve adequate wound protection during the first 48 hours of

treatment and that a prolonged release of low concentration antibiotic could favour the selection of resistant bacteria (Ahire *et al.*, 2015). The results are particularly encouraging because *S.aureus* is the most frequent cause of delayed healing of wounds and wound associated infections, such as diabetic foot, venous leg and pressure ulcers (Frykberg and Banks, 2015).

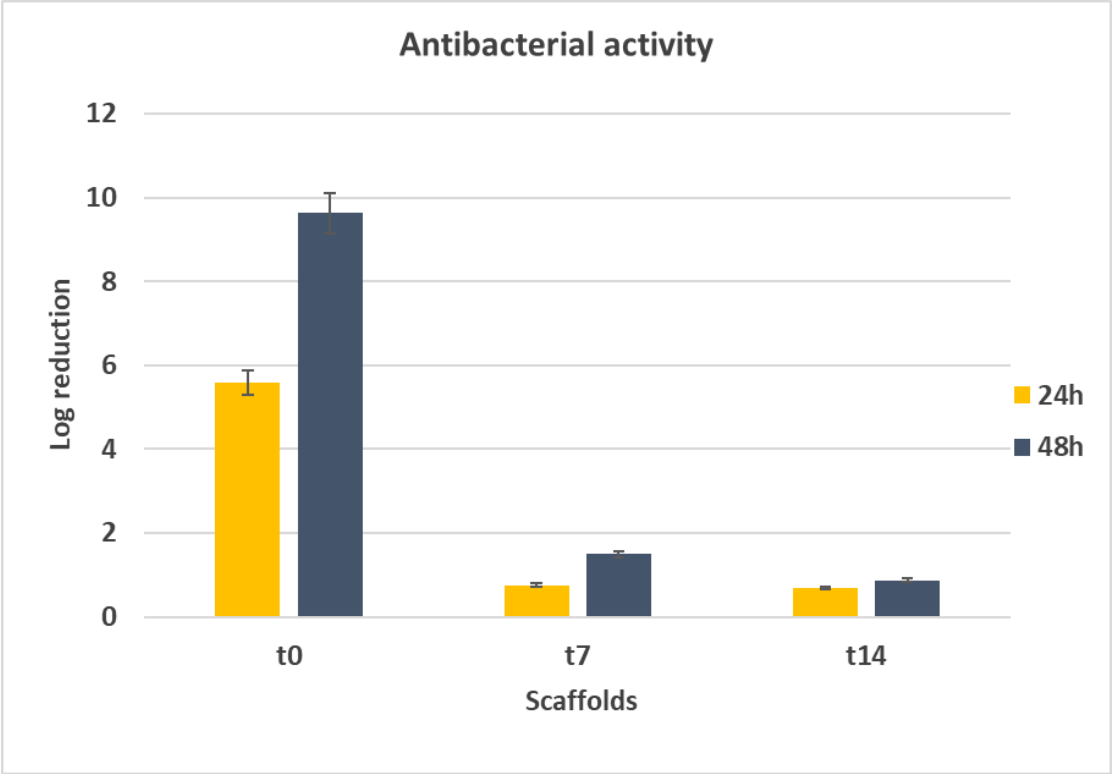

Figure 29. Antibacterial activity against S. aureus ATCC 25923 of membrane loaded with antibiotic CPX (2% w/w) (t0) and membranes recovered after 7 (t7) and 14 (t14) days from in vitro release experiments. Histograms show the logarithmic reduction of growth of S.aureus at different incubation times (24 and 48 hours)

3.2.5 Scratch test and cell chemoattraction assay

Scratch test, reported in Figure 30, was an exemplary assay to evaluate the wound closure. It is evident that the wound closure is in agreement with the release of FGF-2 from the investigated membranes (treated with DPBS alone or crosslinked with $CaCl_2$ 0.1 and 1 M). Indeed, the most rapid wound closure occurred already after 24 hours for the sample

crosslinked with $CaCl_2$ 1M according to the increased amount of FGF-2 released (see Figure 27 c). At the end of the experiment (72 hours), the initial scratch has been entirely covered by the cells also for the sample crosslinked with $CaCl_2$ 0.1M while the closure of the scratch resulted incomplete for the control and for the sample treated with DPBS alone.

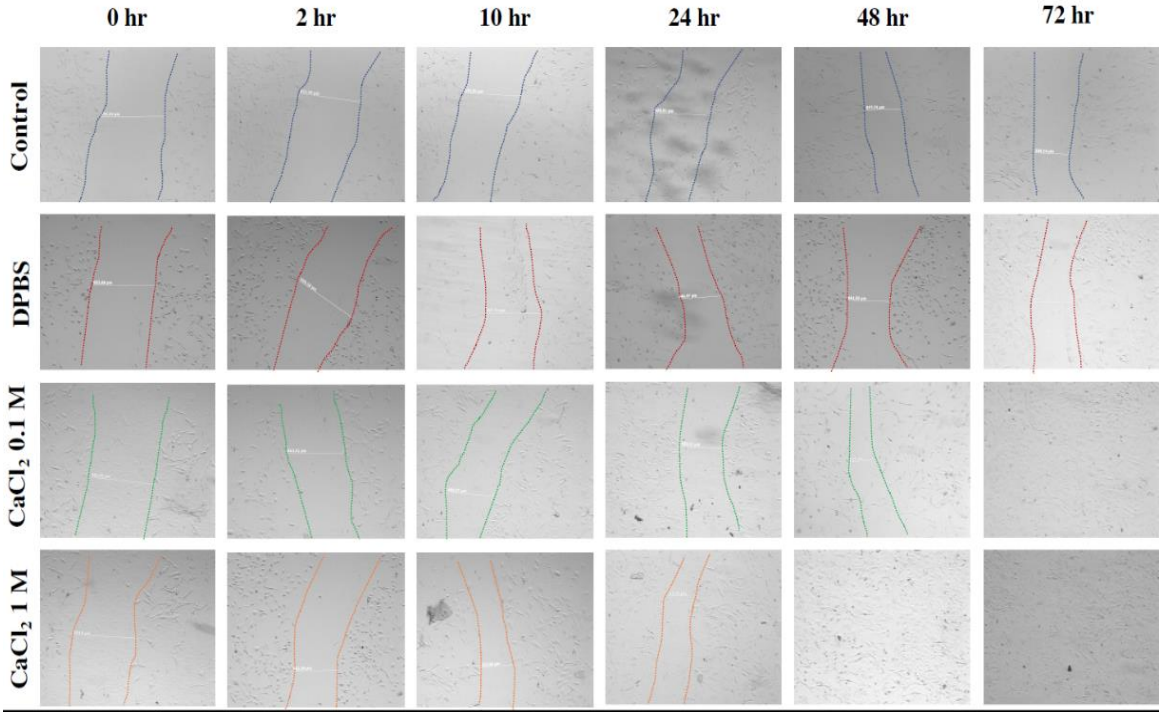

Figure 30. Scratch test performed on NIH 3T3 fibroblasts incubated with the medium conditioned for 24 hours by round-shaped double-layer membranes (loaded with FGF-2 and CPX) treated with DPBS alone or crosslinked with CaCl2 (0.1 M or 1M). Cells cultured with serum-free DMEM were used as a control

Finally, a cell chemoattraction assay has been performed using transwell inserts as illustrated in Scheme 6. In this test, an artificial extracellular matrix (Matrigel^{TM}) has been interposed between the membrane (treated with DPBS alone or crosslinked with $CaCl_2$ 0.1 and 1M) and the cells as a diffusion substrate to test for the generation of a growth factor gradient capable of stimulating cell migration through the matrix.

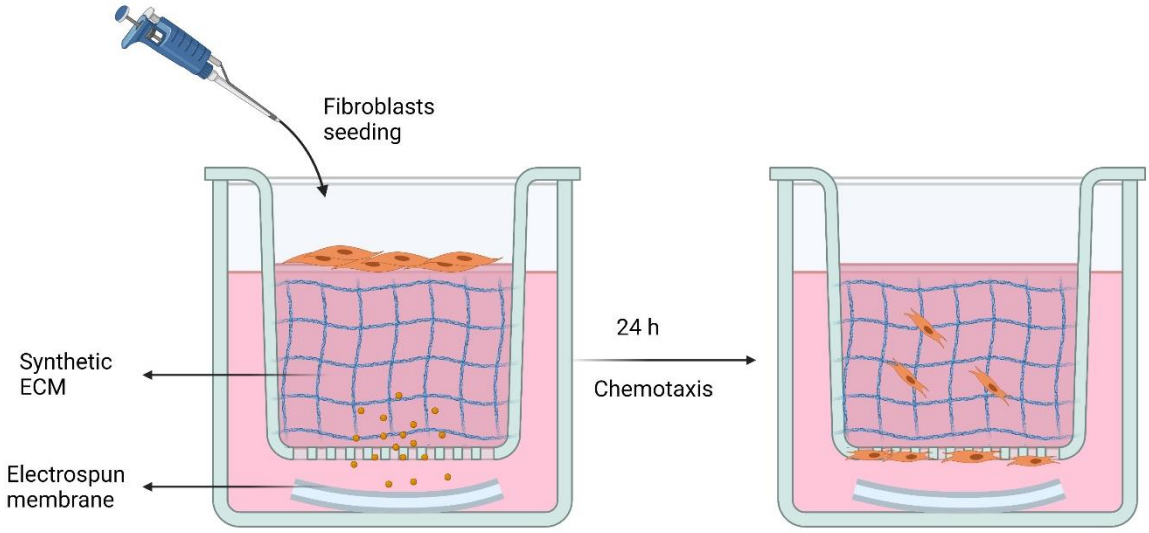

Scheme 6. Invasion assay performed with NIH-3T3 fibroblast line

As shown in Figure 31, the chemoattraction of the fibroblasts resulted in agreement with the release of FGF-2 (Figure 27 c); in fact, no cells have been detected both for the control and for the sample treated with only DPBS (Figure 27 a) due to the low release of FGF-2. The massive release of FGF-2 (approximately 50% w/w after 24 hours) has been obtained from the sample crosslinked with $CaCl_2$ 1M, which has allowed a rapid cell recruitment. Such results have confirmed that the bioactivity of FGF-2 has not been affected by the electrospinning and the crosslinking procedures. The hydrophilic layer has improved the storage of the bioactive FGF-2, which has generated a gradient able to stimulate cell recruitment. The exposure of the membrane to a medium with controlled ionic strength and concentration on $CaCl_2$ could be potentially exploited to tune the release of the growth factor, thus influencing cell recruitment.

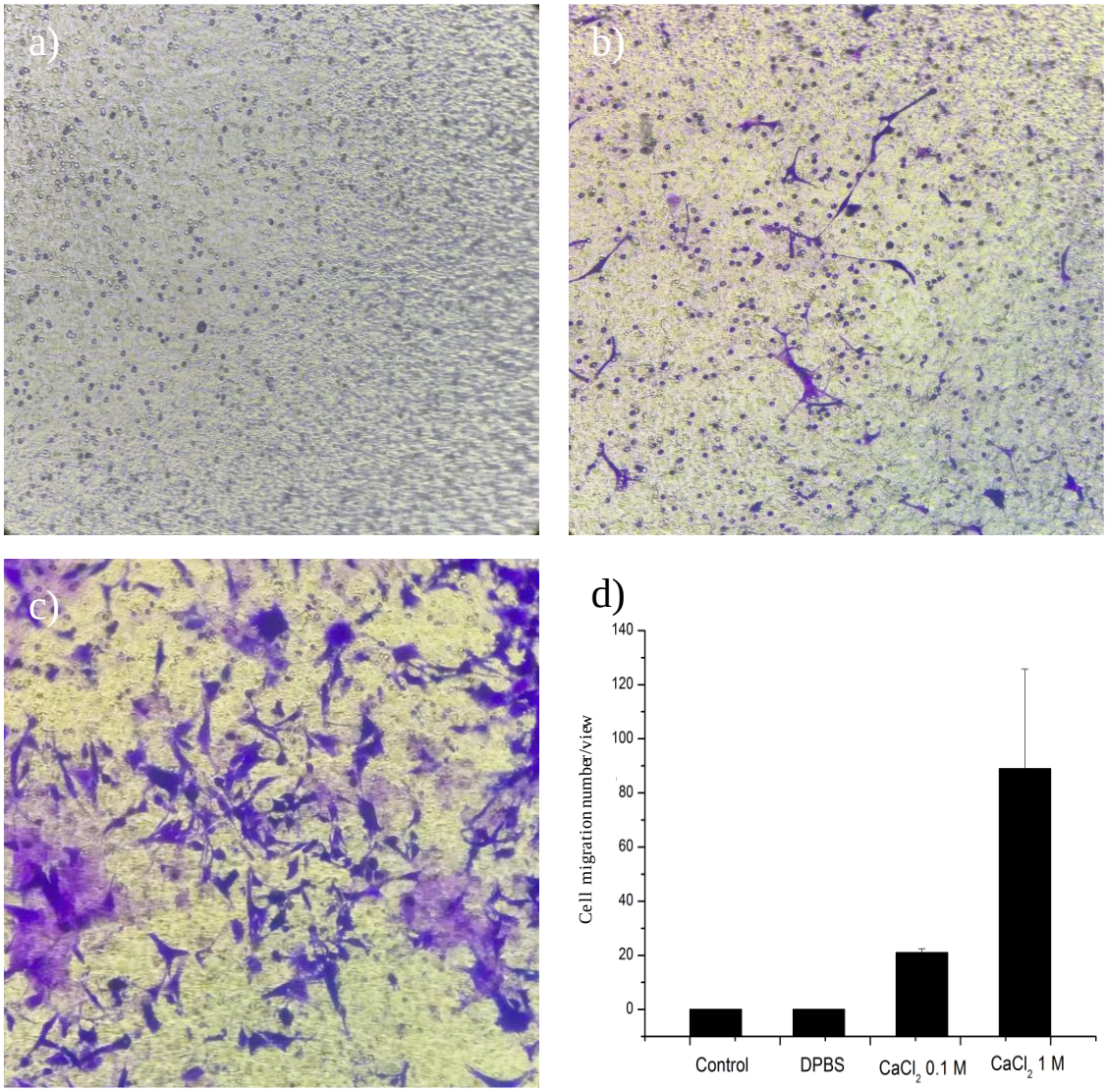

Figure 31. Images of NIH 3T3 fibroblasts migrated through a MatrigelTM layer in contact with double-layer membranes loaded with FGF-2, and CPX treated with DPBS alone (image a) or crosslinked with CaCl2 0.1 M (image b) and 1 M (image c). Cell migration number per field for all investigated sample (image d). Data were represented as mean value ± standard deviation

3.3 Fabrication of electrospun membranes based on hyaluronan derivatives for periodontal regeneration

The interest of processing different hyaluronic acid derivatives in electrospun membranes was to achieve thin mechanical barriers for Guided Bone Regeneration. For this application, membranes should be applied surgically between the gingival epithelium and the connective tissue. The electrospun pattern could isolate bone and periodontal ligaments and prevent epithelial migration and infiltration in the periodontal tissue. In addition, the increasing hydrophobic character of hyaluronan derivatives has been analyzed in terms of drug-eluting features of an osteoinductive active as illustrated in Scheme 7.

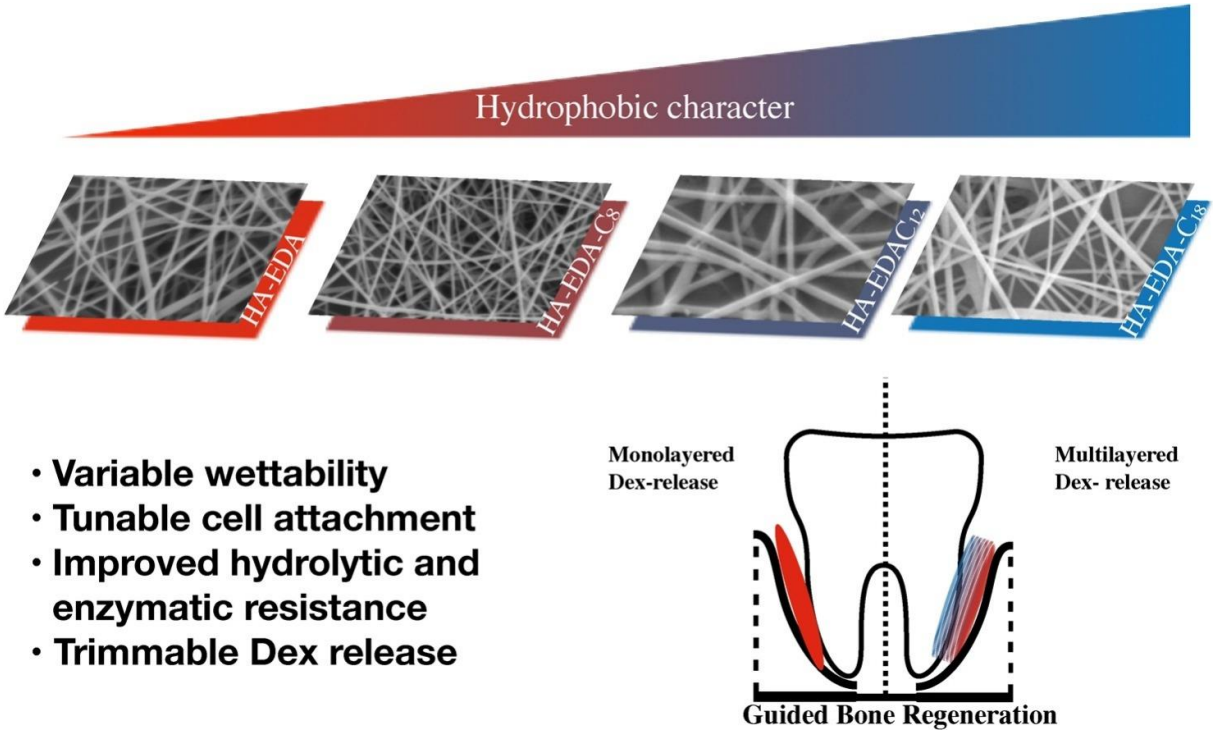

Scheme 7. Periodontal application of electrospun membranes based on hyaluronic acid derivatives

3.3.1 Physico-chemical characterization of HA derivatives

Hyaluronic acid has been degraded in acidic conditions and converted in the tetrabutilammonium salt to favour the following derivatization. HA chemical modifications have been carried out in dimethyl sulfoxide (Scheme 8) via 4-NPBC activation (Giammona, Palumbo and Pitarresi, 2009). Four hyaluronic acid derivatives have been produced and characterized; three of them bearing free amino groups and alkyl moieties (C_8, C_{12} and C_{18}) and the fourth one with free amino groups. (HA-EDA) Table 5 resumes the derivatization degree expressed in terms of moles per cent of EDA and alkyl moieties, both calculated as mean of values determined by H^{1-}NMR analysis and colourimetric TNBS assay, and the SEC analyses results. The chemical insertion of different alkyl amines has not altered the relative derivatization degree (DD_{Cx} mol mol^{-1}) significantly (about 11.0 mol%).

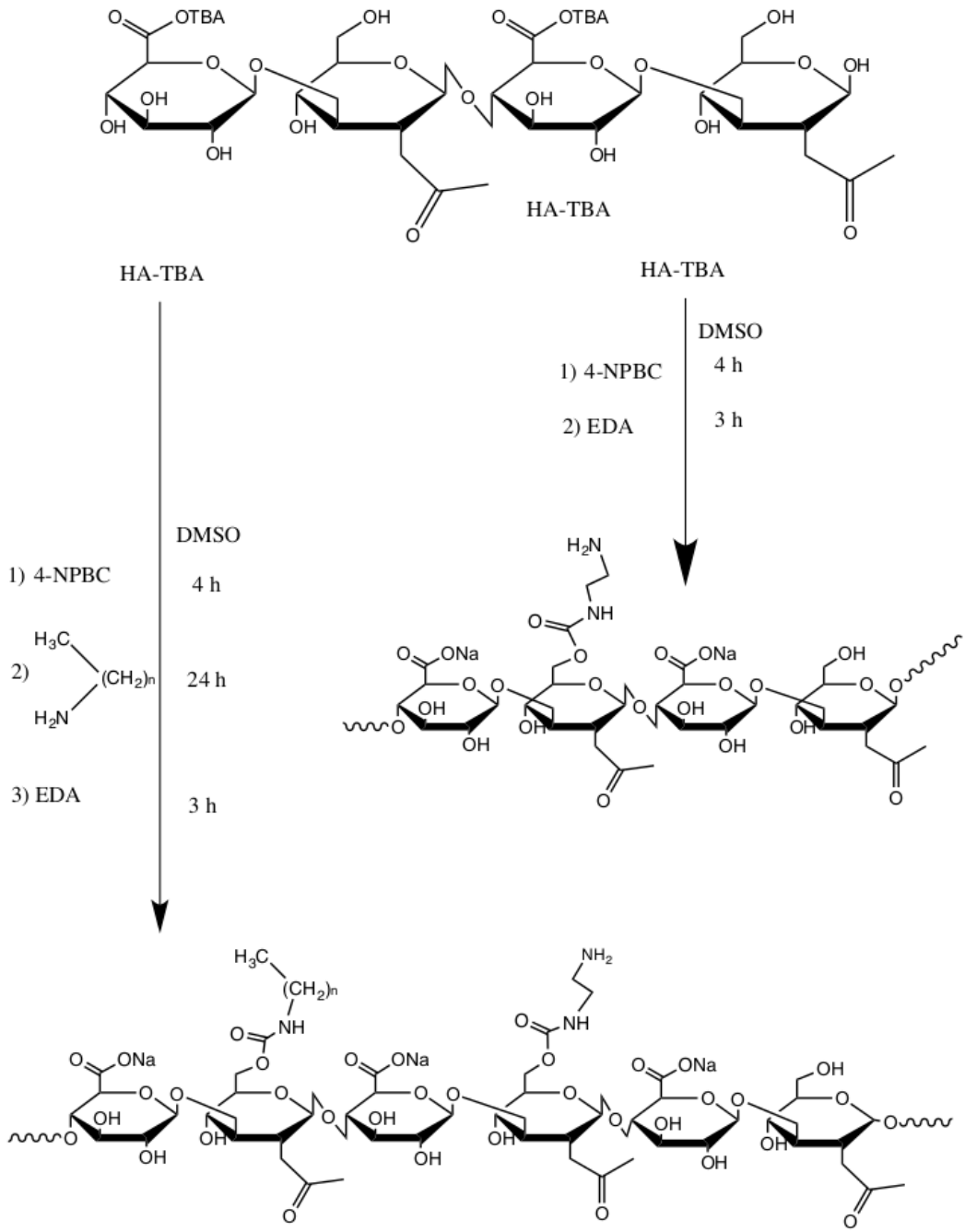

Scheme 8. Synthesis of hyaluronic acid derivatives

A statistically significant decrease in EDA functionalization has been observed by increasing chain length from C_8 to C_{18}, while no significant difference in alkyl functionalization has been noted. The reduced derivatization in EDA (DD_{EDA}) is in

agreement with the greater steric hindrance of the grafted alkyl amine. The derivatization with alkyl amine has been quantitative, but it has determined a progressive decrease in the final molecular weight of polymer according to a higher hydrophobic aggregation of these systems in aqueous environments, as determined by GPC analysis. These results were in agreement with other polysaccharide derivatives synthetized in similar conditions, like gellan gum alkyl-derivatives (Agnello, Gasperini, *et al.*, 2017).

Table 5. Derivatization degrees (DD), weight-average molecular weights (Mw) and polydispersity index (PDI) of HA-EDA, HA-EDA-C8, HA-EDA-C12, HA-EDA-C18. Data represented as mean ± standard deviation (SD)

Sample	DD_{EDA} mol%	DD_{Cx} mol%	M_w (kDa)	PDI
HA-EDA	70.0 ± 0.5	/	457	1.76
HA-EDA-C_8	40.0 ± 0.5	10.0 ± 0.5	416	1.98
HA-EDA-C_{12}	38.0 ± 0.5	12.0 ± 1.2	400	1.93
HA-EDA-C_{18}	30.0 ± 0.5	12.0 ± 1.3	322	1.83

ATR-IR spectra of derivatives showed a broad band centred at 3330 cm^{-1} (-OH and -NH asymmetrical vibrations), weak bands at 1715 cm^{-1} (stretching C=O), bands at 1642 and 1610 cm^{-1} (amide I of HA), 1151, 1081 and 1027 cm^{-1} (C-O alcohol and ether stretching).

3.3.2 Set-up of electrospinning procedure

The first goal was the reproducible production of nanofibrous scaffolds using only water as solvent. The use of water-soluble carrying polymers, like PEO or PVA, is a common strategy for HA or other polysaccharide electrospinning. Hydroxypropyl-β cyclodextrins (HPCD) are the third element which has been included whose effects in blends are helpful for many reasons. A considerable reduction of droplets and beads through the stabilization of Taylor's cone has been studied (Séon-Lutz *et al.*, 2019), as well as the potential control

of rheological behaviour of solutions (Agnello, Bongiovì, *et al.*, 2017). The presence of HPCD has represented an additional opportunity for the encapsulation of low water-soluble drugs during ES.

Preliminary electrospinning tests have been carried out to define solution parameters such as the concentration and the weight ratio HA*n*:PVA:HPCD. In a vertical electrospinning set-up, a low flow rate has been required to avoid dripping and to favor the evaporation of solvent from blends; thus the stability of Taylor's cone over several hours has been one of the main parameters considered.

The optimum of spinnable drug-free aqueous blends (H*n*) has been obtained by dispersion of HA-EDA, HA-EDA-C_8 or HA-EDA-C_{12} derivatives with PVA at 5% w/v respectively and with HPCD at 8.33% w/v in weight ratio HA*n*:PVA:HPCD equal to 1:1:1.66, while the optimum adopted for HA-EDA-C_{18} was 0.5:1:1.66. PVA has been set at 5% w/v and represented the lowest common amount which has determined the generation of nanofibers, probably because, below this value, PVA has been in a dilute condition to ensure enough entanglements (Rwei and Huang, 2012) Spinnable drug-loaded aqueous blends (HnX or H*n*X/2) have been obtained by incorporation of Dex at 0.166% w/w in H*0*, H*8*, H*12* blends and at 0.083 % w/w in H*18*. HPCD has acted effectively as a Taylor's cone stabilizer by slightly reducing the blend's conductivity and a thickening effect, determining a huge stabilization of the charged jet (Kayaci and Uyar, 2012). The inclusion of Dex at 0.166 % w/w in 1:1:1.66 blends and at 0.083 % w/w in 0.5:1:1.66 blend has not compromised the processing of the blends as showed in the comparison of SEM in Figure 34. Rotational rheological tests, reported in Figure 32, describe the decreasing viscosity curves with increasing shear rates, thus indicating the shear-thinning behaviour of blends.

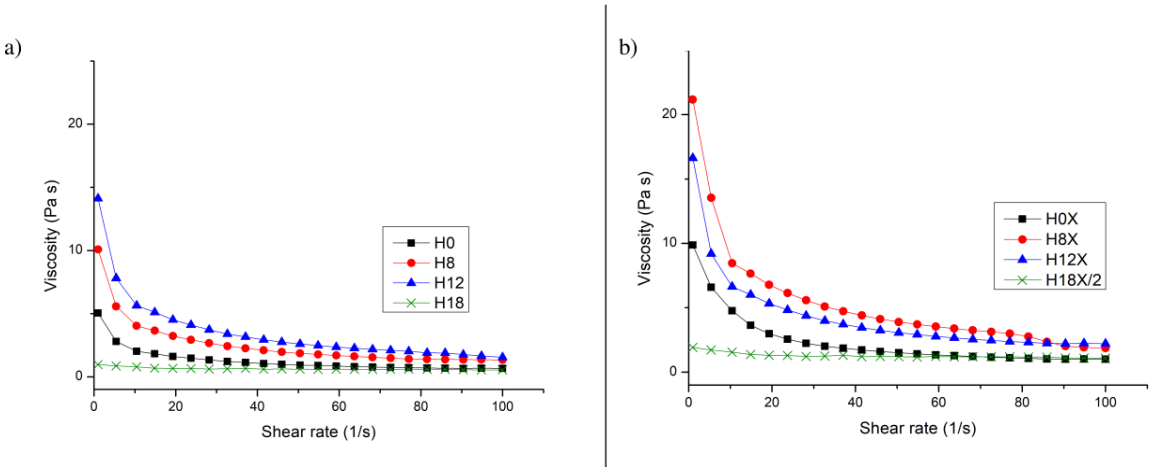

Figure 32. Viscosity curves showing the shear-thinning behaviour for a) spinnable drug-free dispersions and b) spinnable drug-loaded dispersion. Curves have been obtained using a rotational cone-plate measuring system

The comparison of H*0*, H*8*, H*12* blends has highlighted the increase in terms of viscosity at low-shear rates (1 sec^{-1}) according to the hydrophobic derivatization on HA backbone with different aliphatic amines (Figure 32 a), (H*0* = 5.0 ± 0.2 Pa•s, H*8* = 10.5 ± 0.2 Pa•s, H*12* =14.1 ± 0.4 Pa•s). The incorporation of Dex in blends, showed in Figure 32 b, further modified viscosity curves determining an increase (H*0*X = 9.8 ± 0.5 Pa•s, H*8*X = 21.2 ± 0.4 Pa•s, H*12*X =16.6 ± 0.6 Pa•s). The effect resulted more pronounced for the H*8*X blend, probably due to the stronger inclusion interactions of HPCD with the drug, which have determined the exclusion of C8 chain from the complex with the cyclodextrin.

H*18* blend (WR 0.5:1:1.66) has reported a low-shear viscosity of 0.9 ± 0.1 Pa•s which has raised up to 1.9 ± 0.2 Pa•s after the inclusion of Dex (H*18*X/2). As it possible to see from Figure 32, the behaviour of every blend has been mainly influenced by the hydrophobic character of the HA derivative and its concentration, as expected. In Table 6, the compositions and viscosities at 100 s^{-1} of drug-loaded blends (HnX and HnX/2) have been compared with respective drug-free ones, thus defining the spinnable viscosity range for these samples (0.5-2.2 Pa•s). The viscosity values at 100 s^{-1} have been considered relevant

to predict elongational properties of the blends during the stretching of the cone-shaped drop.

Table 6. Composition and viscosity at 100 s-1 of spinnable drug-free and drug loaded dispersions based on HA alkyl- derivatives

Sample Code	***HA derivative***	***Weight ratio HAn: PVA: HPCD***	***Dex amount (% w/w)***	***Viscosity (Pa•s)***
H*0*	HA-EDA	1:1:1.66	/	0.667
H*0*X	HA-EDA	1:1:1.66	0.166	1.009
H*0*X/2	HA-EDA	1:1:1.66	0.083	0.942
H*8*	HA-EDA-C_8	1:1:1.66	/	1.334
H*8*X	HA-EDA-C_8	1:1:1.66	0.166	1.850
H*12*	HA-EDA-C_{12}	1:1:1.66	/	1.543
H*12*X	HA-EDA-C_{12}	1:1:1.66	0.166	2.201
H*18*	HA-EDA-C_{18}	0.5:1:1.66	/	0.537
H*18*X/2	HA-EDA-C_{18}	0.5:1:1.66	0.083	1.075

Potential suitability for chemical crosslinking of matrices has been assayed and studied via frequency sweep characterization of corresponding hydrogels (Figure 33. Frequency sweep tests of drug-free blends (Hn) before and after EDC/NHS crosslinkingFigure 33). To achieve the main proposal of the scaffolds, the structural integrity of electrospun matrices needs to be extended by crosslinking, ensuring a stable mechanical barrier over weeks because HA*n*, PVA, and HPCD are all water-soluble compounds. Frequency sweep tests, reported in Figure 33, have suggested that the efficiency of crosslinking varied among spinnable drug-free blends. H*0* and H*18* blends resulted more susceptible to the process than other polymers, in fact, the G' and G" moduli increased about 1000 times. Referring to

a comb disposition of substituents onto polysaccharide backbones, the alkyl chains C_8 and C_{12} (H*8* and H*12* blends) have probably exerted a steric hindrance on hydrophilic moieties resulting in reduced susceptibility to the crosslinking and reduced strength of the hydrogels. In the case of HA-EDA-C_{18} blend (H*18*), the self-hydrophobic aggregation of long chains has led to the formation of compact hydrophobic cores which have probably exposed its hydrophilic moieties (i.e. free amino groups) to the environment, thus contributing to a very effective crosslinking.

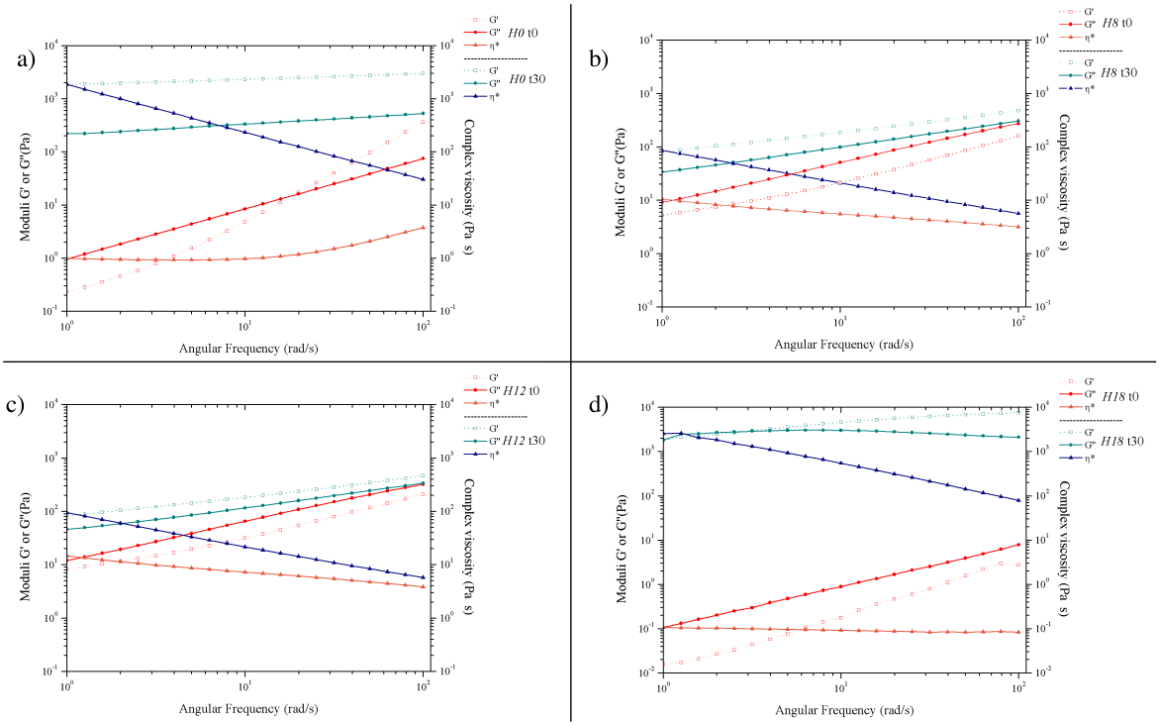

Figure 33. Frequency sweep tests of drug-free blends (Hn) before and after EDC/NHS crosslinking

All samples have showed an increased elastic response after thirty minutes (t30) than at zero time point (t0). Crosslinked hydrogels H*0* CL and H*18* CL (Figure 33 a-d) both have reported G' values (1-2 kPa in the range of frequency between 1-100 rad/s) higher than G' values (0.08- 0.14 kPa) of H*8* CL and H*12* CL (Figure 33 b-c). Rheological data performed on crosslinked blends have suggested the feasibility of post-production crosslinking

procedure exploiting the enhanced reactivity of pendant NH_2 groups of derivatives for an autocrosslinking procedure.

After characterization of blends, scaffolds have been produced using working conditions reported in Table 7, then dried, and peeled off after several days under hood.

Table 7. Optimized electrospinning working conditions

Sample	***Name***	***Flow rate (ml/h)***	***Distance (cm)***	***Voltage (kV)***	***Average size (nm)***	***DS***
HA-EDA 5% w/v + PVA 5% w/v +HPCD 8.33% w/v	H*0*	0.1	7.0	29.7	155.0	0.043
HA-EDA 5% w/v + PVA 5% w/v + HPCD 8.33% w/v + Dex 0.166% w/w	H*0*X	0.8	7.0	21.8	180.0	0.051
HA-EDA 5 w/v + PVA 5% w/v + HPCD 8.33% w/v +Dex 0.083 % w/w	H*0*X/2	0.8	7.0	21.8	190.0	0.062
HA-EDA-C_8 5% w/v + PVA 5% w/v + HPCD 8.33% w/v	H*8*	0.3	7.0	26.4	105.0	0.059
HA-EDA-C_8 5% w/v + PVA 5% w/v + HPCD 8.33% w/v + Dex 0.166% w/w	*H8X*	0.4	7.0	26.0	106.0	0.032
HA-EDA-C_{12} 5% w/v + PVA 5% w/v + HPCD 8.33% w/v	H*12*	0.3	7.0	26	100.0	0.034
HA-EDA-C_{12} 5% w/v + PVA 5% w/v + HPCD 8.33% w/v + Dex 0.166% w/w	*H12X*	0.4	7.0	26.0	98.0	0.029
HA-EDA-C_{18} 2.5% w/v + PVA 5% w/v + HPCD 8.33% w/v	*H18*	0.1	7.0	29.0	166.0	0.061
HA-EDA-C_{18} 2.5 w/v + PVA 5% w/v + HPCD 8.33% w/v +Dex 0.083 % w/w	*H18X/2*	0.4	8.0	24.6	146.0	0.032

SEM micrographs of drug-free mats (H*0*, H*8*, H*12*, and H*18*) and respective drug-loaded mats (H*0*X, H*8*X, H*12*X, and H*18*X/2) have been reported and supported by corresponding distribution curves of fibrillar diameter sizes in Figure 34.

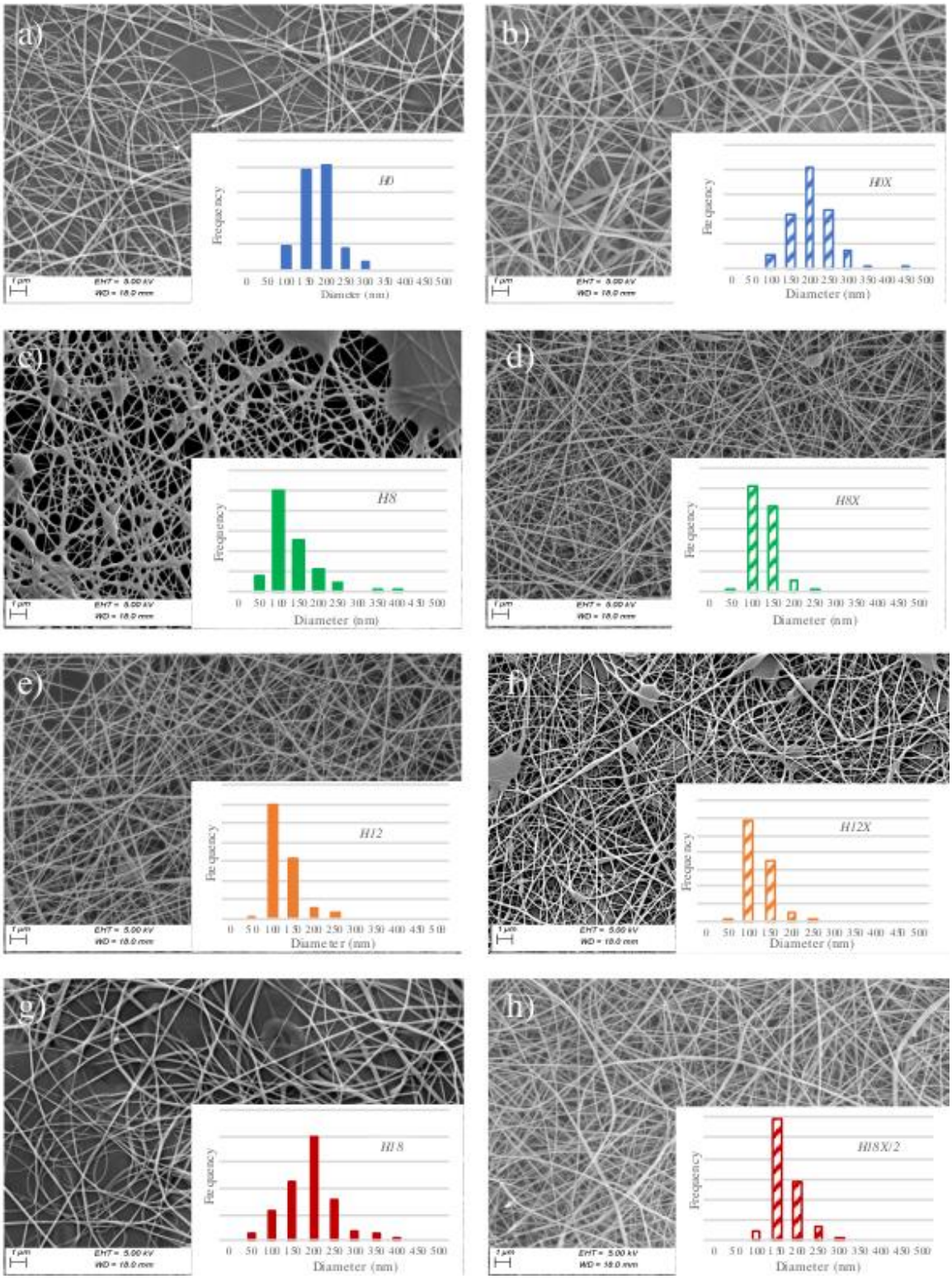

Figure 34. SEM micrographs and distribution curves of nanofibers: a) HA-EDA: PVA : HPCD 1:1:1.66 (H0); c) HA-EDA-C_8 :PVA:HPCD 1:1:1.66 (H8); e) HA-EDA-C_{12}:PVA:HPCD 1:1:1.66 (H12); g) HA-EDA-C_{18}:PVA: 0.5:1:1.66 (H18); and relative drug-loaded mats on the right side (HnX, HnX/2). Scale bar 1 µm. Data represented as mean ± standard deviation (SD)

During ES processing, no relevant differences have been noted between blends. Smooth, uniform and cylindrical nanofibers have been detected, and few defects observed only in

H*8* and H*12*X micrographs (Figure 34 c-f). Mean fiber diameters were less than 200 nm or slightly lower in almost all membrane produced. The incorporation of the drug (dexamethasone), the induced alteration of viscosities, and the optimization of the working conditions resulted into a narrowing of all distribution curves of diameters (Figure 34, right side) compared to drug-free blends. The efficiency of drug loading, reported in Table 8, has been around 87%, with no statistical difference among H*0*X, H*8*X, H*12*X, while the loading efficiency of H*18*X/2 mat has been the lowest one (83.2%).

The crosslinking of nanofibrous scaffolds occurred by soaking round-shaped samples in 500 µl of crosslinking bath (EtOH:H_2O 75:25 v/v) containing the exact amount of EDC/NHS which has satisfied the molar ratio (EDC/NHS/carboxyl groups of HA repetitive unit = 5: 2: 1). The crosslinking process did not alter the nanofibrillar morphology of membranes.

Untreated and crosslinked EM have been characterized analysing the effects exerted on different physical properties by HA*n* element. X-ray diffraction profiles of the singular powders have confirmed the non-crystalline structures of HA derivatives (data not reported), while a clear peak can be detected in the case of PVA as reported in the literature (Aziz *et al.*, 2017). All the XRD profiles of the mats have showed no sharp peaks but a broad curve, whose centre has reported a pronounced intensity attributable to PVA contribute (data not showed).

Water-contact angle (WCA) measurements, Figure 35, have showed the surface changes of every bare HA*n*-based nanofibrous matrix with drug-loaded ones before and after crosslinking.

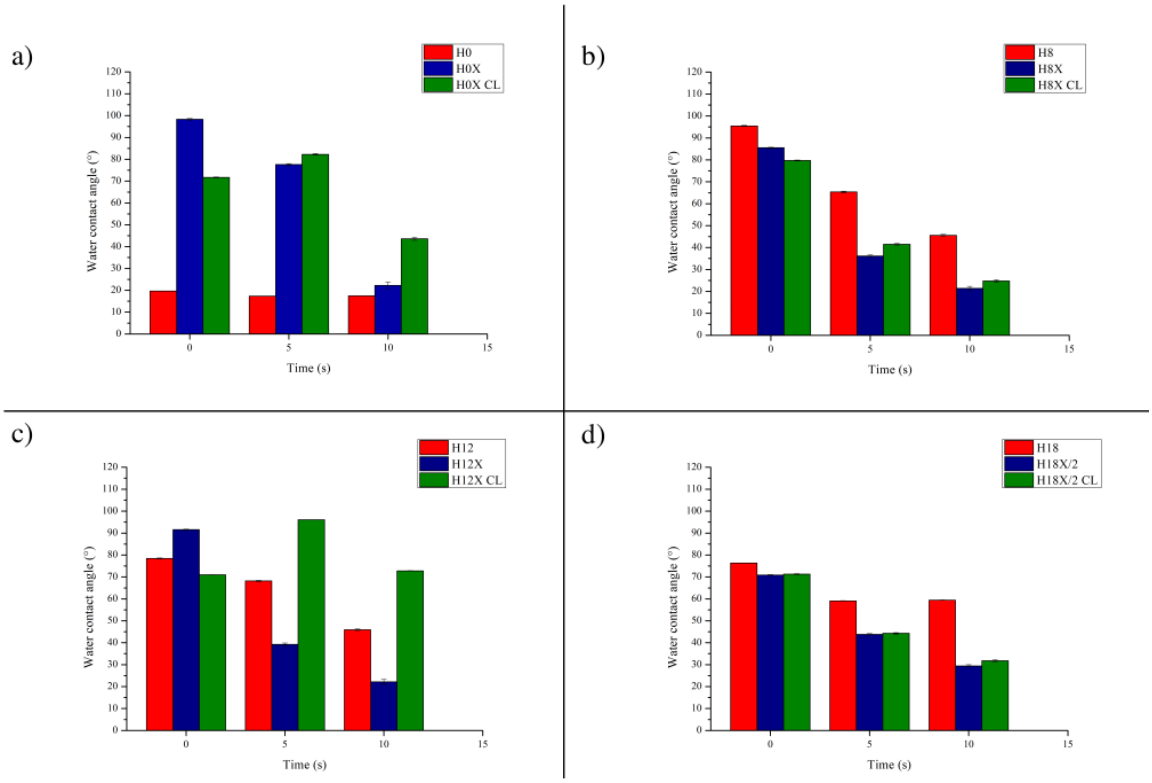

Figure 35. Water contact angles comparison of bare matrices, drug-loaded mats, and crosslinked drug-loaded mats based on each HA derivative. a) HA-EDA:PVA:HPCD 1:1:1.66 (H0, H0X, and H0X CL); b) HA-EDA-C_8:PVA:HPCD 1:1:1.66 (H8, H8X, and H8X CL); c) HA-EDA-C_{12}:PVA :HPCD 1:1:1.66 (H12, H12X, and H12X CL); d) HA-EDA-C_{18}:PVA: 0.5:1:1.66 (H18, H18X/2, and H18X/2 CL).Data represented as mean ± standard deviation (SD)

Water-contact angles of drug-free matrices after 10s, H*0*, H*8*, H*12*, H*18* (Figure 35), increased according to the rising hydrophobic character of the HA derivative (H*0* = 20°, H*8* = 45°, H*12* = 48°, H*18* = 60°). The hydrophobic derivatization of the polysaccharide has mainly defined the wettability of bare matrices. Figure 35 a, has showed the stable hydrophilic surface of the H*0* sample with a fixed contact angle of 20° for the detected time 0-10 sec. Dex-loaded sample (H*0*X) has displayed an initially increased contact angle up to 100°, which shifted to 20° at the end of the analysis. H*0*X CL showed angles in the range of 50-60°. H*8* and H*12* matrices, in Figure 35 b-c, displayed an initial hydrophobic surface (100° and 92°) that remodeled pver time (50° and 55°). The differences have vanished after dexamethasone's incorporation, causing a progressive rearrangement of these surfaces towards a hydrophilic angle after 10 seconds (≈20°). The event has been probably

determined from the entropy-driven self-assembling of polymeric aliphatic tails, which has generated more or less dense and stable hydrophobic cores as a function of the aliphatic graft length. After crosslinking, the WCA profiles of H*8*X CL reached 22° while the H*12*X CL sample resulted in the highest hydrophobic surface (78°) at the end of the analysis among the group. H*18* sample has displayed a constant contact angle around 60°, while both the incorporation of dexamethasone and the crosslinking reduced it to 30° (Figure 35 d).

3.3.3 Drug releasing and hydrolysis properties of matrices

Table 8 reports the values if drug loading and the incorporation efficiencies. Drug release profiles, hydrolysis and enzymatic resistance, have been highly dependent on both HA*n* derivative and post-electrospinning treatments.

Table 8. Drug loading and efficiency of electrospun matrices based on hyaluronan derivatives

Sample	***Name***	***Drug Loading (% w/w)***	***Efficiency %***
HA-EDA 5% w/v + PVA 5% w/v + HPCD 8.33% w/v + Dex 0.166% w/w	H*0*X	0.147 ± 0.002	88.35
HA-EDA-C_8 5% w/v + PVA 5% w/v + HPCD 8.33% w/v + Dex 0.166% w/w	H*8*X	0.146 ± 0.005	87.68
HA-EDA-C_{12} 5% w/v + PVA 5% w/v + HPCD 8.33% w/v + Dex 0.166% w/w	H*12*X	0.145 ± 0.003	87.57
HA-EDA-C_{18} 2.5 % w/v + PVA 5% w/v + HPCD 8.33% w/v +Dex 0.083% w/w	H*18*X/2	0.069 ± 0.001	83.23

The observed slight decrease in Dex loading efficiency could be related to the increasing hydrophobization of the polymer, from 88.35% of H0X membrane to 83.23% with H18X/2 membrane. Untreated and crosslinked membranes have been compared in 24-well plates in three aqueous media (PBS, Hyal 5 U ml^{-1}, and FBS 10% v/v) at 37°C for two months in terms of drug-releasing profile and uronic acid release (Figure 36 and Figure Figure 37).

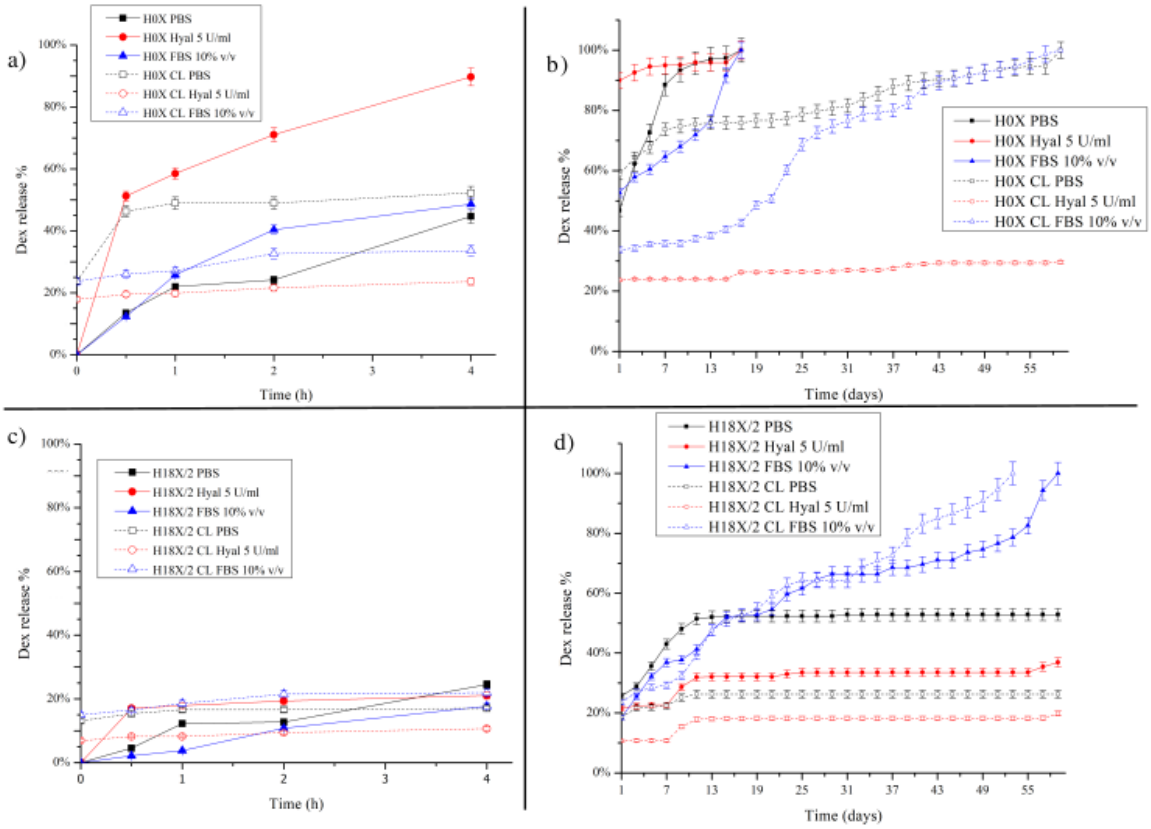

Figure 36. Release profile of Dex from untreated and crosslinked drug-loaded matrices in different aqueous media for two months. Data represented as mean ± standard deviation (SD)

All uncrosslinked scaffolds dissolved in aqueous media quickly, except for H*18*X/2. The advantages of the long-chain hydrophobic derivatization of HA can be resumed as a greater hydrolytic and enzymatic resistance, and the extension of Dex release curve in all aqueous media tested. The EDC/NHS method has exclusively improved the resistance of HA-EDA and HA-EDA-C_{18} based mats (H*0*X CL and H*18*X/2 CL) up to two months (Figure 36 b and d), without exerting any effect on H*8*X CL and H*12*X CL, which dissolved in less than

a day (data not reported). The drug loss, during the crosslinking, has been considered as the first point of every graph (t0) in Figure 36. H*0*X has released less than 50% of drug content after 4 hours in PBS and FBS 10% v/v, and a burst release up to 80% has been noted in the aqueous media with hyaluronidase during the first four hours (Figure 36 a). The release was completed in two weeks. The crosslinking (H*0*X CL) has determined two effects: an initial drug loss (17-23%); and a whole membrane stabilization. It has provided a sustained release of Dex up to two months in all aqueous media (Figure 36 b). The drug has been released from H8X and H12X samples after one day and the fast dissolution of membranes in all aqueous media occurred concurrently (data not reported). These mats have been discarded due to the incompatibility with the intended purpose for periodontal regeneration. Matrices based on HA-EDA-C_{18} released less than 20% after four hours (Figure 36 c). The total amount of drug has been entirely released after 55^{th} and 60^{th} day from untreated and crosslinked matrices (H*18*X/2 and H*18*X/2 CL) immersed in FBS 10% v/v, respectively (Figure 36 d).

Meanwhile, the amount released from H18X/2 samples in PBS and Hyal 5 U ml^{-1} has been around 60% and 40% after two months, respectively. The crosslinking has reduced both releases to 20%. The resuls were in agreement with frequency sweep analyses reported in Figure 33, where the reduced availability of EDA moieties in the H*8* and H*12* blends has generated weaker hydrogels than those resulting from the H*0* and H*18* blends.

In summary, the crosslinking provided two main advantages, such as the improvement of the stability of H*0*X in aqueous media which favoured a prolonged release of Dex for two months, and the adequate wettability of H*18*X/2 for cell cultures without altering its release profiles, as followed in FBS 10% v/v (Figure 36 d). Figure 37 shows the uronic acid percentage hydrolysed from each scaffold up to 60 days in the three aqueous media.

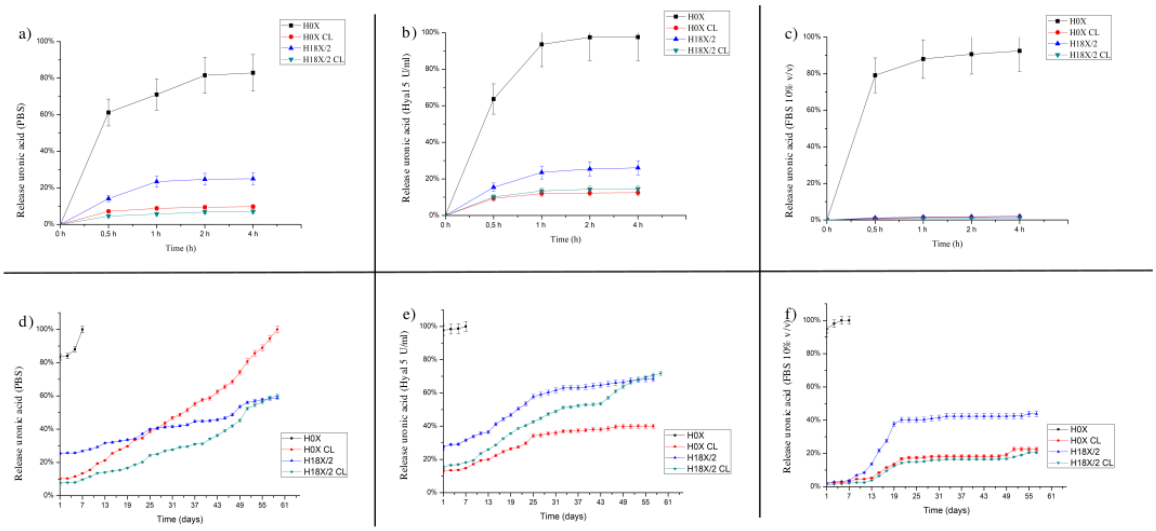

Figure 37. Quantification of uronic acid from untreated and crosslinked drug-loaded matrices treated for two months in different media (PBS, Hyal 5 U/ml and FBS 10% v/v). Data represented as mean ± standard deviation (SD)

A comparison of data reported in Figure 36 and Figure 37 could explain how hydrolysis influenced drug release. H*0*X has released around 80% of uronic acid in four hours (Figure 37 a-c), and it was completed after seven days (Figure 37 e-f) in all the aqueous media. The results agreed with its hydrolytic profile. H*18*X/2 has lost about 10% of its uronic acid content for up to four hours (Figure 37 a-c), while about 40% in FBS 10% v/v and 60% in PBS and Hyal 5 U/ml have been released after two months (Figure 37 e-f).

3.3.4 In vitro cell culture studies

To evaluate the osteoinductive effect of drug-loaded membranes, MC3T3 cells have been cultured for five weeks on selected mats, namely H*0*X CL, H*18*X/2, H*18*X/2 CL and respective drug-free controls performing proliferation assays and tests to evaluate the osteoinduction effect. A new sample has been introduced, H*0*X/2 CL, hence a crosslinked patch based on HA-EDA with the halved amount of Dex (0.083 wt%) and loading efficiency equal to 90.1%, as a comparable sample for *in vitro* performances of H*18*X/2 and H*18*X/2 CL. All the matrices proposed have been able to control the daily release of the drug

achieving a stable concentration around 10^{-8} M of Dex (Figure 36). MC3T3 cells have been seeded above mats and cultured in a proliferative medium up to 7 days. Proliferation occurred in all the samples, as reported in Figure 38.

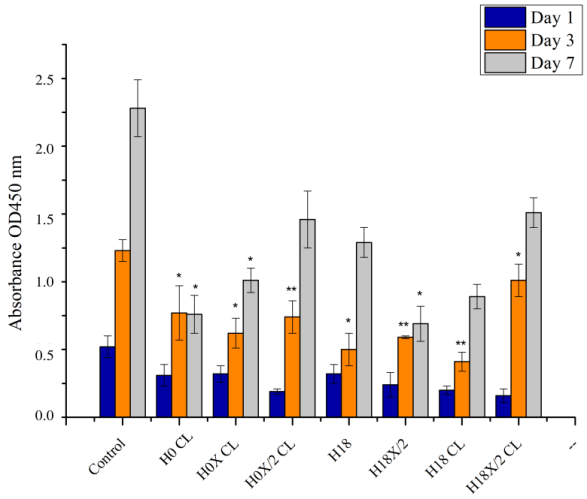

*Figure 38. Quantification of viable cell number in proliferation assay CCK-8 after 7 days of cell culturing. Statistical differences between scaffold and control were noted with * and ** to indicate p < 0.05 and p<0.01, respectively. Data are reported as mean ± standard deviation*

The DNA quantification has confirmed the absence of any cytotoxic effects from tested HA-EDA and HA-EDA-C_{18} membranes up to 28 days of culture and has been in accord with proliferation results (Figure 39).

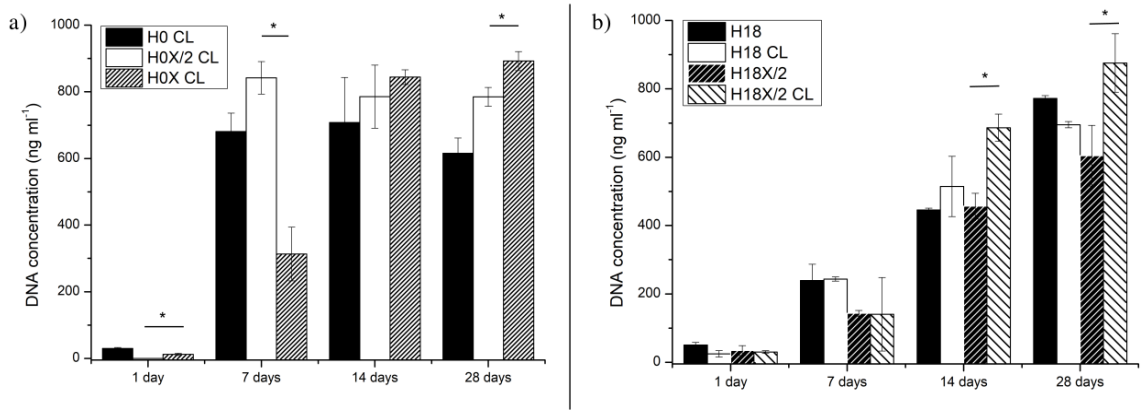

*Figure 39. Determination of DNA content from a) HA-EDA based systems; b) HA-EDA-C18 based systems until 28 days of cell culture in Dex-free osteogenic medium. Data represented as mean ± standard deviation (SD). Statistical differences between two drug loaded sampe were noted with * and placed above "“—“ p< 0.05*

Figure 40 shows alkaline phosphatase (ALP) activities up to the 28th day from *in vitro* culture experiments. ALP assay and calcium content assay have coherently reflected the amount of drug in each sample, showing that the bioactivity of Dex has been well persevered using the HA derivatives and the electrospinning technique. The results of these assays have been considered as typical distinctive markers to value the rate of osteogenic induction exerted on MC3T3 cells.

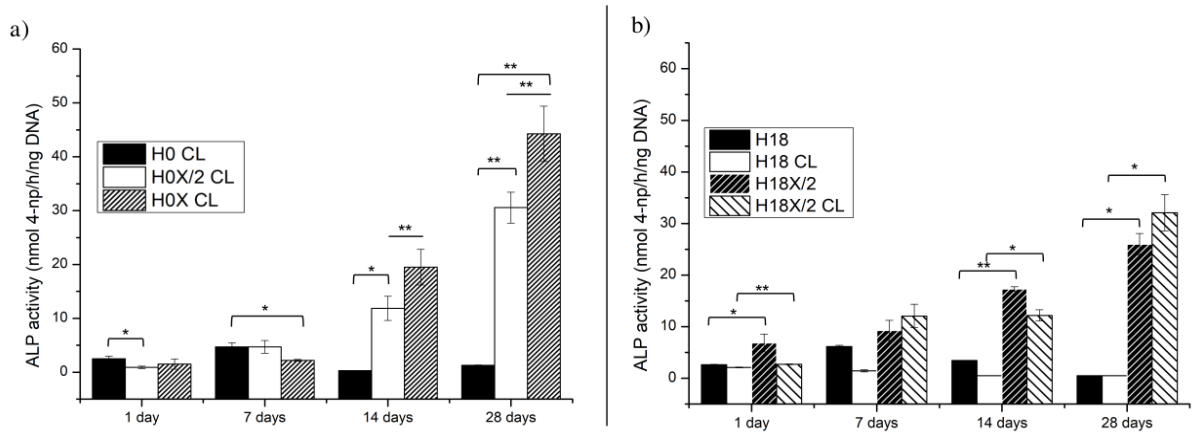

*Figure 40. Evaluation of alkaline phosphatase (ALP) activity from a) HA-EDA based systems; b) HA-EDA-C18 based systems until 28 days of cell culture in Dex-free osteogenic medium. Data represented as mean ± standard deviation (SD). Statistically significant differences between drug-free and drug-loaded samples were noted with * or ** to indicate p < 0.05 and p<0.01 and placed above"[", or above "—" to indicate the difference between two drug-loaded samples*

In Figure 40a, an increase of ALP activity has been noted for H*0*X/2 CL at day 14 ($p < 0.05$) and for H*0*X/2 CL and H*0*X CL at day 28 concering drug-free sample ($p < 0.01$). In particulare, the H*0*X CL sample provided the highest activity value (≈ 45 mmol 4-NP/h/ng DNA). Notably, higher values of ALP activity (Figure 40 b) have been also noted for H*18*X/2 and H*18*X/2 CL compared to drug-free matrices at 14th and 28th days ($p<0.05$). Figure 41 shows the induced mineralization capability as result of cell culturing above membranes for 35 days.

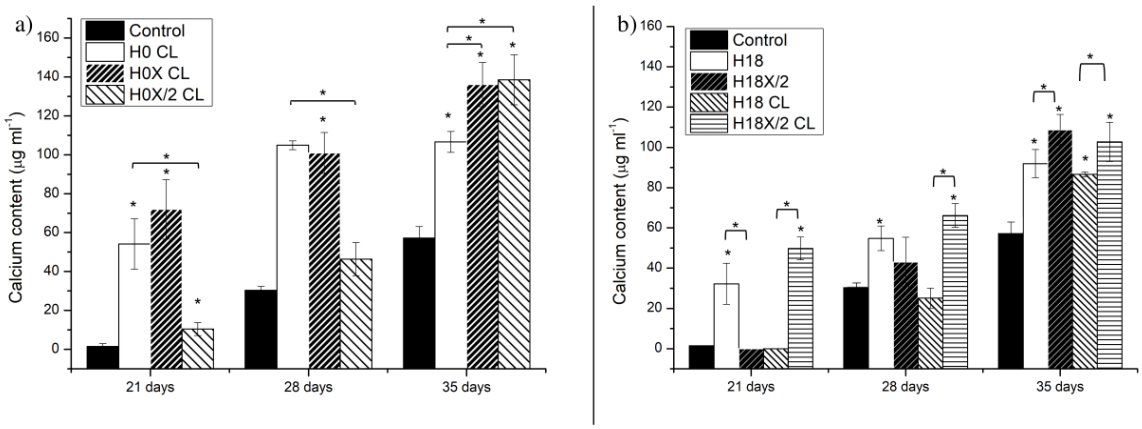

*Figure 41. Determination of calcium content from a) HA-EDA based matrices and b) HA-EDA-C18 based scaffold after 35 days of cell culturing. Data represented as mean ± standard deviation (SD). Statistical differences between scaffold and control were noted with * to indicate p < 0.05 Statistical differences between drug free and drug loaded scaffolds were noted with * to indicate p < 0.05 and placed above "["*

The control (black bars), represented by the H*0* CL immersed in a complete osteogenic medium without cells, has showed a certain absorption of calcium during time. Bigger calcium deposits (140-100 µg ml^{-1}) have been found in all drug-loaded samples than control on 35th day ($p<0.05$). Calcium deposits have also been found in H*0* CL, H*0*X CL, H*18*, and H*18* CL (about 90 µg ml^{-1}). All drug-loaded matrices have showed higher values than the respective drug-free sample on 35th day ($p<0.05$). In particular, the H*0*X/2 CL membrane has reported the highest value (140 µg ml^{-1}) in Figure 41 a. The mineralization assay has also indicated a self-mineralizing effect of the membranes themselves since the higher values of calcium have been found for Dex-free matrices than controls ($p<0.05$).

3.4 Evaluation of therapeutic properties of the electrospun membrane of HA-EDA and graphene oxide

The variability of the etiology of an infection reduces the efficacy of some antibiotic therapies. Antibiotic resistance is related to some gene mutations of planktonic bacteria and with the formation of bacterial biofilms. Biofilms are sessile multicellular communities comprised of microrganisms, embedded in a self-produced extracellular matrix mainly composed of polysaccharides and proteins, able to confer increased resistence to external stresses and protection to bacteria, impeding the infiltration of antibiotics and the action of immune host cells (Costerton, Stewart and Greenberg, 1999; Wang *et al.*, 2020). Great interest in the formulation of biodevices with *on demand* non-specific antimicrobial effects growed during last years (Nguyen *et al.*, 2015; Mauro *et al.*, 2020).

Nanocarbon materials can absorb light from the UV to near-infrared (NIR) region and convert the absorbed light into heat through nonradiactive decay. Hyperthermia has been shown to be effective for the eradication of bacteria and their biofilms (Xiao *et al.*, 2017). The theraphy, induced by NIR light, has demonstrated to exert a deep tissue penetration and no significant absorption from tissues. One of the main limitation of this application is the nonselective thermal effect during the irradiation which could damage the neighbouring structures of the body. Once activated from an external stimuli, the thermogenic effect has demonstrated to inhibit bacterial proliferation, to destabilize biofilm structures and to increase the effect of common antibiotics.

In light of results achieved with hyaluronan derivatives, the fabrication of improved electrospun membranes combined with nanocarbon materials allowed to extend the application of these membranes for wound healing purposes as illustrated in Scheme 9. With the aim of faster regeneration of dermal and epidermal lesions, graphene oxide was introduced into HA-based nanofibrillar membrane to exert an antimicrobial effect by acting

in collaboration with ciprofloxacin. Fibroblasts have been cultured above membranes evaluating the proliferative capability of the systems proposed.

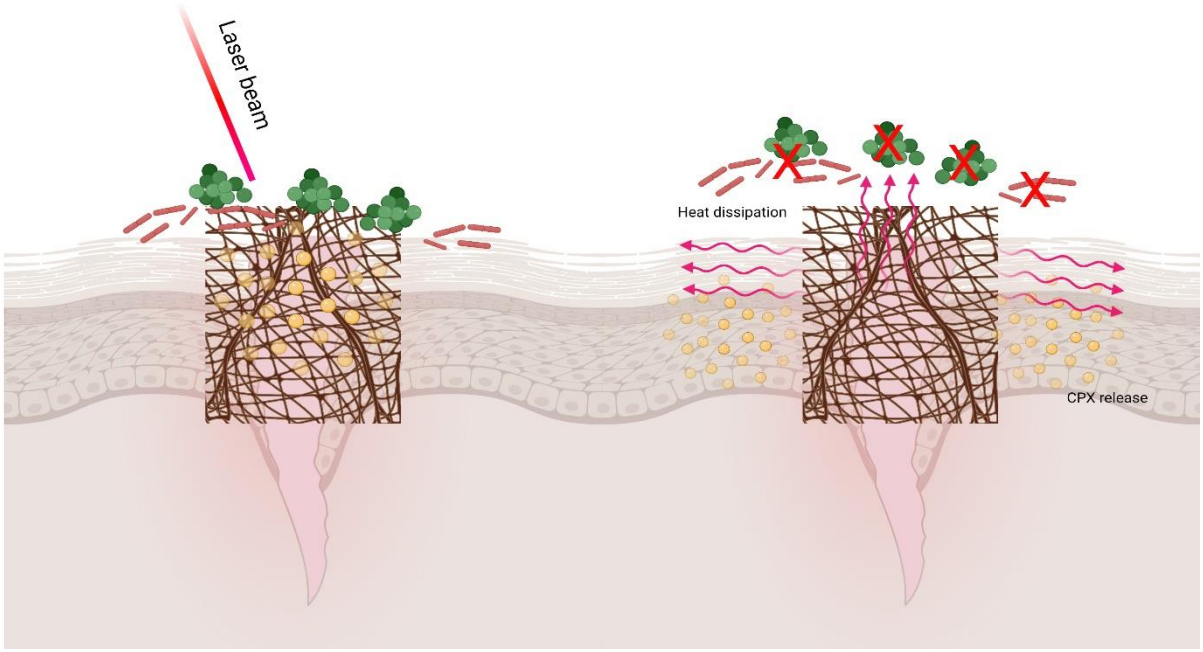

Scheme 9. Representation of antibacterial application of HA-EDA based membranes with graphene oxide for chronic wound healing application

3.4.1 Preparation procedure and rheological characterization of HA-EDA blend with graphene oxide

Considering the expertise acquired with the polymer HA-EDA and the composition of the blends used previously, the blends for this investigation have prepared similarly. The rheological characterization regarded only spinnable blends, i.e. such blends, which have demonstrated the ability to generate Taylor's cone and to depose a solid on the collector.

The addition of GO to the HA blends, (0.02% w/v) HAGOa and (0.03% w/v) HAGOb, has caused a visible decrease in terms of viscosity, as evaluated by the inversion tube test. This evidence has been confirmed by flow ramp studies (Figure 42), where a progressive reduction in viscosity has been related to an increase of GO amount in the blend.

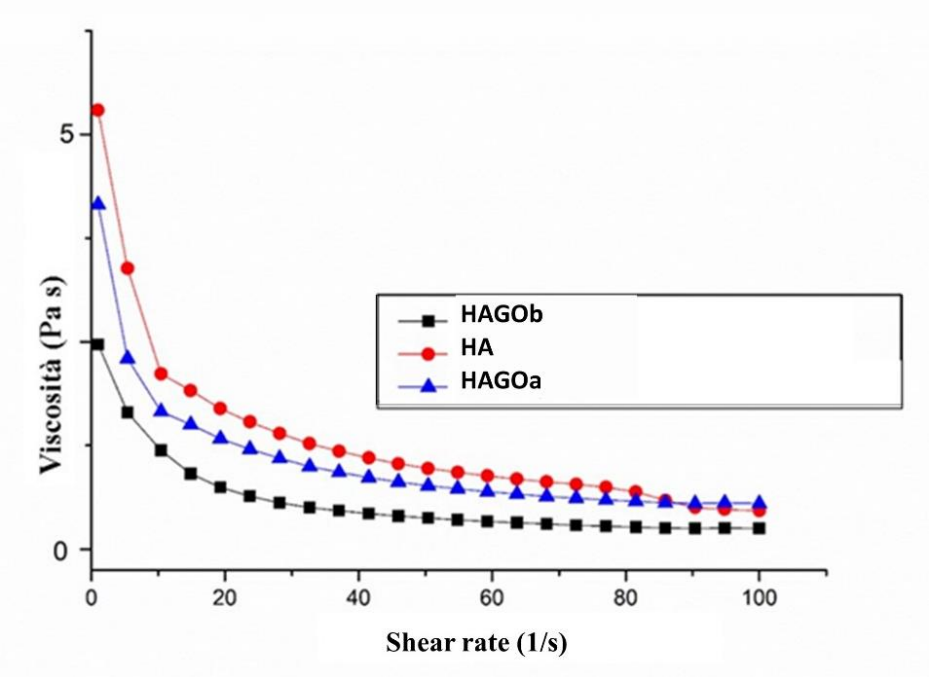

Figure 42. Flow ramp comparison of blends based on HA and HA with two concentration of GO (HAGOa and HAGOb) before electrospinning

It is reasonable to hypothesize that GO has reduced interactions between HA polymeric chains, determining a lower opposition to the flow, as similarly reported in the literature (Moraes *et al.*, 2020). Tested blends have reported a shear-thinning behaviour representing the ability of polymeric chains to align according to the direction of the applied shear. As the shear rate increased, the viscosity gradually decreased throughout the blend. The results shown in Figure 42 could represent what happens to the mixture once it has been processed by electrospinning, in fact, considering the low shear rates which are similar to those imposed by the syringe piston, the rheological behavior has favoured the flow of the blend. On the other hand, the application of the electric field indefinitely stretched the drop of the solution and it can be compared to the high shear rate results obtained by the rheometer.

In frequency sweep tests, HA, HAGOa, and HAGOb showed a typical viscoelastic behaviour (Figure 43). In these cases, G" values resulted higher than G' for low angular frequencies (comparable to low feed rate stress exerted by syringe pump) showing the ability of the three blends to flow.

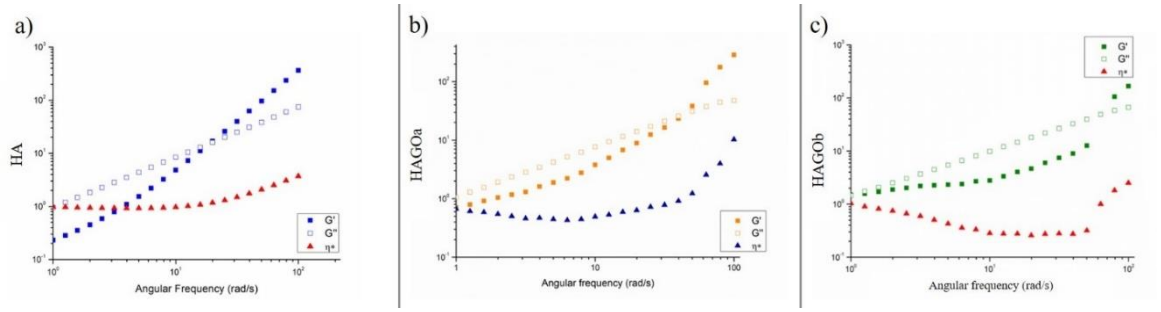

Figure 43. Frequency sweep test of pre-electrospinning dispersions. a) HA blend, b) HAGOa blend, c) HAGOb blend

A crossover point can be detected in all rheograms, after which G" is greater than G' and the systems have reported elastic responses causing gelation. The more graphene oxide is included in the mixture, the more the crossover point shifts to higher frequencies.

This result could be attributed to the interposing effect of GO between polymeric chains, which delayed gelation. From the frequency sweep tests, it could be also highlighted a reduction in the damping factor ($\tan\delta = G''/G'$) of GO-loaded blends at low frequencies. During the electrospinning process, the reduction of the damping factors resulted in greater efforts to regulate the flow rate and the applied electric field due to a greater propensity for gelation on the nozzle(Shenoy *et al.*, 2005).

3.4.2 Fabrication procedure of electrospun membranes based on HA-EDA and GO

The membranes have been prepared following the parameters reported in Table 9. The conditions have permitted the generation of fibrillar scaffolds from HA and HAGOb blends, while several beads have been collected for HAGOa tests. Variations in distance, electric field or feed rate resulted in non-continuous spinning where the gelation of the spinning drop was the main cause.

Table 9. Optimized ES parameters for HA-based blends

Sample	**Distance nozzle-collector**	**Electric Field**	**Feed rate**
HA	10 cm	30kV	0.3 ml/h
HAGOa	10 cm	30kV	0.3 ml/h
HAGOb	10 cm	30kV	0.3 ml/h

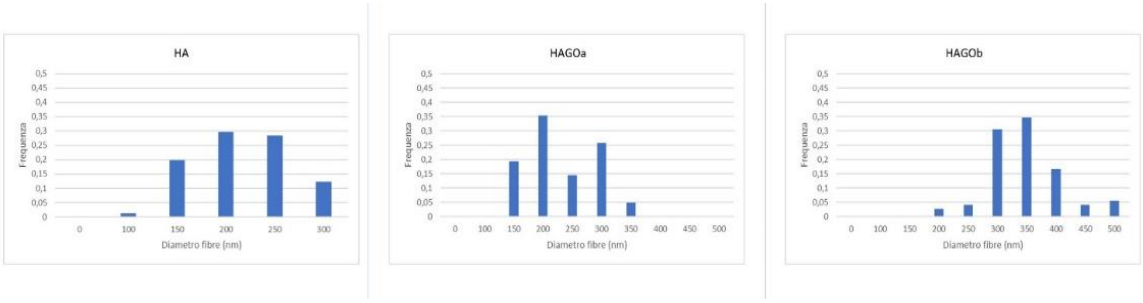

Figure 44 compares the SEM micrographs obtained with reported conditions and the frequency of diameter size distribution for every SEM picture. The images derived from HA and HAGOb blends showed high fibrillarity (

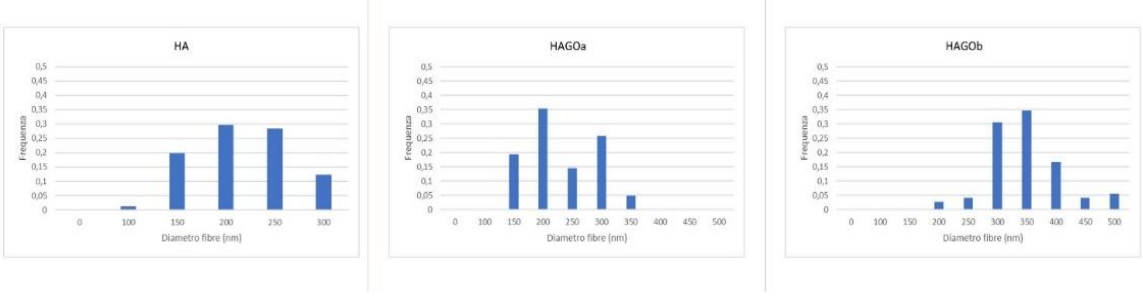

Figure 44a and c), whereas the HAGOa showed some beads on the scaffold.

The average diameters obtained have been calculated and equal to 250 ± 57 nm for HA blend, 206 ± 61 nm for HAGOa, and 301 ± 66 nm for HAGOb. The results suggested to perform further characterizations on the HAGOb sample.

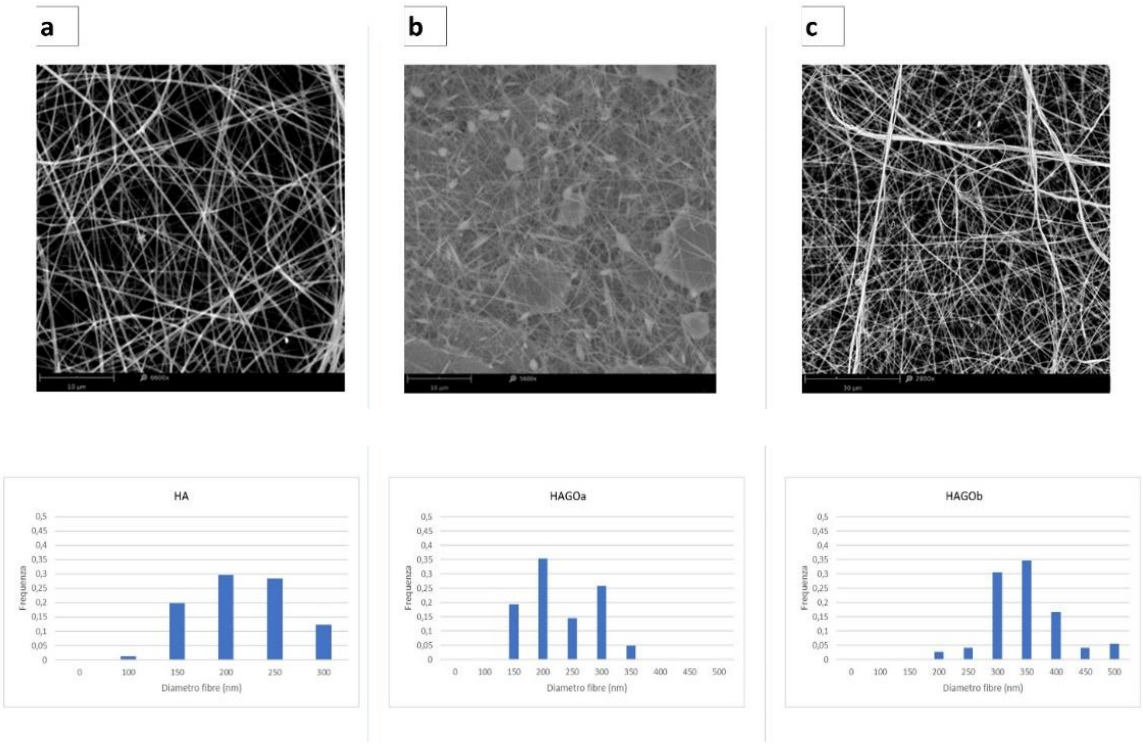

Figure 44. SEM images of electrospun scaffolds based on HA blend(a); HAGOa (b); and HAGOb (c). Scale bar 30 µm. The dimensional distribution of each membrane has been reported below the corresponding image.

3.4.3 Hydrolysis and enzymatic resistance of crosslinked membranes

All membranes were found to be highly dispersible in water; therefore a post-electrospun crosslinking procedure occurred via EDC/NHS coupling to increase the resistance of the membranes in contact with biological fluids as well as their mechanical properties.

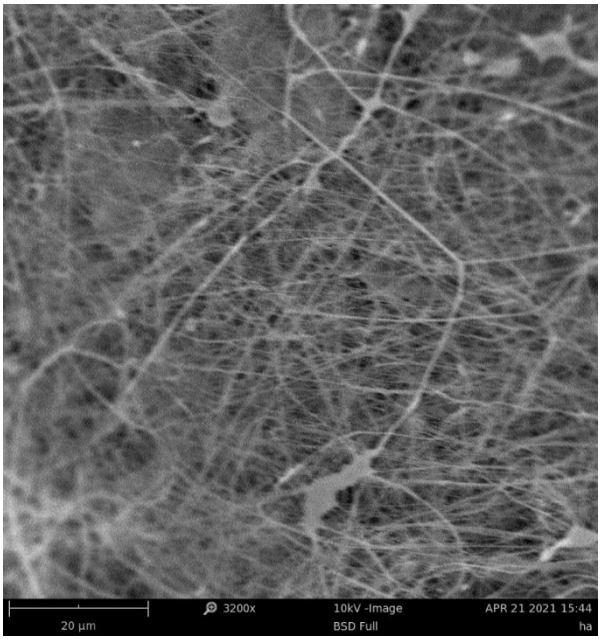

Figure 45. SEM micrograph of crosslinked HAGOb after crosslinking in EDC/NHS solution EtOH: H_2O 75:25 v/v

Considering wound dressing systems should absorb exudates from the wound, *in vitro* swelling studies and hydrolytic and enzymatic degradation have been investigated on crosslinked (CL) membranes obtaining HA CL and HAGOb CL.

Table 10 shows the weight ratio (Q value) of swollen/dry weight of membranes after 24 hours of incubation in DPBS. The sample HA CL doubled its weight, while the sample HAGOb CL showed a three times higher weight. The greater swelling capacity could be related to the higher hydrophilicity due to graphene oxide, or to the interposition of GO between HA chains which resulted in a less dense structure capable of absorbing a greater amount of aqueous medium.

Table 10. Swelling degree studies reported as Q value after 24 hours of incubation in DPBS pH 7.4 at 37°C

Scaffold	**Q values after 24 hours**
HA CL	1.85 ± 0.11
HAGOb CL	3.54± 0.18

Components of a wound dressing device should be biodegradable to aid removal from the wound bed. The need to remove common bandages could result in the loss of neotissue, further delaying the healing. Moreover, the degradation of the scaffold should occur in an appropriate timeframe with the healing process. The hydrolytic profiles of crosslinked and untreated membranes are reported in Figure 46. As reported in Figure 46a, the membranes were found to be highly dispersible in water and dissolve repidly in the medium in 24 hours ($p < 0.05$), considering the high solubility of the components in the aqueous phase.

In this case, the presence of GO determines a slight increase in water resistance (80% after one day). Results reported in Figure 46b, expressed as percentage of uronic acid release, shows the improvement of the hydrolytic resistance of crosslinked membranes when immersed in DPBS pH 7.4 up to 45 days ($p < 0.05$). The hydrolytic profile of the sample HAGOb CL shows a 80% of degradation after fifteen days, whereas only the 40% degrades from HA CL sample.

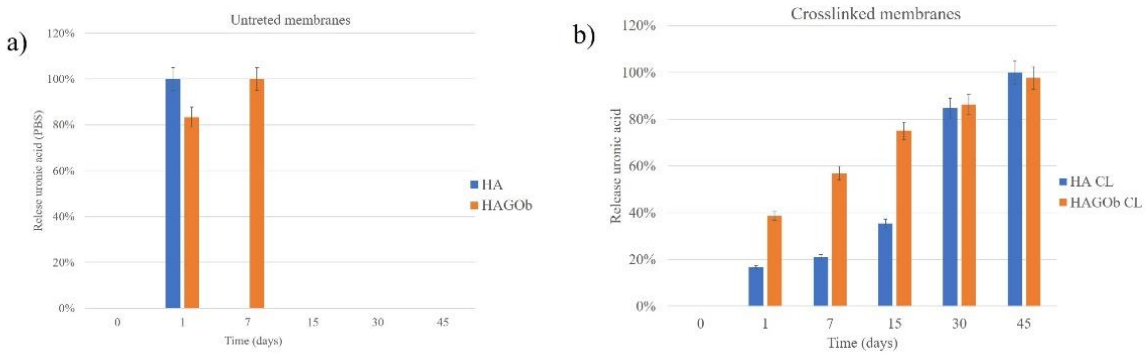

Figure 46. Hydrolytical studies of electrospun membranes HA and HAGOb via carbazole assay. a) untreated membranes; b) membranes crosslinked through EDC/NHS coupling. Results are reported as mean value ± standard deviation

The reported results are in agreement with the swelling data showing the greater ability of HAGOb CL to incorporate an aqueous medium; thus causing a more rapid hydrolysis. However, considering that most wound dressing devices need to be replaced every three days, the water resistance of HAGOb CL allows the support to be retained for an extended period of time, avoiding the need for removal and the risk of causing further damage. The rate of degradation should be adjusted according to the period of deposition and remodeling of the neo-tissue, as an essential feature of resorbable devices (Kim *et al.*, 2018).

3.4.4 Evalutation of hyperthermal features and drug-eluting profiles

The ability of HA-based electrospun membranes to exert a thermogenic effect has been evalued as the increased values of the temperature where scaffold are immersed after exposure to NIR light (810 nm).

Figure 47 reports the measured temperatures of aqueous medium (DPBS) after continuous laser irradiation of crosslinked membranes for 25, 50, 75, 100, and 125 seconds. The irradiation of the membrane without graphene oxide (HA CL, green line) did not show any thermogenic effect reporting the starting ambient temperature (25°C) because this sample is not able to convert light into heat.

The hyperthermal capacity is esclusively related to the presence of graphene oxide (GO); in fact, once applied the stimulus for 25 seconds, the temperature increased (around 32 °C) for GO-bearing samples. Exposing scaffolds to 5 W light, orange line, the temperature of medium has increased according to the time of exposure reaching the highest value (36°C) after 125 seconds. The application of NIR light at 10 W, blue line, determines an almost linear relationship between the increase in the temperature of the medium and the exposure time; then the medium was heated to 47°C as a maximum value after 125 seconds. The exact temperature of the scaffolds after exposure to NIR light was not measured directly but it was higher than the medium temperature. As similarly reported in the literature, scaffolds are sensitive to both power and the time of irradiation (Fiorica *et al.*, 2017).

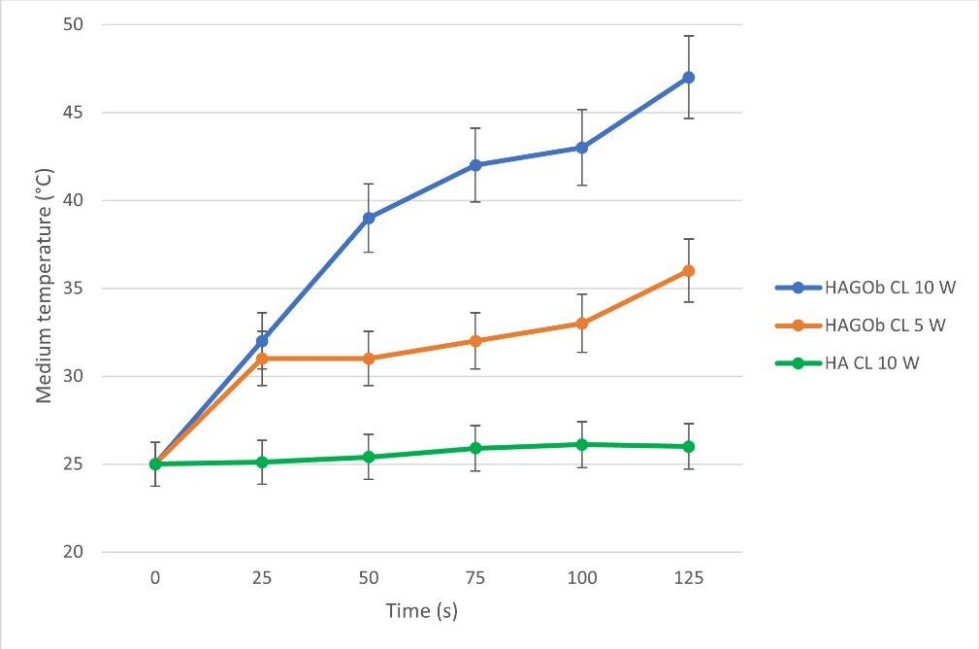

Figure 47. Hypertermal effect of electrospun membranes based on HA-EDA derivative in presence of graphene oxide (GO) after laser irradiation (808 nm) using 10 W (blue line) or 5 W (orange line). Data are reported as mean value ± standard deviation

The exposure to NIR light has changed the macroscopic morphology of the scaffold determining a shrinking of membrane surface.

Ciprofloxacin (CPX) has been loaded on electrospun membrane and drug-eluting features were evaluated. Spray-dried ciprofloxacin microparticles have been used to dissolve the drug in the aqueous blend before electrospinning procedure with a drug loading of 5% (mg of drug/ mg of HA+PVA). The incorporation of drug did not change the instrumental settings adopted for previous fabrications.

As reported in Figure 48, the drug did not significantly affect the morphology of the scaffold. The avarage diameter size of fibers result 222 nm ± 60 nm. After crosslinking of the membranes, the drug loading has resulted equal to be 3.61 ± 0.02 %

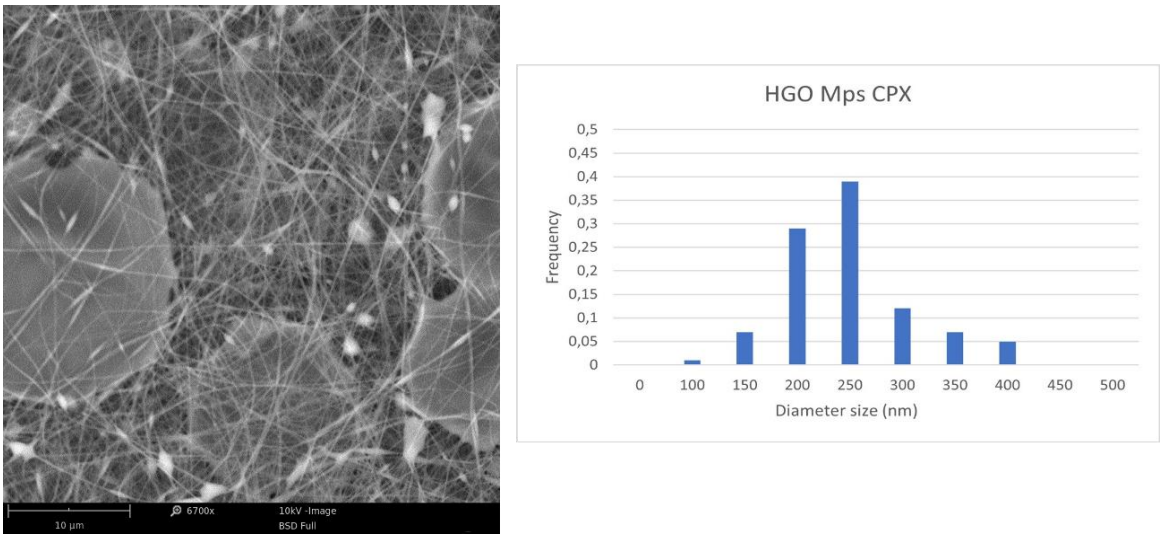

Figure 48.SEM micrograph of CPX-loaded electrospun membrane with HA and graphene oxide (GO) and fiber size distribution as calcuted from ImageJ software

Drug release studies were performed by immersing round-shaped crosslinked membranes of similar weight (10 mg bearing 361 µg of CPX) in DPBS at 37°C. In the first instance, the membranes have retained most of the drug (approximately 97%) after a week of immersion (data not shown). The drug retention is probably due to π–π stacking interaction between GO and aromatic moieties of the drug. At predetermined times, drug-loaded membranes have been light-triggered and cumulative release was reported in Figure 49. The

influence of NIR light exposure on drug-eluting features of scaffolds has been valued after daily applications of laser at two different powers.

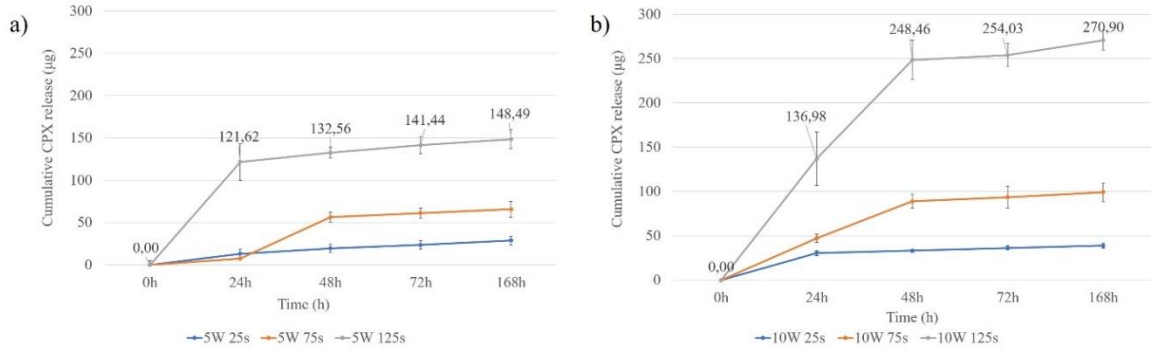

Figure 49. CPX release profile from HAGOb CL membrane after daily NIR light continuous exposure for 25, 75, and 125 seconds with laser using a) 5 W; or b) 10 W. Data are reported as mean value ± standard deviation

In Figure 49a, the stimulation at 5W for 25 seconds (blue line) results in a little drug release in the medium after the first 24 hours (approximately 3%). After seven days, the cumulative release reaches the 8% of the total drug loaded. A similar trend occurs for the first 24 hours fof the sample treated for 75 seconds at 5 W (approximately 2%), but the second application has determined the release of about 65 µg of CPX (18% of drug loaded). Interesting results occured after 125 seconds of light exposure, where a burst effect was noted (about 120 µg, approximately 34%). In this case, the subsequent stimulations did not result in any additional effect (approximately 42 of the total drug loaded). The membrane seems to be no more sensible to other stimulations.

In summary, the application of 5 W laser resulted in a consistent effect only after 24 hours and for 125 seconds of exposure. Figure 49b reports the drug release profile from membranes treated with a laser power of 10 W. After 24 hours, matrices have released 30 µg, 47 µg, and 137 µg (approximately 8%, 13%, and 38%) when exposed for 25, 75, and 125 seconds, respectively. The drug loss from the membrane increased based on the time of exposure to laser light confirming previous results with lower power light. Further

exposures of 25 seconds (blue line, Figure 49b) did not determined significative releases of the drug, while exposures of 75 second at 10W (orange line, Figure 49b) increased the release around 25% of the whole amount of drug loaded in the membrane. The second exposure of 125 seconds (gray line, Figure 49b) determined the release of additional 112 μg (approximately 69%). After seven days, the other daily exposure for 125 seconds caused no significant drug release in the medium.

In summary, the membranes were found to be directly sensitive both to the time of exposure to light and to the power of the laser used up to the second exposure. After the other stimulations, all membranes did not release significant amounts of the drug for up to seven days.

3.4.5 In vitro cytocompatibility studies

The adhesion of fibroblast cells has been evaluated through live and dead assay after 1 and 3 days of culture of cells above crosslinked membranes. Images have been recorded with fluorescent miscroscope and reported in Figure 50.

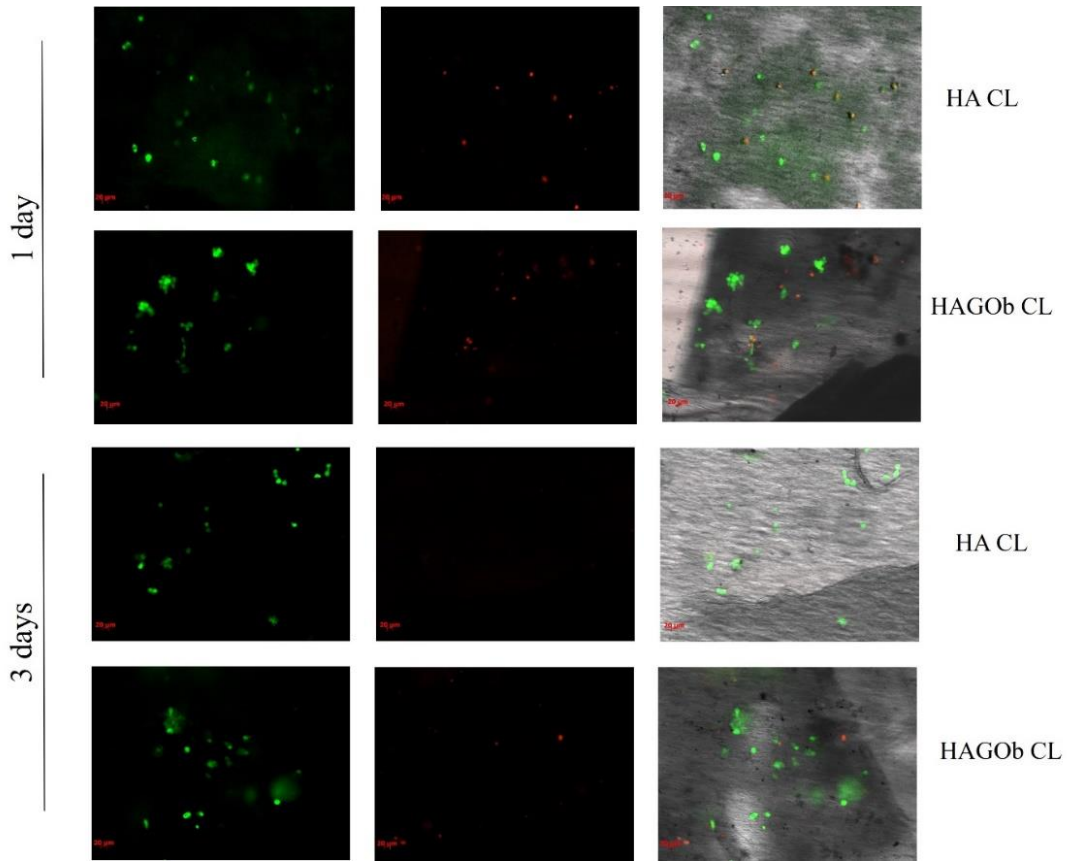

Figure 50. Live and Dead assay of fibroblasts seeded above HA-based membranes after 1 and 3 days of cell culture. Viable cell (green) and dead cells (red) are visible. Scale bar 20 µm

The fibroblasts appeared almost all viable (green) when seeded over the membranes, and only a few dead cells (red) were observed one day after seed in both the seeding both in HA CL and HAGOb CL samples. No significant differences were found.

Cell proliferation has been quantified with MTS assay and reported in Figure 51. The assay has compared HA CL, HAGOb CL and HAGOb CL +CPX membranes and all samples have showed almost similar values close to cells cultured on tissue culture plate (TCP) used as control. The HAGOb CL sample has showed the highest value after three days of cell culture.

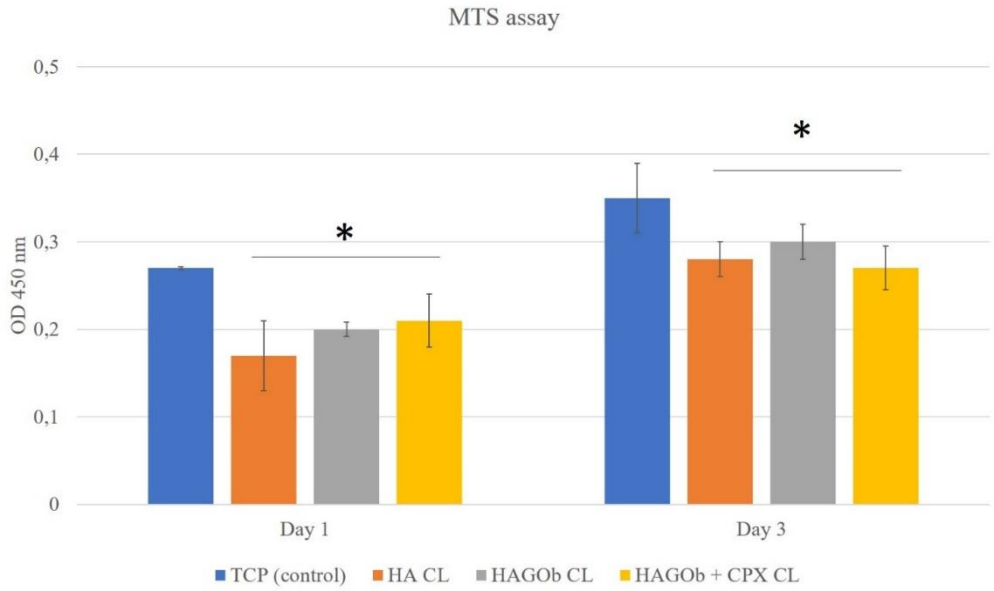

Figure 51. Cell proliferation assay by MTS method on electrospun membranes after 1 and 3 days of cell culture. Data reported as mean value ± standard deviation. Statistical significance ($p < 0.02$) versus control at the same time point

3.4.6 Antimicrobial properties

Considering the drug-loss from membranes resulted more higher the MIC for both *S.aureus* and *P.*aeruginosa, CPX-membrane with a loading of 1.8 % w/w was prepared to better highlight the synergistic drug-eluting and thermogenic features.

The investigation of the long-term antibacterial properties of HA-based electrospun membranes under NIR light irradiation, the inhibition zones of drug-free and CPX-loaded membranes were evaluated against *S. aureus* and *P. aeruginosa* and photographated after 24 hours of culture, Figure 52. For all tested bacteria, CPX-free membrane without irradiation showed no inhibitory area, while CPX loaded membranes not irradiated reported a mean diameter inhibition of 1 cm both for *Pseudomonas aeruginosa* (Pa) and *Staphylococcus aureus* (Sa) demonstrating that matrices are capable to release the drug and to preserve its activity.

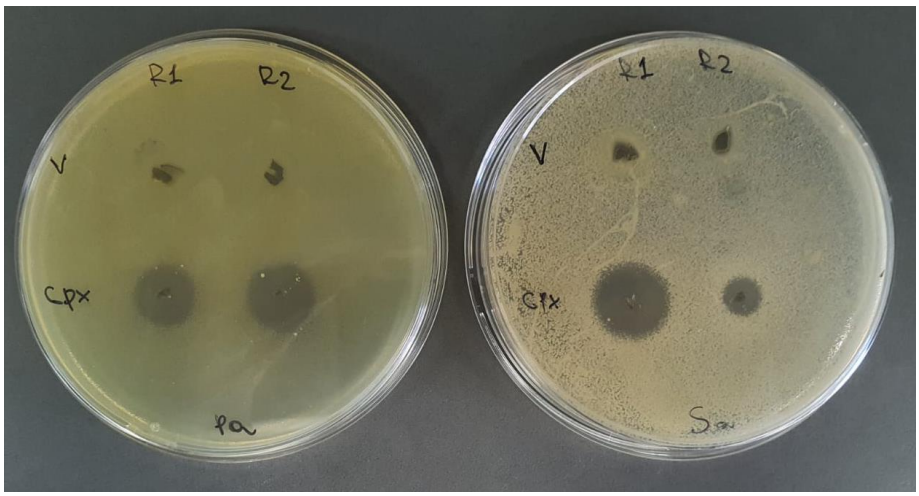

Figure 52. Cultures of Pseudomonas aeruginosa (Pa) (a) and Staphylococcus aureus (Sa) (b) incubated for 24 hours in presence of CPX-free electrospun membranes and CPX-loaded matrices (1.8 % w/w, CPX loading about 15 μg)

In Figure 53 shows the effects of the irradiation in drug-free membranes and the synergic effect on CPX-loaded sample. Increased bacterial inhibition zones were observed for drug-loaded irradiated membranes (red oval) with the respect of untreated drug-free membrane (blue oval) and drug-free irradiated membrane (yellow oval). A further increment was noticed for drug-loaded irradiated membranes (green oval) as result of combined effect of NIR light exposure and drug release. Results showed that the local temperature increase in the membrane resulted capable to induce a certain bacterial inhibition growth. Furthermore, the NIR light exposure caused a huge release of the CPX in drug-loaded membranes generating greater inhibition zones; thus it is conceivable a synergistic effect achieved from irradiated drug-loaded membranes.

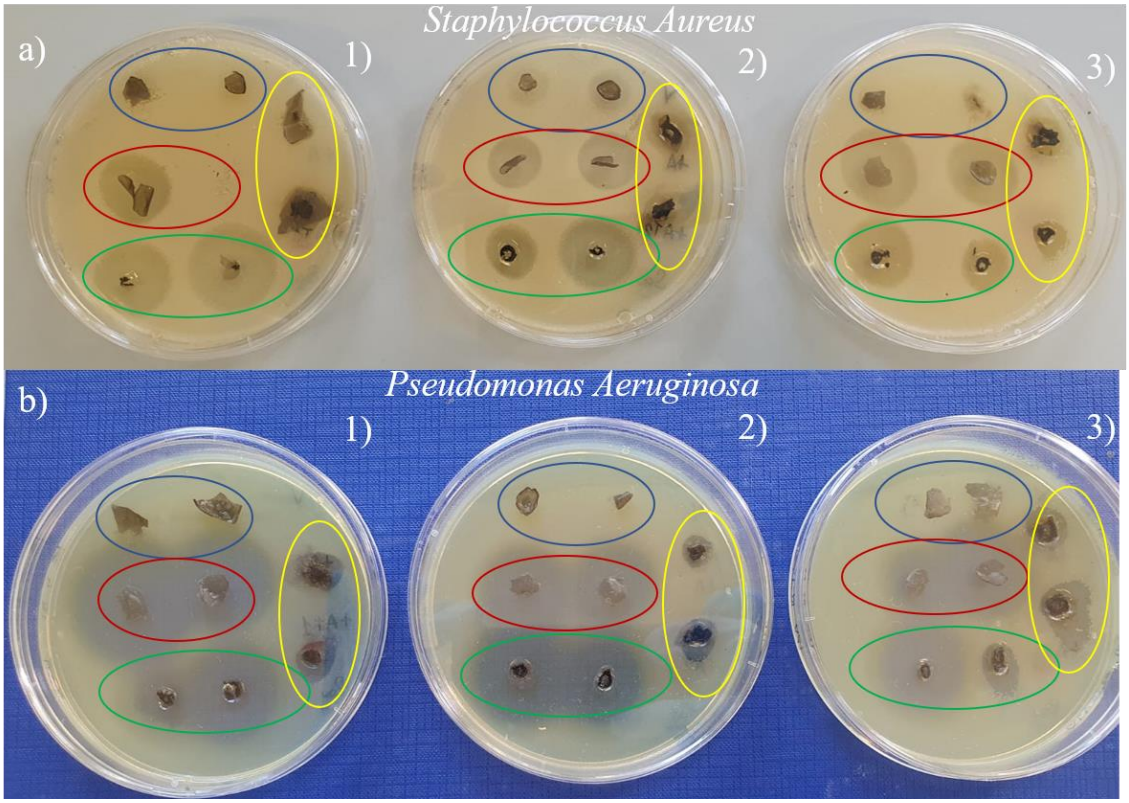

Figure 53. Inhibition zones of electrospun CPX-free and CPX-loaded membranes in response to NIR light exposure (Laser 808 nm, 10W, 125 seconds) against a) Staphylococcus aureus; b) Pseudomonas aeruginosa. Legend: Blue oval = CPX-free membranes with no irradiation; yellow oval = CPX-free membranes irradiated; red oval CPX-loaded membranes; green oval CPX-loaded membranes irradiated. Numbers 1,2 or 3 represent the consecutive irradiation cycles executed (interval time between irradiations =30 minutes)

Inhibition diameters of previous experiments were reported in Figure 54. Considering drug-free membranes exposed 1, 2 or 3 times to NIR light, the mean diameter size of inhibition zones growed according to the number of exposures demonstrating the ability of graphene oxide (GO) to reproduce the thermogenic effect. Drug-loaded membranes exposed 1, 2 or 3 times to NIR light showed mean diameter sizes of inhibition zones 2-fold larger than CPX-free membranes (up to 2 cm for *S.aureus* and 2.5 cm for *P. aeruginosa*) and the cumulative effect of more exposure was confirmed.

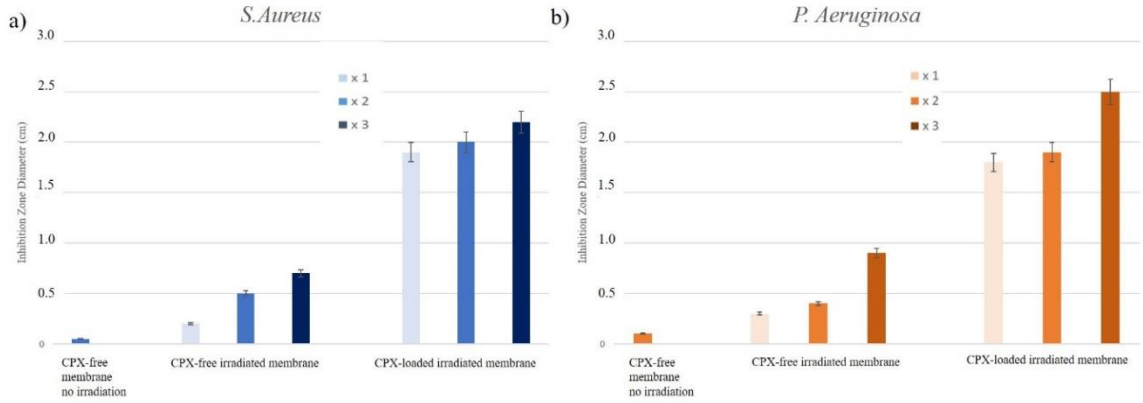

Figure 54. Diameter size of inhibition zones normalized for scaffold dimension for S. aureus and P. aeruginosa. Control is represented by CPX-free membrane without irradiation. Irradiation cycles are reported as x1, x2, x3. Data are reported as mean value ± standard deviation (n= 3)

The NIR exposure promoted the release of CPX from electrospun membranes as more as it was repeated. There were no differences in the diameters of inhibition zones after 48 hours of culture, suggesting the CPX-loaded electrospun membranes retained a long-lasting antibacterial activity against *S.aureus* and *P. aeruginosa* resulting as suitable for wound dressing applications.

To confirm data reported, the count of viable bacteria was evaluated and expressed as logarithmic reduction (Figure 55) after 24 hours of incubation of bacteria in the presence of membranes after NIR light exposure. Samples cultured above CPX-free membrane without any irradiation exerted a minimal reduction in the bacterial count for both microorganisms as control (1.6×10^8). The isolated effect of NIR light exposure was highlighted in CPX-free irradiated membranes for *S.aureus* and resulted not significant for *P.aeruginosa.* In particular, in *S.aureus* samples the irradiation reduced more the bacteria viable count as the drug-free membranes were irradiated repeated times, from 1.1×10^8 after first irradiation up to 1.1×10^7 CFU/ml after the third one. In *P.aeruginosa* samples, the effect of irradiated CPX-free membranes resulted less active and no significant differences were reported between one and three cycles of NIR light treatment.

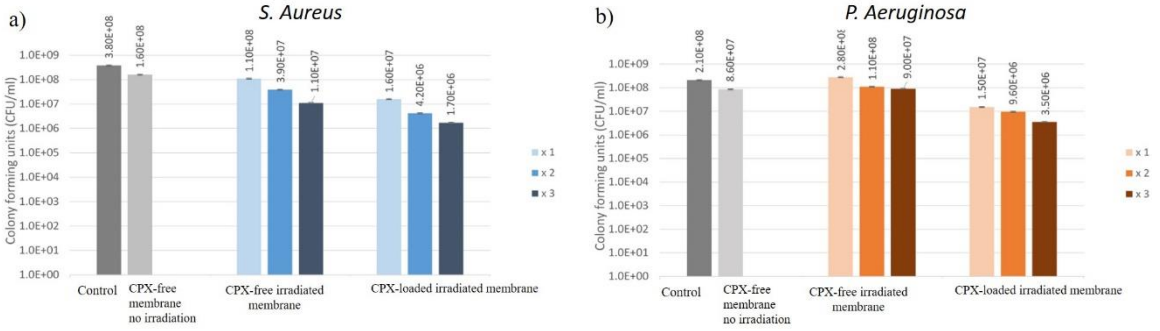

Figure 55. Viable bacteria a) S.aureus and b) P.aeruginosa expressed as CFU/ml after 24 hours of incubation at 37°C in Mueller Hinton (MH) medium containing laser-treated membranes loaded or not with ciprofloxacin. CPX-free membrane no irradiation represents bacteria cultured in MH medium for 24 hours at 37°C; CPX-free irradiated membrane represents the bacteria count in presence of CPX-loaded membrane (15µg) treated with laser. CPX-loaded irradiated membrane represents drug-loaded membrane treated with laser. The cycles of irradiation (125 seconds, 10W) are represented by x1, x2, x3 in the legend. Viability of bacteria is compared to viability of bacteria plates cultured in MH medium without membrane or treatments. Data represented as mean value ± standard deviation. (n =3)

CPX-loaded samples after irradiation reported a more efficient reduction in viable bacteria count for both *S.aureus* and *P.aeruginosa* compared to control, Figures 55-56. The presence of the drug combined to the thermogenic effect of the membranes enhanced the capability of membrane to reduce bacteria viability up to 1.7 x 10^6 for *S.aureus* and 3.5 x 10^6 for *P. aeruginosa*. Results were better expressed in Figure 56 showing the more efficacy of CPX-loaded membranes as more they were irradiated with NIR light. In particular, CPX-loaded samples resulted more capable to reduce bacteria counts than drug-free samples after three NIR exposures, achieving a logarithmic reduction about 40% for *S.aureus* and about 70 % for *P. aeruginosa*.

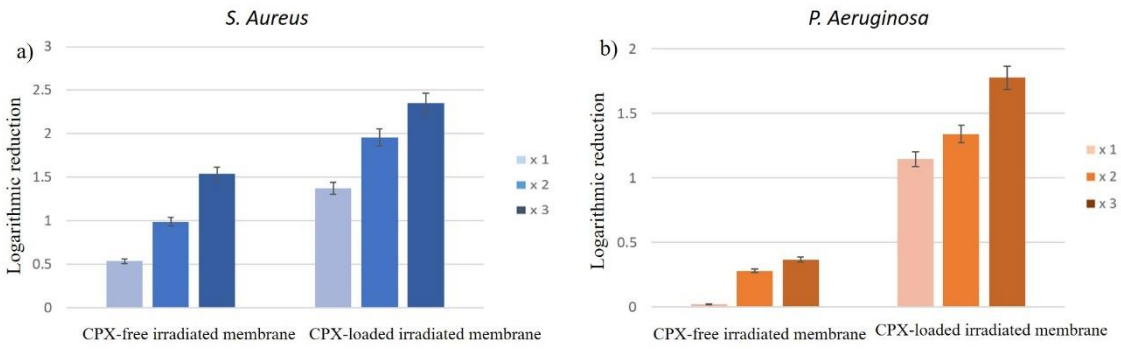

Figure 56. Logarithmic reduction comparison of CPX-free and CPX-loaded membranes after 1,2, or 3 cycles of laser irradiation (808 nm, 10 W 125 seconds) and 24 hours of bacteria culturing in MH-medium . Data represented as mean value ± standard deviation. (n =3)

4. Conclusions

Tissue engineering represents one of the most relevant and innovative field for restoring damaged tissues and organs of the human body exploiting the interactions between cells and biomaterials. On the basis of a deep knowledge of macroscopic, microscopic, biochemical, immunologic and molecular aspects of a tissutal damage, several biodevices have been fabricated achieving the adeguate regeneration of the target.

The realization of this thesis took place through the fabrication of electrospun nanofibrous membranes based on polysaccharide derivatives, obtained from gellan gum and hyaluronic acid, for tissue engineering purposes. Novel wound dressing devices and membranes for the periodontal regeneration have been characterized in terms of physico-chemical properties and *in vitro* biological performances.

The first period has been employed for the definition of instrumental parameters for the electrospinning fabrication of membranes based on two alkyl derivatives of gellan gum.

Continous uniform nanofibers (above 210 nm) have been obtained from GG-C_8 polymer blended with PVA in water solutions. Although octyl and dodecyl derivatizations on gellan gum backbone do not interfere with the typical coil-to-helix transition of GG, the comparison with unfunctionalized polymer (GG-TBA) and the dodecyl derivative (GG-C_{12}) performances has highlighted the interesting relevance of eight-carbon pendant graft in the generation of entanglements from aqueous solutions at the concentrations proposed. The addition of small amounts of quantities of ethanol to the mixture, a non-solvent for all derivatives of gellan gum, further favoured the hydrophobic aggregation of the GG-C_8 chains and it speeded up the electrospinning process without negative influences on the integrity of the fibers; in fact, morphology, fiber size, and orientation have been refined up.

Unfortunely, no significant improvements in the use of water:ethanol mixture was obtaines for GG/PVA and GG-C_{12}/PVA blends. The ES efficiency of GG-C_{12} derivative has resulted to be affected by a more robust hydrophobic interaction of polymer chains which reduced

the flexibility of the polymer and the generation of entanglments, avoiding the proper elongation of the polymer jet; thus exerting a negative effect on its spinning. These results have been confirmed by frequency sweep analyses.

On the basis of preliminary outcomes of GG-C_8 polymer, an asymmetric electrospun scaffold has been formulated representing an effective alternative to common bandages as bioactive wound dressing device. The asymmetric scaffold has been fabricated with a two-step electrospinning procedure of two polymer materials: the octyl derivative of gellan gum (GG-C_8) as a hydrophilic dermal layer and polyurethane-polycaprolactone (PU-PCL) as a hydrophobic epidermal layer. *In vitro* experiments have showed how the release of the antibiotic ciprofloxacin (CPX) and growth factor FGF-2 as well as their biological activity (antimicrobial and chemoattractant actions, respectively) could be controlled by exploiting the ionotropic properties of GG-C_8 polymer. In particular, it was found that the release profiles of CPX and FGF-2 are related differently to the ionotropic crosslinking procedure. In fact, if the scaffold is not preliminarily crosslinked with $CaCl_2$, a rapid release of CPX is obtained with a consequent effective antimicrobial activity, on the contrary, a lower release of FGF-2 is obtained with less chemoattractant activity. If the scaffold is crosslinked with $CaCl_2$, the release of FGF-2 and the chemoattractant activity are significantly increased. Considering this ionotropic dependent release, the proposed system has allowed an adequate control in the wound healing treatment, in fact a rapid release of antibiotic is necessary to obtain adequate protection of the wound during the first 48 hours of treatment, stopping a possible bacterial infection. The initial use of a non-crosslinked double-layer scaffold allowed for the release of higher amounts of CPX onto the wound bed. After dermal layer dissolution, the epidermal layer of PU-PCL electrospun could be easily detached from the GG-C_8/PVA electrospun layer, without exerting mechanical trauma. Then a new double-layer scaffold crosslinked by $CaCl_2$ could be applied in order to enhance, if required, the additional release of FGF-2 to increase and to sustain its chemoattractant activity, thus

promoting the wound healing process. *In vitro* culture of NIH3T3 fibroblasts have confirmed the bioactivity of the membrane in terms of chemoattractant property to allow the cellular homing and repopulation of the wound; thus suggesting the use of the asymmetric scaffold for wound healing purposes.

Four chemical derivatives of hyaluronic acid, at increasing hydrophobic functionalization, have been processed by electrospinning for periodontal regeneration. Optimized instrumental conditions have allowed to produce two fast-dissolving devices, based on HA-EDA-C_8 and HA-EDA-$C_{12,}$ and two scaffolds, based on HA-EDA and HA-EDA-C_{18} derivatives, which have demonstrated osteostimulatory properties by controlling the release of dexamethasone over time. Post-electrospinning EDC/NHS-mediated crosslinking has allowed to increase the hydrolytic and enzymatic resistance of the latter two matrices for more than two months. *In vitro* culture of MC3T3 seeded on membranes has showed the cytocompatibility of biomaterials and how they have promoted the cell proliferation over time. The controlled release of dexamethasone has induced the desired osteogenic response from MC3T3 cells on the twenty-eighth day of culture with the increase in ALP activity levels and calcium deposits. In light of the results obtained, membranes based on HA derivatives have a great potential to stimulate mineralization for periodontal regeneration. Furthermore, the physical and delivery properties of these membranes should be incorporated in a stacked double-faced membrane with a hydrophobic gradient and tested as future perspective.

Finally, HA-EDA based membranes have been also fabricated for chronic wound healing treatment. Antimicrobial properties have been added to the membrane after incorporation of ciprofloxacin and graphene oxide. Viscoelastic studies have demonstrated the shear-thinning behaviour of GO-loaded blends. The interactions of the nanocarbon filler with the polymer have been discussedd. Continous nanofibrillar membranes have been obtained with an average diameter of 300 nm. The crosslinking process has prolonged the hydrolytic

resistance of membranes up to 45 days. Hyperthermal properties of GO-loaded membranes have been demonstrated when exposed to NIR light achieving thermal profiles. The light also affected the release properties of ciprofloxacin from the membrane as they were time- and power-dependent from laser exposure. The influence of an external stimuli has been demostrated. Cultures o fibroblasts cultures were found to be viable once seeded over these membranes.

Antimicrobial properties of the matrices have been highlighted reporting the effective synergistic effect of the thermogenic tretment with GO-loaded membranes associated with the ciprofloxacin release for the effective logarithmic reduction of *S.aureus* and *P. aeruginosa* cultures. Results demonstrated the usefulness of using of such membranes for wound protection and the potential eradication of drug-resistant bacterial infections; thus enhancing wound healing in terms of reduced recovery time and improved repair quality.

5. Experimental section

5.1 Fabrication of electrospun membranes based on alkyl derivatives of gellan gum

5.1.1 Materials and apparatus

Gellan (Gelzan; average Mw 1000 kg/mol), sodium hydroxide, ion exchange cationic resin Dowex 50W-X8, tetrabutylammonium hydroxide (TBA-OH), bis(4-nitrophenyl) carbonate (4-NPBC), octylamine (C_8-NH_2), dodecylamine (C_{12}-NH_2), tetramethylammonium chloride (TMACl), ethanol (EtOH), acetone, and dimethyl sulfoxide anhydrous (DMSO) were purchased from Sigma Aldrich Italia. HCl 37% was acquired from Fluka. Merck supplied methanol. Polyvinyl Alcohol (PVA) 80 kDa was purchased from Serva Feinbiochemica. ^{1}H-NMR spectra were recorded employing a Bruker Avance II 300 instrument, operating at 300.12 MHz. Size exclusion chromatography (SEC) analysis was performed using a multidetector SEC system equipped with a Waters 600 pump, a Waters 410 Refractive Index Detector, a PolySep-GFC-P 4000 column, and a guard column PolySep-GFC-P (35x8 mm) purchased from Phenomenex. The calibration curve was obtained by using pullulan standards purchased from Polymer Laboratories Inc. An aqueous solution of TMACl 0.025 M and methanol 70:30 v/v was used as elution medium with a flow rate of 0.6 ml/min at 35 ± 0.1 °C. The rheological analyses were performed with an Ares G2 (TA Instruments). Electrospun mats were prepared using an instrument purchased from Linari Biomedical srl. SEM analyses were performed with the Phenom Pro X Desktop acquired from ThermoFisher Scientific. Analysis of fiber dimensional distribution and orientation was performed with ImageJ software and its plugins Diameter J and OrientationJ.

5.1.2 Hydrolysis of Gellan Gum and synthesis of its alkyl derivatives

Hydrolysis of gellan gum (1000 kDa) and the synthesis of alkyl derivatives GG-C_8 and GG-C_{12} were performed according to previous procedures reported elsewhere (Palumbo *et al.*, 2015, 2016; Agnello, Gasperini, *et al.*, 2017). The alkaline hydrolysis of Gelrite® occurred at pH 13 for 24 hours, and the resulted product., i.e. GG at lower molecular weight, was involved in the generation of its tetrabutylammonium salt, called GG-TBA. For the functionalization, 68.6 mg of 4-NPBC were dissolved in anhydrous DMSO (12 ml) (molar ratio X = 4-NPBC / GG repetitive units equal to 0.2). The solution was added dropwise to the 1% w/v GG-TBA solution in anhydrous DMSO at 40°C under orbital stirring. After 4 hours, the appropriate amount of alkylamine (molar ratio Y = NH_2-C_x/ 4-NPBC equal to 1.2) was added. After 24 hours, the work out of the reaction occurred adding 1 ml of NaCl saturated solution and stirring for 30 minutes. Each functionalized derivative was precipitated into an excess of ethanol, then washed several times with ethanol/ deionized water 8:2 v/v, absolute ethanol and then with acetone. The degree of derivatization of each derivative, calculated via ^{1}H-NMR, was expressed as mean value ± standard deviation. A typical ^{1}H-NMR spectrum of a GG-C_8 and GG-C_{12} derivatives showed peaks at δ: 0.7-0.8 (3H, s of the -C**H**$_3$ of the alkyl chain), 1.0 (br m, of the -C**H**$_2$– of the alkyl chain), 1.2 (3H, s, of the -C**H**$_3$ of rhamnose); 3.2- 4.0 (-C**H** of glucose), 5.11 (-C**H** of glucuronic acid), 5.29 (-C**H** of rhamnose).

5.1.3 Size exclusion chromatography analyses

Powders of GG, GG-C_8 and GG-C_{12} were dispersed in tetramethylammonium chloride (TMACl, 0.025 M in water) in the oven at 90°C. After 4 hours, the proper amount of methanol was added in each sample (same solvent composition of the eluent phase)

reaching a final concentration of 2.5 % w/v at room temperature. Samples and standards were filtered with 0.45µm in regenerated cellulose. The elution was performed injecting 100 µl of standard or sample on a Polysep P-4000 column, using TMACl (0.025 M): methanol 70:30 v/v as an eluent at a flow rate of 0.8 ml/min, conditioned at 35 °C, and using a calibration curve based on pullulan (range of Mw 5.9–212 kDa). All chromatograms were recorded after 30 minutes from injections.

5.1.4 Preparation of electrospun nanofibers

GG, GG-C_8, and GG-C_{12} powders were mixed with PVA powder (weight ratio equal to 1:1 w/w) and dispersed in water (5% GG, 5% GG-C_8, 4% GG-C_{12}(w/v)). After 4 hours in the oven at 90°C, blends were vigorously mixed and sonicated prior to electrospinning. In the binary blended dispersions, ethanol was added after thermal treatment to achieve the same polymer concentrations and a final water/ethanol ratio equal to 95/5 (v/v). Once homogenized, blends were introduced into glass syringe (insulated with Teflon tape) and mounted onto syringe pump. A cylindrical collector covered with aluminum foil was used for the collection of deposed fibers. The optimized experimental settings were studied by changing a parameter for each test. Flow rate was tuned from 0.130 ml/min to 0.625 ml/min, applied voltage was varied from 10 to 20 kV and needle-to-collector distance was progressively increased from 10 to 15 cm. Water vapor permeability was studied according to the ASTM standard E96-90, procedure D. Briefly, vials were filled with 4 ml of water and sealed with testing materials above and weighed. The water evaporation was monitored by weight loss of the whole system after 24 hours. The water transmission rate was calculated using the equation: $Wv\ (kg/(m^2 \cdot 24\ h)) = 4(Wo-Wr)/\pi D2$, where Wo was the mass of the whole system (including sample and water) before test, Wr is the total mass of

the device with material and water after test, D is the diameter of the sample. The values were expressed as means (n = 3).

5.1.5 Rheological characterization

Viscoelastic features were evaluated by amplitude sweep analyses using a constant angular frequency of 1 rad s^{-1} and a strain per cent range between 0.01% and 100%. Rheological behaviour of blends, prepared as described before, was investigated by a rotational rheometer (Ares G2, TA Instruments) in oscillatory frequency sweep mode using a 25-mm parallel-plate geometry. The measurements were carried out at 25 °C, within the angular frequency range 1–100 rad/s. The value of strain adopted was 1%.

5.1.6 Statistical analysis

Fiber diameter size distribution of the scaffolds was assessed from image analysis performed onto SEM micrographs. For each sample, six micrographs were taken in and each of them was investigated by counting at least fifty fiber per region (n = 300). The distribution of fiber diameter size was estimated with the aid of ImageJ software. Mean diameter ± standard deviation (SD) were also provided.

5.2 Asymmetric dual-layer device for *in situ* regeneration of skin

5.2.1 Materials and apparatus

Gellan gum (GG) (Gelzan®; average Mw 1000 kg/mol), sodium hydroxide, ion exchange cationic resin Dowex 50W-X8, tetrabutylammonium hydroxide (TBA-OH), Poly 4,4'-methylene bis(phenyl isocyanate)-1,4-butanediol/di(propylene glycol)-polycaprolactone

(PU-PCL), bis(4-nitrophenyl) carbonate (4-NPBC), octylamine (C_8-NH_2), polyvinyl pyrrolidone 10 kDa, succinic acid tetramethylammonium chloride (TMACl), ciprofloxacin (CPX), anhydrous dimethyl sulfoxide, toluidine blu, Tris-HCl, ECM gel, ethanol (EtOH), acetone, and the Transwell® inserts were obtained from Sigma Aldrich Italia. HCl 37% was purchased from J.T. Baker. Methanol was purchased from Merck KGaA. Polyvinyl alcohol (PVA) 80 kDa was purchased from Serva Feinbiochemica. N,N'-dimethylformamide (DMF), N,N'-dimethylacetamide (DMA), tetrahydrofuran (THF) and 1,4-dioxane were purchased from VWR (Italy). DMEM and fetal bovine serum obtained from Euroclone s.r.l. ELISA kit for FGF-2 was purchased from Thermo scientific. [3-(4,5-dimethylthiazol-2-yl)-5-(3-carboxymethoxyphenyl)-2-(4-sulfophenyl)-2H-tetrazolium] (CellTiter 96® AQueous One Solution Cell Proliferation) was purchased from Promega.

^{1}H-NMR spectra were recorded with a Bruker Avance II 300 instrument operating at 300.12 MHz at room temperature with deuterated water and NaOD as a solution for polysaccharide samples, whereas d_6-DMF was employed for the PU-PCL.

SEC analyses were performed as reported previously. Electrospun mats were produced using a custom instrument. SEM analyses were performed with the Phenom Pro X Desktop obtained from ThermoFisher. Microparticles were produced with the Buchi Nano B 90 HP spray dried from Flawil (Switzerland). Crystallographic profiles were acquired with XPert Pro (2θ, 40 kV, 40 mA) at a scan rate of 2 degrees per minute in the range 5 - 60°. The water vapor transmission rate (WVTR) was evaluated by using a PermeH2O apparatus at 37 ◦C and with relative humidity of 50% according to ASTM standard E96, Standard test methods for water vapour transmission of materials) (Xu *et al.*, 2016). The analysis was performed in triplicate and results expressed as mean permeability (g/m2·24 h) ± standard deviation

5.2.2 Hydrolysis of Gellan Gum (GG) and synthesis of its octyl derivative (GG-C_8)

The hydrolysis and the synthesis of the octyl derivative of gellan gum was performed as previously described in paragraph 5.1.2.

5.2.3 Production of ciprofloxacin microparticles (CPX MPs)

Solid dispersions of ciprofloxacin (CPX) hemisuccinate were produced as microparticles (MPs) with the Büchi Nano Spray Dryer B-90 HP as reported elsewhere (Mesallati and Tajber, 2017). Briefly, 59.1 mg of CPX and 20.9 mg of succinic acid (molar ratio 1:1) were dissolved in slightly warm deionized water at 2% w/v. After dissolution, a further addition of PVP (10 kDa) at 20 % w/w respect to the weight of CPX hemisuccinate was performed at room temperature. Instrumental settings adopted were: air flow rate 100 L/min; inlet temperature 110°C, spray 78% and frequency 122 kHz. The drug loading of microparticles was determined by UV spectrophotometry using a calibration curve (range 0-0.025 mg/ml) at 277 nm in phosphate buffer at pH 3 and resulted to be 55.2 % w/w ± 0.5. The solubility of CPX MPs was tested in different organic solvents such as 1,4-dioxane, DMF, DMA, THF and their 1:1 v/v mixtures (in the range of 2-10% w/v of CPX nominal content in microparticles).

5.2.4 Set-up of electrospinning parameters and fabrication of the double-layer electrospun membrane

The fabrication of the double-layer membrane occurred in two steps. The hydrophilic layer composed of GG-C_8 and PVA was the first produced considering literature reference

(Vashisth *et al.*, 2014). Briefly, GG-C_8 powder was mixed with PVA powder (1:1 w/w) and dispersed in deionized water at 4% w/v. The proper homogenization occurred after 4 hours at 90°C in oven and vigorous mechanical stirrings. Once the dispersion was cold, FGF-2 was dissolved in the aqueous mixture of GG-C_8/PVA (25 ng of FGF-2 every mg of polymers) in similar conditions reported in the literature (Zomer Volpato *et al.*, 2012). ES parameters were: flow rate 0.0085 ml/min, electric field 21-23 kV, distance 14 cm; rate of mandrel 70 rpm. The FGF-2 loading into hydrophilic layer was determined by ELISA and expressed as ng of growth factor per mg of both polymers. Once GG-C_8/PVA layer was produced, it was dried under a fume hood, peeled off from aluminum and re-fixed on the mandrel.

In the second step, the PU-PCL solution in a suitable organic solvent (in the absence or in the presence of CPX) was electrospun so that its nanofibers were deposited on the hydrophilic layer. To select the most suitable solvent, PU-PCL copolymer was preliminary dissolved in organic blends, such as DMF, DMA, DMF:THF 1:1 v/v or DMA:THF 1:1 v/v, at 5% w/v at room temperature for 24 hours under stirring. The preliminary tests selected the mixture DMF:THF 1:1 v/v for the processing of the polyurethane layer. CPX-MPs were homogenized into polymer solution through 30 minutes cycles of vortex agitation and sonication, repeated twice.

ES parameters for polyurethane layer were: flow rate 0.01 ml/min, electric field 10 kV, distance 20 cm, rate of mandrel 70 rpm. The same parameters were used for the drug loaded blend. The loading of CPX into PU-PCL layer was evaluated extracting with DPBS pH 7.4 at 37°C and plotting UV results at 277 nm against a calibration curve (range 0-0.025 mg/ml) in phosphate buffer at pH 3. CPX loading resulted equal to 2% w/w. The double-layer membrane was dried under a fume hood for three days, peeled off the aluminum foil and stored at -20°C until its use.

5.2.5 Characterization of the double-layered electrospun membrane: SEM analysis, swelling degree, GG-C_8 dissolution and release studies

Single-layer and double-layer electrospun membranes were observed through a scanning electron microscope (SEM). The swelling degrees of crosslinked membranes (1 or 0.1M $CaCl_2$) were expressed as ratio of swollen weight/dry weight and reported as Q value.

Samples were crosslinked, dried, weighed and soaked in 5 ml of DPBS pH 7.4 in orbital shaker at 37°C. After 24 hours, scaffolds were gently dried with a blotting paper and weighted.

Hydrolysis of hydrophilic layer and the release actives (CPX and FGF-2) was evaluated with Franz cells on round-shaped dual-layer membrane (diameter 19 mm) cut out from dried scaffold. Samples were immediately used or crosslinked in $CaCl_2$ 0.1 or 1 M for 30 minutes at 37 °C and then rinsed in PBS pH 7.4 to remove the residues of the crosslinker solution.

The membranes were sealed on Franz cells (orifice diameter 14 mm) using an O-ring and a clip exposing the hydrophilic layer to the acceptor compartment, filled with PBS pH 6.8. The donor compartment was plein and all releases were followed keeping the apparatus at 35°C. At predetermined time intervals, a proper volume was withdrawn from the acceptor compartment and replaced with fresh medium.

The toluidine blue assay, reported elsewhere (West, Strohfus and Santiago, 2000), allowed the quantification of GG-C_8 dissolved over time. In particular, 50 μM of toluidine blue O in 50 mM Tris-HCl buffer at pH 7.3 constitutes the dye solution for the assay. Sample were prepared by mixing 0.1 ml of aqueous medium containing GG-C_8 and 3.9 ml of dye solution. After incubation for 20 minutes at 25°C, the absorbance at 530 nm of the mixture was quantified. The linear regression provided the slope of the standard curve for the GG-

C_8 (0 and 0.5 mg/ml). Results were expressed as the percentage of dissolved GG-C_8 compared to the total amount of polysaccharide in each sample.

The CPX released from the PU-PCL layer was determined at 277 nm spectrophotometrically. The amount of FGF-2 released from the GG-C_8/PVA layer was determined using an ELISA kit.

5.2.6 Cell culture

The NIH 3T3 cell line was expanded with low glucose DMEM with the supplement of 10% v/v of FBS, and penicillin 100 μg/ml, streptomycin 100 μg/ml and amphotericin B 0.625 μg/ml.

5.2.7 Cytocompatibility assay

Round-shaped double-layer membranes (both empty and loaded with FGF-2 and CPX) crosslinked in $CaCl_2$ 1 M were placed into cell-crown inserts 48 well plates after sterilization under UV light at 254 nm (30 minutes per side). Cultured NIH 3T3 fibroblasts (passage 5) were suspended in complete DMEM and 1×10^5 cells were loaded on the hydrophilic layer of the membrane. After 30 minutes of incubation, insert were washed and moved to other well plates. 0.5 ml of DMEM was added to each well and replaced every two days with fresh medium. Cell viability was evaluated after 1, 3 and 7 days of incubation using the MTS assay. In particular, withdrawn samples were incubated for 4 hours at 37 °C, and 5% CO_2 with a 20% v/v solution of MTS in supplemented DMEM and, then, the absorbance at 492 nm of the solution was read with a multiplate spectrophotometer reader (Multiskan EX Thermo Scientific). Cells cultured on tissue culture plate (48 well) without the sample were used as a positive control.

5.2.8 Antibacterial activity

Viable plate counts method was used to monitor the effectiveness of the antibacterial activity of CPX- loaded membranes at different conditions (Schillaci *et al.*, 2010). The antimicrobial activity was evaluated on drug-loaded samples (t0) and on samples recovered after 7 (t7) and 14 (t14) days of immersion in releasing conditions to determine the efficiency of the device in terms of inhibition of bacterial growth. In particular, samples loaded with CPX 2% w/w and samples recovered from Franz cells in comparison with samples without antibiotic, were fixed in cell-crown inserts 24 well plates and sealed with the plastic O-ring exposing the hydrophobic layer to the inner volume of the insert.

Then, the sealed inserts were filled with 1 ml of Mueller Hinton 2 (MH2) medium in 24-well plates; two replicates were done for each system at different times (24 and 48 hours). A bacterial suspension of *Staphylococcus aureus* ATCC 25923 culture, whose turbidity was equivalent to 0.5 McFarland standard, was diluted 1:20 in NaCl 0.9% w/v to get the concentration of 5×10^6 colony-forming unit (CFU)/ml, and 100 µl were added to each well containing tested samples or growth control and incubated at 37°C under stationary conditions.

After 24 and 48 hours of incubation, 100 µl of bacterial suspension was removed from each well, and utilized for the bacterial count. Briefly, the inocula were added in test tubes with 10 ml of NaCl (0.9% w/v solution), six 10-fold dilutions were prepared and 100 µl aliquots of each dilution were plated onto Tryptic Soy Agar (TSA) (Sigma Aldrich, USA) plates, followed by incubation at 37°C overnight. Each assay was performed in triplicate and repeated at least twice. In order to quantify the number of viable bacteria present in each system, the value of CFU /ml was determined, and the antibacterial activity was expressed in terms of logarithmic (log) reduction. Log reduction was calculated by subtracting the

difference between the log CFU/ml of the growth control (test without antibiotic) and the log CFU/ml of starting sample (t0) loaded with CPX 2% w/w, or samples recovered after 7 (t7) and 14 days (t14) of CPX release.

5.2.9 Scratch test

Cells were seeded into a 24-well plate and cultured in medium containing 10% v/v of FBS until 90% confluence. Linear scratches were generated over the cell monolayer with the help of a 200 µl plastic pipette tip. Two washes with phosphate buffer removed every residue of cellular debris. Previously, round-shaped double-layer membranes (bearing FGF-2 and CPX) were immersed in DPBS or crosslinked (0.1 M or 1M $CaCl_2$) and then incubated in serum-free medium for 24 hours (37°C, 5% CO_2). After this time, the medium was withdrawn and poured over the scratched cell monolayer. The scratch closure was evaluated in the following 72 hours with the help of an inverted microscope and reported as images underlying the uncovered plastic area. Cells cultured with serum-free DMEM were used as a control.

5.2.10 Cell chemoattraction assay

Round-shaped membranes of 14 mm diameter, full loaded (FGF-2 and CPX) were cut and sterilized under UV irradiation at 254 nm for 30 minutes per side. Membranes investigated were untreated and crosslinked (bath $CaCl_2$ 0.1 or 1 M). After 30 minutes, crosslinker residuals were removed by PBS washings (pH 7.4). Transwell inserts (pore size 8 µm) were filled with 100 µl of a Matrigel™ solution diluted 1:1 v/v with serum-free cell culture medium and incubated at 37°C. When gelation occurred, inserts were placed above wells containing the membranes. The bottom chamber was filled with 600 µl of serum-free

medium. Pellets of NIH 3T3 fibroblasts were resuspended in serum-free medium, and 200 µl of this suspension were seeded above the thin Matrigel layer with a concentration of 2.5 × 10^5 cells/ml. After 24 hours, the inserts were removed, washed in PBS and the upper chamber was cleaned with a cotton-tipped applicator. Cells adhered on the bottom side were fixed by soaking the inserts in 70% of ethanol for 10 minutes. Once dried, inserts were immersed in crystal violet solution (0.2 % w/w) for staining. After 10 minutes, they were washed and dried. Adherent cells on the bottom side of the inserts were counted with an inverted microscope with 40X objective in five random fields of the insert layer.

5.2.11 Statistical analysis

Fiber diameters were estimated from SEM images using ImageJ and Origin software analysing fifty different measurements, taken from four different regions (n = 200) reporting data as mean ± standard deviation (SD). Data obtained from the biological and microbiological tests were presented as mean ± SD. Statistical analysis for significance was performed by means of Student's t-test, assuming two-tailed distribution and unequal variance. Values of $p<0.05$ were considered statistically significant.

5.3 Fabrication of electrospun membranes based on hyaluronan derivatives for periodontal regeneration

5.3.1 Materials and apparatus

Hyaluronic acid (HA_{HMW}, 1025 kDa) was purchased from Altergon (Italy). HA_{LMW} and its tetrabutylammonium salt were produced as reported elsewhere (Fiorica *et al.*, 2013; Pitarresi *et al.*, 2013). The hyaluronan derivative, HA-EDA, HA-EDA-C_8, HA-EDA-C_{12},

and HA-EDA-C_{18} were synthesized and characterized following the procedure elsewhere reported (Palumbo *et al.*, 2018).

Water-soluble tetrazolium salt (WST-8) was purchased from Sanbio (The Netherlands). Quantifluor dsDNA system was obtained from Promega Corporation (WI, USA). Glutaraldehyde solution 25% was purchased from Merk (Germany). Polyvinyl alcohol 80 kDa was purchased from Serva Feinbiochemica. Dexamethasone, hyaluronidase, methoxy poly(ethylene glycol) amines, 1-Ethyl-3-(3-dimethylaminopropyl)carbodiimide (EDC), N-hydroxysuccinimide (NHS) were acquired from Sigma-Aldrich(Italy and the Netherlands). PBS pH 7.4, α-MEM, fetal bovine serum were purchased from Gibco (The Netherlands).

^{1}H-NMR was performed using a Bruker Avance II 300 spectrometer operating at 300.12 MHz. GPC analyses was performed using an Agilent 1260 Infinity Multi-Detector Bio-SEC solution. GPC was equipped with a pump system, a PolySep-GFC-P 4000 column from Phenomenex. Analyses were performed using 0.025 M tetramethylammonium chloride solution (TMACl)/MeOH 7:3 (v/v) mixture as an eluent, with a flow of 0.6 ml/min and a column temperature of 35 °C. ATR-IR analyses determined the chemical profile of electrospun membranes or powders with a resolution of 4.0 cm^{-1} in the scanning range between 400 cm^{-1} and 4000 cm^{-1}. All UV measurements were carried out using the spectrophotometer Synergy HTX multi-mode reader from Biotek involving the use of the software Gen5 2.06. Membranes were prepared by electrospinning technique using a custom instrument (Advanced Surface Technology BV, The Netherlands). The morphology of scaffolds was observed using a SEM microscopy (Zeiss GeminiSEM, The Netherlands). Before acquisition, samples were fixed on stubs with carbon tape and sputtered with chromium or gold. The crystallographic profiles of EM and powders were acquired with XRD analysis (X'pert^3 powder, PANalytical, the Netherlands). XRD spectra were recorded using a copper sample holder at 45 kV, 40 mA (Cu-Kα1 radiation with a wavelength of 1.54

Ä), and a 2θ between 5 and 40, at a step size of 0.01°. All rheological analyses were performed using the rheometer with parallel plates cross-hatched 20 mm of diameter at 25°C or cone and plate geometry (cone angle of 2°, diameter = 40 mm, truncation 55 µm) (Ares 2000ex, the Netherlands). Water contact angles (WCA) were measured to evaluate the wettability of nanofibrous scaffolds using the optical tensiometer (OneAttension Theta Lite from Biolin Scientific, the Netherlands) by image processing of sessile drops of 4 µl for 10 seconds.

5.3.2 Synthesis of hyaluronic acid derivatives

The derivatization procedure involved the graft of different aliphatic chains and small moieties with free amino groups onto HA backbone. The native HA (HA_{HMW} 1.025 kDa) was subjected to acidic degradation following a procedure reported elsewhere (Shu *et al.*, 2002) to form its low-molecular-weight form, labelled as HA_{LMW}, and then its tetrabutylammonium salt with a ion-exchange cationic resin (Dowex 50 W × 8-200) as similarly adopted for gellan gum derivatives. In the first step of the syntheses, considering a molar ratio 4-NPBC/HA-TBA repetitive units equal to 0.7, the activation of the primary hydroxyl of each repetitive unit occurred by adding the amount required of 4-NPBC to a 1% w/v HA-TBA solution in DMSO at 40°C for 4 hours under stirring (Giammona, Palumbo and Pitarresi, 2009).

The HA-EDA derivative was obtained dripping a solution of EDA by using a molar ratio equal to 10 respect to the moles of 4-NPBC. The solution was kept at 40°C for three hours. After this time, 1 ml of a NaCl saturated solution was added under stirring for thirty minutes at room temperature to obtain the sodium salt of the polymer. The obtained HA-EDA polymer was precipitated into acetone and then washed several times with ethanol/water 8:2 v/v and acetone at room temperature and dried under vacuum.

In the syntheses of alkyl derivatives of HA, the grafting of aliphatic chains (C_8-NH_2, C_{12}-NH_2, C_{18}-NH_2) occurred before the dripping of EDA. In particular, after the activation with 4-NPBC, the aliphatic amines were added in the respective reaction mixtures (molar ratio C_n-NH_2/4-NPBC equal to 0.5). After 24 hours at 60°C, EDA (molar ratio equal to 10 respect to the moles of 4-NPBC) was dripped into the solution and left at 40°C for three hours. At the end of the last step, NaCl saturated solution was added to each flask for thirty minutes under stirring before precipitation into diethyl ether/chloroform 1:1 v/v for HA-EDA-C_{18} derivative and with acetone for HA-EDA-C_8 and HA-EDA-C_{12} derivatives. The purification of HA-EDA-C_{18} product was carried out in hot diethyl ether/chloroform 1:1 v/v, and then with ethanol/water 8:2 v/v at room temperature with a final washing in ethanol. HA-EDA-C_8 and HA-EDA-C_{12} were washed in ethanol/water 8:2 v/v at room temperature with a final washing in ethanol. The functionalization degrees in alkyl chains and EDA were expressed as mol % ± standard deviation. All products were obtained as white powders with a weight yield of 70-80 % and they were characterized by ^{1}H-NMR analysis (Palumbo *et al.*, 2016). All ^{1}H-NMR spectra showed principal peaks of the HA structure, commonly reported in the literature. The TNBS assay was carried out on HA derivatives solutions and resulting hydrogels after thirty minutes of EDC/NHS crosslinking. Powders of HA derivatives, and standards were dissolved in tetraborate buffer at pH 9.3 at 8 mg ml^{-1}. The methoxy poly(ethylene glycol) amines were used for the calibration curve (range 0.01 mg ml^{-1}– 0.001 mg ml^{-1}) as standards. Each well was filled with 900 µl of the buffer, 50 µl of a solution of TNBS 0.03 M, and 50 µl of samples/standards. After two hours of incubation at room temperature in the dark, the absorbance of each well was measured at 500 nm. Values of EDA functionalization was calculated as mean between ^{1}H-NMR analysis and colorimetric assay and expressed as mol % of functionalization.

5.3.3 Set-up of electrospinning condition and electrospun mats fabrication procedure

Preliminary electrospinning tests were carried out to set solution parameters such as concentration and weight ratio (WR). Each HA derivatives and PVA were both tested at 2.5%, 5%, and 6% w/v, in relative different blend ratios in aqueous solutions and mixed with HPCD at three concentrations (4.16%, 8.33% and 10% w/v). Once detected general parameters, viscosity (η) of spinnable blends was obtained recording shear rates ranging from 0.1 to 100 s^{-1}, while viscoelastic features were studied by amplitude sweep analyses using a constant angular frequency of 1 rad s^{-1} and a strain per cent (range 0.01% - 100%), and by frequency sweep tests (within linear viscoelastic region) between 1 and 100 rad s^{-1}. Crosslinked hydrogels were prepared adding crosslinking chemicals in the molar ratio of EDC/NHS/carboxyl groups of HA repetitive unit = 5: 2: 1 to the blends for thirty minutes at room temperature. Fabrication of electrospun mats (EM) was performed by dissolving PVA (80 kDa) powder in water (5% w/v) at 90°C for 2 hours. After cooling at room temperature, hydroxypropyl-β cyclodextrins were dissolved to reach a final concentration of 8.33% w/v, then HA-EDA, HA-EDA-C_8, or HA-EDA-C_{12} (WR HAn:PVA 1:1), or HA-EDA-C_{18} (WR HAn:PVA 0.5:1) powder were added generating H*n* solutions, where *n* (0, 8, 12 and 18) is related to the number of carbons chemically grafted on the HA backbone. After 24 hours, the incorporation of the Dex (ranging from 0.083 to 0.166 % w/w to the sum of polymers weights) occurred to generate H*n*X/2 or H*n*X solution, where X/2 and X declare the lowest and the highest amount of incorporated Dex. The feeding rate of the syringe pump was finely tuned from 0.1 to 0.8 ml h^{-1}, and the applied electric field was changed from 20 kV to 29 kV. Selected mats were dried under hood for five days and easily peeled off the aluminium foil.

Round-shaped matrices of 1 cm of diameter were soaked for thirty minutes at room temperature in 500 µl of a crosslinking bath of ethanol and water 75:25 v/v where EDC and NHS were previously dissolved in the molar ratio EDC/NHS/carboxyl groups = 5: 2: 1 following a similar reported procedure (Nam, Kimura and Kishida, 2008). Residual unreacted chemicals were quickly removed from mats by washings in cold ethanol.

5.3.4 Hydrolysis and Dex-releasing profile from mats

The hydrolysis studies of mats and the Dex releasing profiles were performed at 37 °C on an oscillatory plate for two months in three aqueous media, such as pure PBS 1X pH 7.4 (PBS), and PBS with the addition of hyaluronidase (Hyal 5 U ml^{-1}) or fetal bovine serum (FBS 10% v/v).

The amount of released Dex was quantified by UV spectrophotometer at 241 nm, while the hydrolyses of the electrospun matrices were evaluated through carbazole assay (Cesaretti *et al.*, 2003). In particular, for carbazole assay 96-well plates were filled with 25 µl of withdrawn samples, then 100 µl of 25 mM sodium tetraborate solution in sulfuric acid was added and the plates were heated at 100°C in an oven. After 10 minutes, plates were cooled down at room temperature for 15 minutes. In every well, 25 µl of a 0.125% carbazole solution in absolute ethanol was added and plates heated once again at 100°C for 10 minutes. After the second cooling process at room temperature for 15 minutes, absorbance from the 96-well plates was read in a multiplate reader (wavelength of 550 nm) and plotted against known HA concentrations standards. The linear regression provided the slope of the standard curve for the HA concentration range between 0 and 0.5 mg ml^{-1}. Results were expressed as the percentage of released uronic acid with respect to the total amount in each sample.

5.3.5 In vitro cell culture

Round-shaped matrices of 1 cm of diameter were disinfected for five minutes by Argon plasma using a radio frequency glow discharge plasma cleaner (PDC-001, Harrick Scientific Corp., USA) before all cell culture experiments. MC3T3 were seeded on matrices at a cell density equal to 2.5 x $10^4/cm^2$ and cultured with a growth medium (α-MEM supplemented with 10% FBS, 100 U ml^{-1} penicillin and 100 µg ml^{-1} streptomycin) at 37°C and 5% CO_2.

The CCK-8 assay (n=3) was performed at day 1, 3, and 7 according to the protocol provided by the manufacture. All samples were compared to blank.

For the DNA quantification and alkaline phosphatase (ALP) activity assay, MC3T3 cells were seeded on matrices in triplicate (cell density equal to 2.5 x $10^4/cm^2$) and incubated using a Dex-free osteogenic medium (α-MEM supplemented with 10% FBS, 50 mg ml^{-1} ascorbic acid, 10 mM sodium β-glycerophosphate, 100 U ml^{-1} penicillin and 100 µg ml^{-1} streptomycin) at 37°C and 5% CO_2 and compared to controls with no cells and a complete osteogenic medium with the addition of dexamethasone (10^{-8}M). After 2, 7, 14 and 28 days of culture, membranes were washed twice with sterile PBS, collected and immersed in 1 ml of deionized water, then sonication and two freeze-thaw cycles were performed. For DNA quantification was used the protocol of the factory. ALP activities were measured by a p-nitrophenyl phosphate colorimetric assay, according to the manufacturer's instructions. In particular, the absorbance of samples was read at 405 nm, and ALP activity was normalized according to the DNA content for each sample.

Mineralization on membranes was determined by the calcium content assay. The previously described seeding and culturing protocols were used and, at day 28 and 35, medium was substituted with 1 ml of acetic acid to dissolve calcium deposits due to the mineralizing processes. The working solution of the assay was prepared mixing different solution in a

specific ratio: 5 parts of a solution 14.8M ethanolamine in boric acid buffer at pH 11; 5 parts of a second solution prepared dissolving 80 mg of O-cresolphtalein complexone in a 3.3 mM KOH solution and adding 500 µl of acetic acid 0.5 M; 2 parts of a third solution (1g of 8-hydroxyquinoline in 20 ml ethanol 95% v/v); and 88 parts of MilliQ water. A Ca-stock solution 1 mg ml^{-1} was used for the calibration curve in the range 0 -100 µg/ml. For the determination of calcium, 10 µl of samples or standards and 300 µl of working solution were mixed. After 10 minutes of incubation at room temperature, absorbance was read at 570 nm in a plate reader. All measurements were performed in duplicate.

5.3.6 Statistical analysis

Fiber diameters of scaffolds were estimated from resulting SEM images using ImageJ software. Fifty different measurements were taken from six different regions of each electrospun membrane (n = 300). Data were represented as mean ± standard deviation (SD). The distribution of diameters was estimated with the help of the ImageJ software and Origin. Data obtained from CCK-8, DNA, ALP, and calcium assays were presented as mean ± standard deviation. Statistical analysis for significance was performed by means of Student's t-test assuming two-tailed distribution and unequal variance and one-way ANOVA. Values of $p<0.05$ were considered statistically significant.

5.4 Evaluation of therapeutic properties of electrospun membrane of HA-EDA and graphene oxide

The materials and methods used in this survay are the same as previously reported. In addition, rheological tests were carried out with DHR-2 TA instrument with parallel plate of 8 mm with radial stripes and a conical geometry with a diameter of 40 mm and 2° angle.

HPLC analyses employed HPLC Agilent 1260 infinity with a quaternary pump VL g1311C, a DAD 1260VL detector, with injection of 50 µl. Electrospun membranes were prepared with the instrument NF-130 (ATeN Center). Hyperthermal effect was obtained exposing membranes to a laser beam of 810 nm.

5.4.1 Preparation procedure and rheological characterization of HA-EDA blend with graphene oxide

Blends were prepared mixing equal amounts of HA-EDA and PVA (80 kDa) powders both at 4% w/v with HPCD at 8.33% w/v in DI water by sonication cycles and vortex mixing. The homogenization was completed after 24 hours in an orbital shaker at 37 °C generating a HA blend. The incorporation of GO occurred after 24 hours at the concentration of 0.02% or 0.03% w/v. These blends were called HAGOa and HAGOb, respectively.

Rheological tests were carried out at 25°C by deposition of 200 µl of sample in triplicate. Elongational ability of blends was tested by flow ramp studies recording the change in viscosity as a function of shear rate (0.1 - 100 s^{-1}) using the cone-plate geometry. The linear region, where storage and loss moduli are independent of stress, was investigated by amplitude sweep analyses using a constant angular frequency of 1 rad s^{-1} in the strain percentage range from 0.01 to 100%. Viscoelastic studies were conducted by frequency sweep tests using parallel plates to determine the relationship of complex viscosity with the angular frequency. The settings of these experiments were at fixed strain of 10% and recording G' and G'' moduli in the range 1-100 rad s^{-1}.

5.4.2 Preparation procedure of HA-EDA based membranes

Polymeric blends were introduced in a syringe of 5 ml and applied to pump. The flow rate was tested in the range 0.1-0.5 ml/h and the generation of a stable Taylor's cone was evaluated.

Nanofibers were collected on a cylindrical collector covered with aluminium foil. The nozzle-to-collector distance was evaluated in the range of 8-15 cm. The applied voltage was tuned from 10 to 40 kV. At the end of the spinning, membranes were dried under fume hood for three days and then peeled off the aluminium. Membranes were characterized by Phenom Pro X Desktop of ThermoFisher Scientific and images elaborated with the software ImageJ and its plugins. Crosslinking procedure occurred by EDC/NHS coupling setting a molar ratio (nEDC: nNHS: nCOOH of HA equal to 5: 2: 1). Aiming to the preservation of fibrillar structure, the procedure occurred in dichloromethane, ethanol, or in a mixture 75:25 v/v of ethanol and water at 25°C for 30 minutes.

5.4.3 Swelling degree, chemical and enzymatic hydrolysis of HA-based membranes with GO

Round shaped membranes of 1 cm^2 were cut. The swelling ability of membranes was tested soaking dried weighed pieces in 24 well plates with 1 ml of DPBS at pH 7.4. Sample were incubated at 37°C for 24 hours. The degree of swelling was calculated as Q value expressed as ratio of swollen weight/dry weight. Test was performed in triplicate. The hydrolysis of membranes was evaluated by carbazole assay as reported previously. Results were plotted against known HA concentrations standards. The linear regression provided the slope of the standard curve for the HA concentration range between 0 and 0.5 mg ml^{-1}. The results were

expressed as the percentage of uronic acid released relative to respect to the total amount in each sample.

5.4.4 Hyperthermal studies of HAGO membranes

Crosslinked membranes were deposited on the bottom of 24-well plates with 2 ml of DPBS pH 7.4. A focused laser beam (810 nm) was set in the center of the pieces at a fixed distance of 15 cm. The hyperthermic effect was evaluated by immersing a probe capable of detectin small temperature changes in the aqueous medium after predetermined laser exposures (25, 50, 75, 100, and 125 seconds).

5.4.5 Release profiles of ciprofloxacin from HAGO membranes

Spray dried microparticles of hemisuccinate ciprofloxacin were prepared as previously described. The loading of the drug occurred before the electrospinning and it was set at 5% w/w considering the sum of weights of PVA and HA in the blends. The drug loading efficiency and the releases of the drug were valued by an HPLC method reported in literature (Vella *et al.*, 2015). The method used a reverse phase Luna C18 column and a mobile phase 77:23 v/v of phosphate buffer at pH 2.7 and acetonitrile with a flow rate of 1 ml/min at 25°C. Results were plotted against a calibration curve of ciprofloxacin (0.125-8 µg/ml) at 277 nm and quantified by linear regression.

The release of ciprofloxacin was evaluated by immersing membranes in 1 ml of DPBS pH 7.3 at 37 °C. At predetermined times, the aliquots were withdrawn and replaced with fresh aqueous medium.

The effect of laser exposure was related to release profiles from two series of experiments. A release profile was evaluated for one week after a single laser exposure of 25, 75 or 125

seconds at 5 and 10 W. The release profiles were also followed and compared after daily laser exposures.

5.4.6 Biological experiments

Fibroblast NIH3T3 cell line was expanded in T75 flasks with DMEM high glucose with the supplement of 10% v/v of FBS, penicillin 100 μg/ml, streptomycin 100 μg/ml and amphotericin B 0.625 μg/ml. Culture medium was refreshed every two days until 90% of confluence was reached. Round-shaped membranes were cut and disinfected by UV light at 254 nm (15 minutes per side) and then placed on cell-crown insert for 24-well plates. Cell pellets were prepared by trypsinization and seeded above membranes with a density of 2.5 x 10^4/cm^2. After 30 minutes of incubation (37 °C, 5% CO_2), the membranes were washed to remove non-adherent cells. Adhesion was evaluated by live and dead assay after 1, 3 and 7 days of cell culturing. At these times, samples were washed with sterile DPBS and stained with calcein AM and ethidium homodimer-III. After 20 minutes, membranes were visualized under inverted microscope. MTS assay was used to evaluate the proliferation of fibroblasts cultured above membranes up to 3 days. In this case, membrane were moved to another 24-well plate and soaked with a 20% solution of MTS in DMEM. After four hours of incubation (37°C, 5% CO_2), 100 μl were poured into 96 well plates and absorbance at 490 nm was read with a plate reader. Cell viability was reported as nominal absorbance and performed in triplicate.

5.4.7 Antimicrobial properties of HA-based electrospun membranes

To monitor the effectiveness of CPX- loaded membranes in different conditions, the antimicrobial activity was evaluated on drug-loaded samples to determine the efficiency of

the device in terms of inhibition of bacterial growth, viable plate counts, and the response of membranes against bacteria biofilms of *Staphylococcus aureus* ATCC 25923 and *Pseudomonas aeruginosa* ATCC 15442 as similarly reported in the literature (Schillaci *et al.*, 2010). The strains were grown overnight on Müller–Hinton (Difco) agar plates at 37 °C prior to use. The bacterial cells were collected and re-suspended in saline, and adjusted to 1 x 10^7 CFU/ml (colony forming units) by visual comparison with a 0.5 McFarland standard.

The zone of inhibition test was used to determine the antimicrobial activity of the wound dressing as result of ciprofloxacin diffusion and thermogenic effect of membranes. Squared pieces of electrospun membrane were crosslinked and placed on the bacterial lawn seeded on Müller–Hinton agar plates. Drug-free and drug-loaded membranes (1 mg = 15 μg of CPX) were exposed to 1, 2, or 3 irradiations to laser light (808 nm) for 125 s at 10W. For multiple laser exposure (2 or 3 cycles), the irradiazion was repeated every 30 minutes. After treatments, plates were incubates overnight at 37 °C and then photographed. The inhibition zone mean diameter around the dressings was measured with the help of ImageJ sofware. The zone of inhibition was normalized for the electrospun dressing diameter. Drug-free membranes and drug-loaded membranes not irradiated were used as control.

To count viability of resistant microrganisms, bacterial suspensions of *Staphylococcus aureus* and *Pseudomonas aeruginosa* cultures, whose turbidity was equivalent to 0.5 McFarland standard, were diluted 1:20 in NaCl 0.9% w/v to get the concentration of 5×10^6 colony-forming unit (CFU)/ml, and 100 μl were added to 24-well plates containing tested samples or control. Tested samples were drug-free and drug-loaded membranes exposed to NIR light for 1, 2, or 3 cycles 125s at 10W. After laser treatment, plates were incubated at 37°C under stationary conditions.

After 24 hours of incubation, 100 µl of bacterial suspension was removed from each well, and utilized for the bacterial count. Briefly, the inocula were added in test tubes with 10 ml of NaCl (0.9% w/v solution), six 10-fold dilutions were prepared and 100 µl aliquots of each dilution were plated onto Tryptic Soy Agar (TSA) (Sigma Aldrich, USA) plates, followed by incubation at 37°C overnight. Each assay was performed in triplicate and repeated at least twice. In order to quantify the number of viable bacteria present in each system, the value of CFU /ml was determined, and the antibacterial activity was expressed in terms of logarithmic (log) reduction. Log reduction was calculated by subtracting the difference between the log CFU/ml of the growth control (test without antibiotic and no irradiation) and the log CFU/ml drug-free and drug-loaded membranes after 0, 1, 2, or 3 consecutive laser irradiation (808 nm) for 125 seconds ad 15 cm of distance.

5.4.8 Statistical analysis

The fiber diameter size distribution of the scaffolds was evaluated by image analysis performed on SEM micrographs. For each sample, six micrographs were taken and studied by counting at least fifty fibers per region (n = 300). The size distribution of the fiber diameter was estimated with the help of the ImageJ software. Mean diameter ± standard deviation (SD) was also provided. Statistical analysis for significance was performed by means of Student's t-test assuming two-tailed distribution and unequal variance and one-way ANOVA. Values of $p<0.05$ were considered statistically significant.

6. Bibliography

Agnello, S., Bongiovì, F., *et al.* (2017) 'Microfluidic Fabrication of Physically Assembled Nanogels and Micrometric Fibers by Using a Hyaluronic Acid Derivative', *Macromolecular Materials and Engineering*, 302(11), pp. 1–10. doi: 10.1002/mame.201700265.

Agnello, S., Gasperini, L., *et al.* (2017) 'Synthesis, mechanical and thermal rheological properties of new gellan gum derivatives', *International Journal of Biological Macromolecules*, 98, pp. 646–653. doi: 10.1016/j.ijbiomac.2017.02.029.

Agnello, S. *et al.* (2018) 'Synthesis and evaluation of thermo-rheological behaviour and ionotropic crosslinking of new gellan gum-alkyl derivatives', *Carbohydrate Polymers*, 185, pp. 73–84. doi: 10.1016/j.carbpol.2018.01.021.

Ahire, J. J. *et al.* (2015) 'Ciprofloxacin-Eluting Nanofibers Inhibits Biofilm Formation by Pseudomonas aeruginosa and a Methicillin-Resistant Staphylococcus aureus', pp. 1–13. doi: 10.1371/journal.pone.0123648.

Ajami, S., Shahroodi, A. and Amiri, S. (2020) 'Teicoplanin-loaded chitosan-PEO nano fi bers for local antibiotic delivery and wound healing', *International Journal of Biological Macromolecules*, 162, pp. 645–656. doi: 10.1016/j.ijbiomac.2020.06.195.

Aziz, S. *et al.* (2017) 'Polymer Blending as a Novel Approach for Tuning the SPR Peaks of Silver Nanoparticles', *Polymers*, 9(12), p. 486. doi: 10.3390/polym9100486.

Bai, Y. *et al.* (2018) 'Sequential delivery of VEGF, FGF-2 and PDGF from the polymeric system enhance HUVECs angiogenesis in vitro and CAM angiogenesis', *Cellular Immunology*, 323, pp. 19–32. doi: 10.1016/j.cellimm.2017.10.008.

Barrientos, S. *et al.* (2014) 'Clinical application of growth factors and cytokines in wound healing', *Wound Repair and Regeneration*, 22(5), pp. 569–578. doi: 10.1111/wrr.12205.

Bártolo, P. J. *et al.* (2008) 'Advanced Processes to Fabricate Scaffolds for Tissue Engineering BT - Virtual Prototyping & Bio Manufacturing in Medical Applications', in, pp. 149–170. Available at: https://doi.org/10.1007/978-0-387-68831-2_8.

Behm, B. *et al.* (2012) 'Cytokines, chemokines and growth factors in wound healing', *Journal of the European Academy of Dermatology and Venereology*, 26(7), pp. 812–820. doi: 10.1111/j.1468-

3083.2011.04415.x.

Bettinger, C. J., Langer, R. and Borenstein, J. T. (2009) 'Engineering substrate topography at the Micro- and nanoscale to control cell function', *Angewandte Chemie - International Edition*, pp. 5406–5415. doi: 10.1002/anie.200805179.

Buck, E. *et al.* (2018) 'Antibacterial Properties of PLGA Electrospun Scaffolds Containing Ciprofloxacin Incorporated by Blending or Physisorption', *ACS Applied Bio Materials*, 1(3), pp. 627–635. doi: 10.1021/acsabm.8b00112.

Caballé-Serrano, J. *et al.* (2019) 'Adsorption and release kinetics of growth factors on barrier membranes for guided tissue/bone regeneration: A systematic review', *Archives of Oral Biology*. doi: 10.1016/j.archoralbio.2019.02.006.

Castaño, O. *et al.* (2018) 'Instructive microenvironments in skin wound healing: Biomaterials as signal releasing platforms', *Advanced Drug Delivery Reviews*, 129, pp. 95–117. doi: 10.1016/j.addr.2018.03.012.

Castro, A. G. B. *et al.* (2018) 'Incorporation of simvastatin in PLLA membranes for guided bone regeneration: effect of thermal treatment on simvastatin release', *RSC Advances*, 8(50), pp. 28546–28554. doi: 10.1039/c8ra04397c.

Cesaretti, M. *et al.* (2003) 'A 96-well assay for uronic acid carbazole reaction', *Carbohydrate Polymers*, 54(1), pp. 59–61. doi: 10.1016/S0144-8617(03)00144-9.

Chen, J. *et al.* (2016) 'Electrospun Gelatin Fibers with a Multiple Release of Antibiotics Accelerate Dermal Regeneration in Infected Deep Burns', *Macromolecular Bioscience*, pp. 1368–1380. doi: 10.1002/mabi.201600108.

Chen, S. *et al.* (2014) 'A three-dimensional dual-layer nano / micro fi brous structure of electrospun chitosan / poly (D , L -lactide) membrane for the improvement of cytocompatibility', *Journal of Membrane Science*, 450, pp. 224–234. doi: 10.1016/j.memsci.2013.08.007.

Chen, S. *et al.* (2018) 'Electrospinning: An enabling nanotechnology platform for drug delivery and regenerative medicine', *Advanced Drug Delivery Reviews*, 132, pp. 188–213. doi: 10.1016/j.addr.2018.05.001.

Cheng, H. *et al.* (2018) 'Biomedical application and controlled drug release of electrospun fibrous

materials', *Materials Science and Engineering C*, 90(2017), pp. 750–763. doi: 10.1016/j.msec.2018.05.007.

Chong, E. J. *et al.* (2007) 'Evaluation of electrospun PCL/gelatin nanofibrous scaffold for wound healing and layered dermal reconstitution', *Acta Biomaterialia*, 3(3 SPEC. ISS.), pp. 321–330. doi: 10.1016/j.actbio.2007.01.002.

Coburn, J. M. *et al.* (2012) 'Bioinspired nanofibers support chondrogenesis for articular cartilage repair', *Proceedings of the National Academy of Sciences of the United States of America*, 109(25), pp. 10012–10017. doi: 10.1073/pnas.1121605109.

Contreras-Càceres, R. *et al.* (2019) 'Electrospun Nanofibers : Recent Applications in Drug Delivery and Cancer Therapy', *Nanomaterials*, 9(656), pp. 1–24. doi: doi:10.3390/nano9040656.

Costerton, J. W., Stewart, P. S. and Greenberg, E. P. (1999) 'Bacterial biofilms: A common cause of persistent infections', *Science*, 284(5418), pp. 1318–1322. doi: 10.1126/science.284.5418.1318.

Cui, W. *et al.* (2010) 'Controllable growth of hydroxyapatite on electrospun poly (DL -lactide) fi bers grafted with chitosan as potential tissue engineering scaffolds', *Polymer*, 51(11), pp. 2320–2328. doi: 10.1016/j.polymer.2010.03.037.

Darby, I. A. and Hewitson, T. D. (2007) 'Fibroblast Differentiation in Wound Healing and Fibrosis', *International Review of Cytology*, 257(07), pp. 143–179. doi: 10.1016/S0074-7696(07)57004-X.

Delgado-Rivera, R. *et al.* (2009) 'Increased FGF-2 secretion and ability to support neurite outgrowth by astrocytes cultured on polyamide nanofibrillar matrices', *Matrix Biology*, 28(3), pp. 137–147. doi: 10.1016/j.matbio.2009.02.001.

Du, J. and Hsieh, Y. (2008) 'Nanofibrous membranes from aqueous electrospinning of carboxymethyl chitosan', (March). doi: 10.1088/0957-4484/19/12/125707.

Ebrahimi-hosseinzadeh, B., Pedram, M. and Hatamian-zarmi, A. (2016) 'In vivo Evaluation of Gelatin / Hyaluronic Acid Nanofiber as Burn-wound Healing and Its Comparison with ChitoHeal Gel', 17(6), pp. 820–826. doi: 10.1007/s12221-016-6259-4.

Eming, S. A., Krieg, T. and Davidson, J. M. (2007) 'Inflammation in wound repair: Molecular and cellular mechanisms', *Journal of Investigative Dermatology*, 127(3), pp. 514–525. doi: 10.1038/sj.jid.5700701.

Engler, A. J. *et al.* (2006) 'Matrix Elasticity Directs Stem Cell Lineage Specification', *Cell*, 126, pp. 677–689. doi: 10.1016/j.cell.2006.06.044.

Figueira, D. R. *et al.* (2016) 'Production and characterization of polycaprolactone- hyaluronic acid/chitosan- zein electrospun bilayer nanofibrous membrane for tissue regeneration', *International Journal of Biological Macromolecules*, 93, pp. 1100–1110. doi: 10.1016/j.ijbiomac.2016.09.080.

Fiorica, C. *et al.* (2013) 'A new hyaluronic acid pH sensitive derivative obtained by ATRP for potential oral administration of proteins', *International Journal of Pharmaceutics*, 457(1), pp. 150–157. doi: 10.1016/j.ijpharm.2013.09.005.

Fiorica, C. *et al.* (2017) 'Double-Network-Structured Graphene Oxide-Containing Nanogels as Photothermal Agents for the Treatment of Colorectal Cancer', *Biomacromolecules*, 18(3), pp. 1010–1018. doi: 10.1021/acs.biomac.6b01897.

Frykberg, R. and Banks, J. (2015) 'Challenges in the Treatment of Chronic Wounds', *Advances in Wound Care*, 4, pp. 560–582.

Gaharwar, A. K., Singh, I. and Khademhosseini, A. (2020) 'Engineered biomaterials for in situ tissue regeneration', *Nature Reviews Materials*, 5, pp. 686–705. doi: 10.1038/s41578-020-0209-x.

George, A. M. *et al.* (2020) *Biopolymer-based scaffolds: Development and biomedical applications*, *Biopolymer-Based Formulations: Biomedical and Food Applications*. Elsevier Inc. doi: 10.1016/B978-0-12-816897-4.00029-1.

Ghafari, R. *et al.* (2020) 'Processing-structure-property relationships of electrospun PLA-PEO membranes reinforced with enzymatic cellulose nanofibers', *Polymer Testing*, 81. doi: 10.1016/j.polymertesting.2019.106182.

Giammona, G., Palumbo, F. and Pitarresi, G. (2009) 'Method to produce hyaluronic acid functionalized derivatives and formation of hydrogels thereof.', *U.S.*, (US8858999B2), p. No pp. given.

Gilbert-Honick, J. *et al.* (2018) 'Engineering functional and histological regeneration of vascularized skeletal muscle', *Biomaterials*, 164, pp. 70–79. doi: 10.1016/j.biomaterials.2018.02.006.

Gomez-Florit, M. *et al.* (2020) 'Natural-Based Hydrogels for Tissue Engineering Applications', *Molecules (Basel, Switzerland)*, pp. 1–29. doi: 10.3390/molecules25245858.

Graney, P. L., Lurier, E. B. and Spiller, K. L. (2018) 'Biomaterials and Bioactive Factor Delivery Systems for the Control of Macrophage Activation in Regenerative Medicine', *ACS Biomaterials Science and Engineering*, 4(4), pp. 1137–1148. doi: 10.1021/acsbiomaterials.6b00747.

Hanumantharao, S. N. and Rao, S. (2019) 'Multi-Functional Electrospun Nanofibers from', *Fibers*, 7(66), pp. 1–35.

He, L. *et al.* (2013) 'Surface Modification of PLLA Nano-scaffolds with Laminin Multilayer by LbL Assembly for Enhancing Neurite Outgrowth a', pp. 1601–1609. doi: 10.1002/mabi.201300177.

Herberts, C. A., Kwa, M. S. G. and Hermsen, H. P. H. (2011) 'Risk factors in the development of stem cell therapy', *Journal of Translational Medicine*, 9, pp. 1–14. doi: 10.1186/1479-5876-9-29.

Highley, C. B., Prestwich, G. D. and Burdick, J. A. (2016) 'Recent advances in hyaluronic acid hydrogels for biomedical applications', *Current Opinion in Biotechnology*, 40, pp. 35–40. doi: 10.1016/j.copbio.2016.02.008.

Ismail, N. A. *et al.* (2019) 'Gellan gum incorporating titanium dioxide nanoparticles biofilm as wound dressing: Physicochemical, mechanical, antibacterial properties and wound healing studies', *Materials Science and Engineering C*, 103(April), p. 109770. doi: 10.1016/j.msec.2019.109770.

Ji, Y. *et al.* (2006) 'Electrospun three-dimensional hyaluronic acid nanofibrous scaffolds', *Biomaterials*, 27(20), pp. 3782–3792. doi: 10.1016/j.biomaterials.2006.02.037.

Jiang, T. *et al.* (2015) 'Electrospinning of polymer nanofibers for tissue regeneration', *Progress in Polymer Science*, 46, pp. 1–24. doi: 10.1016/j.progpolymsci.2014.12.001.

Jiang, W. *et al.* (2015) 'Incorporation of aligned PCL-PEG nanofibers into porous chitosan scaffolds improved the orientation of collagen fibers in regenerated periodontium', *Acta Biomaterialia*, 25, pp. 240–252. doi: 10.1016/j.actbio.2015.07.023.

Jin, G., Prabhakaran, Molamma P., *et al.* (2013) 'Controlled release of multiple epidermal induction factors through core-shell nanofibers for skin regeneration', *European Journal of Pharmaceutics and Biopharmaceutics*, 85(3), pp. 689–698. doi: 10.1016/j.ejpb.2013.06.002.

Jin, G., Prabhakaran, Molamma P, *et al.* (2013) 'Controlled release of multiple epidermal induction factors through core – shell nanofibers for skin regeneration', *European Journal of Pharmaceutics and Biopharmaceutics*, 85(3), pp. 689–698. doi: 10.1016/j.ejpb.2013.06.002.

Kansara, V. *et al.* (2019) 'Functionalized graphene nanosheets with improved dispersion stability and superior paclitaxel loading capacity', *Colloids and Surfaces B: Biointerfaces*, 173, pp. 421–428. doi: 10.1016/j.colsurfb.2018.10.016.

Kayaci, F. and Uyar, T. (2012) 'Electrospun zein nanofibers incorporating cyclodextrins', *Carbohydrate Polymers*, 90(1), pp. 558–568. doi: 10.1016/j.carbpol.2012.05.078.

Khalil, A. and Lalia, B. S. (2013) 'Electrospun metallic nanowires : Synthesis , characterization , and applications Electrospun metallic nanowires : Synthesis , characterization , and applications', (November). doi: 10.1063/1.4822482.

Van Kilsdonk, J. W. J. *et al.* (2013) 'An in vitro wound healing model for evaluation of dermal substitutes', *Wound Repair and Regeneration*, 21(6), pp. 890–896. doi: 10.1111/wrr.12086.

Kim, H. S. *et al.* (2018) 'Advanced drug delivery systems and artificial skin grafts for skin wound healing', *Advanced Drug Delivery Reviews*, p. #pagerange#. doi: https://doi.org/10.1016/j.addr.2018.12.014.

Kim, I. L. *et al.* (2013) 'Fibrous hyaluronic acid hydrogels that direct MSC chondrogenesis through mechanical and adhesive cues', *Biomaterials*, 34(22), pp. 5571–5580. doi: 10.1016/j.biomaterials.2013.04.004.

Kim, S. M. *et al.* (2013) 'The effects of dexamethasone on the apoptosis and osteogenic differentiation of human periodontal ligament cells', *Journal of Periodontal and Implant Science*, 43(4), pp. 168–176. doi: 10.5051/jpis.2013.43.4.168.

Kim, Y.-H. and Tabata, Y. (2015) 'Recruitment of mesenchymal stem cells and macrophages by dual release of stromal cell-derived factor-1 and a macrophage recruitment agent enhances wound closure', *Journal of Biomedical Materials Research Part A*, p. n/a-n/a. doi: 10.1002/jbm.a.35635.

Kitsara, M. *et al.* (2017) 'Fibers for hearts: A critical review on electrospinning for cardiac tissue engineering', *Acta Biomaterialia*, 48, pp. 20–40. doi: 10.1016/j.actbio.2016.11.014.

Koh, H. S. *et al.* (2008) 'Enhancement of neurite outgrowth using nano-structured scaffolds coupled

with laminin', *Biomaterials*, 29(26), pp. 3574–3582. doi: 10.1016/j.biomaterials.2008.05.014.

Kong, J. *et al.* (2018) 'Progress in Polymer Science Polymer-based composites by electrospinning : Preparation & functionalization with nanocarbons', *Progress in Polymer Science*, 86, pp. 40–84. doi: 10.1016/j.progpolymsci.2018.07.002.

Kurpinski, K. T. *et al.* (2010) 'The effect of fiber alignment and heparin coating on cell infiltration into nanofibrous PLLA scaffolds', *Biomaterials*, 31(13), pp. 3536–3542. doi: 10.1016/j.biomaterials.2010.01.062.

Lai, H. J. *et al.* (2014) 'Tailored design of electrospun composite nanofibers with staged release of multiple angiogenic growth factors for chronic wound healing', *Acta Biomaterialia*, 10(10), pp. 4156–4166. doi: 10.1016/j.actbio.2014.05.001.

Langer, R. and Vacanti, J. P. (1993) 'Tissue Engineering', *The Educational Forum*, 15(1), pp. 119–120. doi: 10.1080/00131725009342110.

Lehmann-horn, K. *et al.* (2014) 'Preparation of animal polysaccharides nanofibers by electrospinning and their potential biomedical applications Wen', *The Laryngoscope*, (August), pp. 2–31. doi: 10.1002/jbm.a.35187.

Lian, M. *et al.* (2019) 'Bi-layered electrospun nanofibrous membrane with osteogenic and antibacterial properties for guided bone regeneration', *Colloids and Surfaces B: Biointerfaces*, 176(October 2018), pp. 219–229. doi: 10.1016/j.colsurfb.2018.12.071.

Liao, Y. *et al.* (2018) 'Progress in Polymer Science Progress in electrospun polymeric nanofibrous membranes for water treatment : Fabrication , modification and applications', *Progress in Polymer Science*, 77, pp. 69–94. doi: 10.1016/j.progpolymsci.2017.10.003.

Lin, Y. J. *et al.* (2015) 'Stimulation of wound healing by PU/hydrogel composites containing fibroblast growth factor-2', *Journal of Materials Chemistry B*, 3(9), pp. 1931–1941. doi: 10.1039/c4tb01638f.

Liu, S. *et al.* (2014) 'NIR initiated and pH sensitive single-wall carbon nanotubes for doxorubicin intracellular delivery', *Journal of Materials Chemistry B*, 2(9), pp. 1125–1135. doi: 10.1039/c3tb21362e.

Luo, Y. *et al.* (2013) 'Carbon nanotube-incorporated multilayered cellulose acetate nanofibers for

tissue engineering applications', *Carbohydrate Polymers*, 91(1), pp. 419–427. doi: 10.1016/j.carbpol.2012.08.069.

Lutolf, M. P., Gilbert, P. M. and Blau, H. M. (2009) 'Designing materials to direct stem-cell fate', *Nature*, 462(7272), pp. 433–441. doi: 10.1038/nature08602.

Mahdavi, M. *et al.* (2016) 'Electrospinning of Nanodiamond-Modified Polysaccharide Nanofibers with Physico-Mechanical Properties Close to Natural Skins'. doi: 10.3390/md14070128.

Malafaya, P. B., Silva, G. A. and Reis, R. L. (2007) 'Natural-origin polymers as carriers and scaffolds for biomolecules and cell delivery in tissue engineering applications', *Advanced Drug Delivery Reviews*, 59(4–5), pp. 207–233. doi: 10.1016/j.addr.2007.03.012.

Manning, C. N. *et al.* (2013) 'Controlled delivery of mesenchymal stem cells and growth factors using a nanofiber scaffold for tendon repair', *Acta Biomaterialia*, 9(6), pp. 6905–6914. doi: 10.1016/j.actbio.2013.02.008.

Marinucci, L. *et al.* (2001) 'In Vitro Comparison of Bioabsorbable and Non-Resorbable Membranes in Bone Regeneration', *Journal of Periodontology*, 72(6), pp. 753–759. doi: 10.1902/jop.2001.72.6.753.

Martino, M. M. *et al.* (2009) 'Controlling integrin specificity and stem cell differentiation in 2D and 3D environments through regulation of fibronectin domain stability', *Biomaterials*, 30(6), pp. 1089–1097. doi: 10.1016/j.biomaterials.2008.10.047.

Mauro, N. *et al.* (2019) 'Near-Infrared, Light-Triggered, On-Demand Anti-inflammatories and Antibiotics Release by Graphene Oxide/Elecrospun PCL Patch for Wound Healing', *C — Journal of Carbon Research*, 5(4), p. 63. doi: 10.3390/c5040063.

Mauro, N. *et al.* (2020) 'A self-sterilizing fluorescent nanocomposite as versatile material with broad-spectrum antibiofilm features', *Materials Science and Engineering C*, 117(May). doi: 10.1016/j.msec.2020.111308.

Meinel, A. J. *et al.* (2012) 'Electrospun matrices for localized drug delivery: Current technologies and selected biomedical applications', *European Journal of Pharmaceutics and Biopharmaceutics*, 81(1), pp. 1–13. doi: 10.1016/j.ejpb.2012.01.016.

Mendes, A. C., Stephansen, K. and Chronakis, I. S. (2017) 'Electrospinning of food proteins and

polysaccharides', *Food Hydrocolloids*, 68, pp. 53–68. doi: 10.1016/j.foodhyd.2016.10.022.

Mesallati, H. and Tajber, L. (2017) 'Polymer/Amorphous Salt Solid Dispersions of Ciprofloxacin', *Pharmaceutical Research*, 34(11), pp. 2425–2439. doi: 10.1007/s11095-017-2250-z.

Metavarayuth, K. *et al.* (2016) 'Influence of Surface Topographical Cues on the Differentiation of Mesenchymal Stem Cells in Vitro', *ACS Biomaterials Science and Engineering*, 2(2), pp. 142–151. doi: 10.1021/acsbiomaterials.5b00377.

Miguel, S. *et al.* (2017) 'Electrospun Polycaprolactone/Aloe Vera_Chitosan Nanofibrous Asymmetric Membranes Aimed for Wound Healing Applications', *Polymers*, 9(12), p. 183. doi: 10.3390/polym9050183.

Miguel, S. P. *et al.* (2018) 'Electrospun polymeric nanofibres as wound dressings: A review', *Colloids and Surfaces B: Biointerfaces*, 169, pp. 60–71. doi: 10.1016/j.colsurfb.2018.05.011.

Miguel, Sónia P. *et al.* (2019) 'An overview of electrospun membranes loaded with bioactive molecules for improving the wound healing process', *European Journal of Pharmaceutics and Biopharmaceutics*, 139(January), pp. 1–22. doi: 10.1016/j.ejpb.2019.03.010.

Miguel, Sónia P *et al.* (2019) 'Production and characterization of electrospun silk fibroin based asymmetric membranes for wound dressing applications', *International Journal of Biological Macromolecules*, 121, pp. 524–535. doi: 10.1016/j.ijbiomac.2018.10.041.

Mitchell, G. R. and Tojeira, A. (2013) 'Role of Anisotropy in Tissue Engineering', *Procedia Engineering*, 59, pp. 117–125. doi: 10.1016/j.proeng.2013.05.100.

Mohammed, H. *et al.* (2019) 'Latest Progress in Electrospun Nanofibers for Wound Healing Applications', *ACS Applied Bio Materials*. doi: 10.1021/acsabm.8b00637.

Monteiro, N. *et al.* (2015) 'Antibacterial activity of chitosan nanofiber meshes with liposomes immobilized releasing gentamicin', *Acta Biomaterialia*, 18, pp. 196–205. doi: 10.1016/j.actbio.2015.02.018.

Moraes, R. da C. L. *et al.* (2020) 'Rheology of graphene oxide suspended in yield stress fluid', *Journal of Non-Newtonian Fluid Mechanics*, 286(March). doi: 10.1016/j.jnnfm.2020.104426.

Morgado, P. I., Aguiar-Ricardo, A. and Correia, I. J. (2015) 'Asymmetric membranes as ideal

wound dressings: An overview on production methods, structure, properties and performance relationship', *Journal of Membrane Science*, 490, pp. 139–151. doi: 10.1016/j.memsci.2015.04.064.

Moura, L. I. F. *et al.* (2013) 'Recent advances on the development of wound dressings for diabetic foot ulcer treatment - A review', *Acta Biomaterialia*, 9(7), pp. 7093–7114. doi: 10.1016/j.actbio.2013.03.033.

Muniz, F. W. M. G. *et al.* (2018) 'The effect of statins on periodontal treatment—a systematic review with meta-analyses and meta-regression', *Clinical Oral Investigations*, 22(2), pp. 671–687. doi: 10.1007/s00784-018-2354-9.

Nam, K., Kimura, T. and Kishida, A. (2008) 'Controlling coupling reaction of EDC and NHS for preparation of collagen gels using ethanol/water co-solvents', *Macromolecular Bioscience*, 8(1), pp. 32–37. doi: 10.1002/mabi.200700206.

Nguyen, C. T. *et al.* (2017) 'Preparation and in vitro evaluation of FGF-2 incorporated carboxymethyl chitosan nanoparticles', *Carbohydrate Polymers*, 173, pp. 114–120. doi: 10.1016/j.carbpol.2017.05.080.

Nguyen, L. T. H. *et al.* (2012) 'Electrospun poly(L-lactic acid) nanofibres loaded with dexamethasone to induce osteogenic differentiation of human mesenchymal stem cells', *Journal of Biomaterials Science, Polymer Edition*, 23(14), pp. 1771–1791. doi: 10.1163/092050611X597807.

Nguyen, T. K. *et al.* (2015) 'Iron oxide nanoparticle-mediated hyperthermia stimulates dispersal in bacterial biofilms and enhances antibiotic efficacy', *Scientific Reports*, 5(December), pp. 1–15. doi: 10.1038/srep18385.

Ogueri, K. S. and Laurencin, C. T. (2020) 'Nanofiber Technology for Regenerative Engineering', *ACS Nano*, 14, pp. 9347–9363. doi: 10.1021/acsnano.0c03981.

Pacelli, S. *et al.* (2017) 'Strategies to develop endogenous stem cell-recruiting bioactive materials for tissue repair and regeneration', *Advanced Drug Delivery Reviews*, 120, pp. 50–70. doi: 10.1016/j.addr.2017.07.011.

Palumbo, F. S. *et al.* (2015) 'In situ forming hydrogels of hyaluronic acid and inulin derivatives for cartilage regeneration', *Carbohydrate Polymers*, 122, pp. 408–416. doi: 10.1016/j.carbpol.2014.11.002.

Palumbo, F. S. *et al.* (2016) 'Hyaluronic Acid Derivative with Improved Versatility for Processing and Biological Functionalization', *Macromolecular Bioscience*, 16(10), pp. 1485–1496. doi: 10.1002/mabi.201600114.

Palumbo, F. S. *et al.* (2017) 'Spray dried hyaluronic acid microparticles for adhesion controlled aggregation and potential stimulation of stem cells', *International Journal of Pharmaceutics*, 519(1–2), pp. 332–342. doi: 10.1016/j.ijpharm.2017.01.033.

Palumbo, F. S. *et al.* (2018) 'Multifibrillar bundles of a self-assembling hyaluronic acid derivative obtained through a microfluidic technique for aortic smooth muscle cell orientation and differentiation', *Biomaterials Science*, 6(9), pp. 2518–2526. doi: 10.1039/c8bm00647d.

Palumbo, F. S. *et al.* (2020) 'Gellan gum-based delivery systems of therapeutic agents and cells', *Carbohydrate Polymers*, 229(September), p. 115430. doi: 10.1016/j.carbpol.2019.115430.

Pereira, R. F. *et al.* (2013) 'Advanced biofabrication strategies for skin regeneration and repair', *Nanomedicine*, 8(4), pp. 603–621. doi: 10.2217/nnm.13.50.

Pitarresi, G. *et al.* (2013) 'Medicated hydrogels of hyaluronic acid derivatives for use in orthopedic field', *International Journal of Pharmaceutics*, 449(1–2), pp. 84–94. doi: 10.1016/j.ijpharm.2013.03.059.

Qu, J. *et al.* (2013) 'Electrospun silk fibroin nanofibers in different diameters support neurite outgrowth and promote astrocyte migration', *Journal of Biomedical Materials Research - Part A*, 101 A(9), pp. 2667–2678. doi: 10.1002/jbm.a.34551.

Rahmati, M. *et al.* (2020) 'Electrospinning for tissue engineering applications', *Progress in Materials Science*, p. 100721. doi: 10.1016/j.pmatsci.2020.100721.

Rajasekaran, R. *et al.* (2020) 'Role of nanofibers on MSCs fate: Influence of fiber morphologies, compositions and external stimuli', *Materials Science and Engineering C*, 107(September 2019). doi: 10.1016/j.msec.2019.110218.

Rajeshwari, H. R. *et al.* (2019) 'Local drug delivery systems in the management of periodontitis: A scientific review', *Journal of Controlled Release*. Elsevier, pp. 393–409. doi: 10.1016/j.jconrel.2019.06.038.

Ricotti, L. *et al.* (2012) 'Proliferation and skeletal myotube formation capability of C2C12 and H9c2

cells on isotropic and anisotropic electrospun nanofibrous PHB scaffolds', *Biomedical Materials*, 7(February 2014). doi: 10.1088/1748-6041/7/3/035010.

Rwei, S. P. and Huang, C. C. (2012) 'Electrospinning PVA solution-rheology and morphology analyses', *Fibers and Polymers*, 13(1), pp. 44–50. doi: 10.1007/s12221-012-0044-9.

Saghazadeh, S. *et al.* (2018) 'Drug delivery systems and materials for wound healing applications', *Advanced Drug Delivery Reviews*, 127, pp. 138–166. doi: 10.1016/j.addr.2018.04.008.

Santos, B. F. E. *et al.* (2017) 'Local application of statins in the treatment of experimental periodontal disease in rats', *Journal of Applied Oral Science*, 25(2), pp. 168–176. doi: 10.1590/1678-77572016-0149.

Scaffaro, R., Gulino, F. E. and Lopresti, F. (2020) 'Structure–property relationship and controlled drug release from multiphasic electrospun carvacrol-embedded polylactic acid/polyethylene glycol and polylactic acid/polyethylene oxide nanofiber mats', *Journal of Industrial Textiles*, 49(7), pp. 943–966. doi: 10.1177/1528083718801359.

Schillaci, D. *et al.* (2010) 'Pyrrolomycins as potential anti-staphylococcal biofilms agents', *Biofouling*, 26(4), pp. 433–438. doi: 10.1080/08927011003718673.

Selcan Gungor-Ozkerim, P. *et al.* (2014) 'Incorporation of growth factor loaded microspheres into polymeric electrospun nanofibers for tissue engineering applications', *Journal of Biomedical Materials Research - Part A*, 102(6), pp. 1897–1908. doi: 10.1002/jbm.a.34857.

Séon-Lutz, M. *et al.* (2019) 'Electrospinning in water and in situ crosslinking of hyaluronic acid / cyclodextrin nanofibers: Towards wound dressing with controlled drug release', *Carbohydrate Polymers*, 207, pp. 276–287. doi: 10.1016/j.carbpol.2018.11.085.

Shan, Y. H. *et al.* (2015) 'Silk fibroin/gelatin electrospun nanofibrous dressing functionalized with astragaloside IV induces healing and anti-scar effects on burn wound', *International Journal of Pharmaceutics*, 479(2), pp. 291–301. doi: 10.1016/j.ijpharm.2014.12.067.

Sheikholeslam, M. *et al.* (2018) 'Biomaterials for Skin Substitutes', *Advanced Healthcare Materials*, 7(5), pp. 1–20. doi: 10.1002/adhm.201700897.

Shenoy, S. L. *et al.* (2005) 'Role of chain entanglements on fiber formation during electrospinning of polymer solutions: Good solvent, non-specific polymer-polymer interaction limit', *Polymer*,

46(10), pp. 3372–3384. doi: 10.1016/j.polymer.2005.03.011.

Shi, R. *et al.* (2018) 'Antimicrobial gelatin-based elastomer nanocomposite membrane loaded with ciprofloxacin and polymyxin B sulfate in halloysite nanotubes for wound dressing', *Materials Science and Engineering C*, 87(September 2017), pp. 128–138. doi: 10.1016/j.msec.2018.02.025.

Shin, S. R. *et al.* (2016) 'Graphene-based materials for tissue engineering', *Advanced Drug Delivery Reviews*, 105, pp. 255–274. doi: 10.1016/j.addr.2016.03.007.

Shu, X. Z. *et al.* (2002) 'Disulfide Cross-Linked Hyaluronan Hydrogels'. doi: 10.1021/bm025603c.

Souza, C. M. C. O. *et al.* (2014) 'Regeneration of skin tissue promoted by mesenchymal stem cells seeded in nanostructured membrane', *Transplantation Proceedings*, 46(6), pp. 1882–1886. doi: 10.1016/j.transproceed.2014.05.066.

Steel, E. M., Azar, J. Y. and Sundararaghavan, H. G. (2020) 'Electrospun hyaluronic acid-carbon nanotube nanofibers for neural engineering', *Materialia*, 9(July 2019). doi: 10.1016/j.mtla.2019.100581.

Stevens, L. R. *et al.* (2016) 'Tissue engineering with gellan gum', *Biomaterials Science*, 4(9), pp. 1276–1290. doi: 10.1039/c6bm00322b.

Stijnman, A. C., Bodnar, I. and Hans Tromp, R. (2011) 'Electrospinning of food-grade polysaccharides', *Food Hydrocolloids*, 25(5), pp. 1393–1398. doi: 10.1016/j.foodhyd.2011.01.005.

Sun, X. *et al.* (2014) 'BFGF-grafted electrospun fibrous scaffolds via poly(dopamine) for skin wound healing', *Journal of Materials Chemistry B*, 2(23), pp. 3636–3645. doi: 10.1039/c3tb21814g.

Tang, J. *et al.* (1994) 'Polymer and Ion Concentration Effects on Gellan Gel Strength and Strain', *Journal of Food Science*, 59(1), pp. 216–220. doi: 10.1111/j.1365-2621.1994.tb06934.x.

Thakkar, S. and Misra, M. (2017) 'Electrospun polymeric nanofibers: New horizons in drug delivery', *European Journal of Pharmaceutical Sciences*, 107(May), pp. 148–167. doi: 10.1016/j.ejps.2017.07.001.

Tsaryk, R. *et al.* (2017) 'Biological performance of cell-encapsulated methacrylated gellan gum-based hydrogels for nucleus pulposus regeneration', *Journal of Tissue Engineering and Regenerative Medicine*, 11(3), pp. 637–648. doi: 10.1002/term.1959.

Tsou, T. L. *et al.* (2005) 'Poly(2-hydroxyethyl methacrylate) wound dressing containing ciprofloxacin and its drug release studies', *Journal of Materials Science: Materials in Medicine*, 16(2), pp. 95–100. doi: 10.1007/s10856-005-5954-2.

Vashisth, P. *et al.* (2014) 'Process optimization for fabrication of gellan based electrospun nanofibers', *Carbohydrate Polymers*, 109, pp. 16–21. doi: 10.1016/j.carbpol.2014.03.003.

Vella, J. *et al.* (2015) 'A simple HPLC-UV method for the determination of ciprofloxacin in human plasma', *Journal of Chromatography B: Analytical Technologies in the Biomedical and Life Sciences*, 989, pp. 80–85. doi: 10.1016/j.jchromb.2015.01.006.

Wang, H. *et al.* (2020) 'A dual-targeted platform based on graphene for synergistic chemo-photothermal therapy against multidrug-resistant Gram-negative bacteria and their biofilms', *Chemical Engineering Journal*, 393(February), p. 124595. doi: 10.1016/j.cej.2020.124595.

Wang, H., Feng, Y. and Zhao, H. (2012) 'Electrospun Hemocompatible PU / Gelatin-Heparin Nanofibrous Bilayer Scaffolds as Potential Artificial Blood Vessels', *Macromolecular Research*, 20(4), pp. 347–350. doi: 10.1007/s13233-012-0012-7.

Wang, J. and Windbergs, M. (2017) 'Functional electrospun fibers for the treatment of human skin wounds', *European Journal of Pharmaceutics and Biopharmaceutics*, pp. 283–299. doi: 10.1016/j.ejpb.2017.07.001.

West, T. P., Strohfus, B. and Santiago, M. F. (2000) 'A colorimetric assay for gellan elaborated by Sphingomonas paucimobilis ATCC31461', *World Journal of Microbiology & Biotechnology*, 16, pp. 529–531. doi: 10.1023/A00138703.

Wu, C. *et al.* (2016) 'Nanofibrous asymmetric membranes self-organized from chemically heterogeneous electrospun mats for skin tissue engineering', *Biomedical Materials*, 11(3), p. 035019. doi: 10.1088/1748-6041/11/3/035019.

Xiao, L. *et al.* (2017) 'Enhanced Photothermal Bactericidal Activity of the Reduced Graphene Oxide Modified by Cationic Water-Soluble Conjugated Polymer', *ACS Applied Materials and Interfaces*, 9(6), pp. 5382–5391. doi: 10.1021/acsami.6b14473.

Xie, J. *et al.* (2009) 'Neurite Outgrowth on Nanofiber Scaffolds with Different Orders, Structures, and Surface Properties', *ACS Nano*, 3(5), pp. 1151–1159. doi: 10.1021/nn900070z.

Xu, R. *et al.* (2016) 'Controlled water vapor transmission rate promotes wound-healing via wound re-epithelialization and contraction enhancement', *Scientific Reports*, 6(April), pp. 1–12. doi: 10.1038/srep24596.

Xu, R. *et al.* (2017) 'Dual-delivery of FGF-2 / CTGF from Silk Fibroin / PLCL-PEO Coaxial Fibers Enhances MSC Proliferation and Fibrogenesis', *Scientific Reports*, (July), pp. 1–11. doi: 10.1038/s41598-017-08226-0.

Xue, J. *et al.* (2013) 'Engineering ear-shaped cartilage using electrospun fibrous membranes of gelatin/polycaprolactone', *Biomaterials*, 34(11), pp. 2624–2631. doi: 10.1016/j.biomaterials.2012.12.011.

Yang, S. *et al.* (2018) 'Preparation and characterization of antibacterial electrospun chitosan/poly (vinyl alcohol)/graphene oxide composite nanofibrous membrane', *Applied Surface Science*, 435, pp. 832–840. doi: 10.1016/j.apsusc.2017.11.191.

Yang, S., Zhang, X. and Zhang, D. (2019) 'Electrospun chitosan/poly (vinyl alcohol)/graphene oxide nanofibrous membrane with ciprofloxacin antibiotic drug for potential wound dressing application', *International Journal of Molecular Sciences*, 20(18). doi: 10.3390/ijms20184395.

Yang, Z. *et al.* (2010) 'Crystallization behavior of poly(ε-caprolactone)/layered double hydroxide nanocomposites', *Journal of Applied Polymer Science*, 116(5), pp. 2658–2667. doi: 10.1002/app.

Yin, Z. *et al.* (2015) 'Electrospun scaffolds for multiple tissues regeneration invivo through topography dependent induction of lineage specific differentiation', *Biomaterials*, 44, pp. 173–185. doi: 10.1016/j.biomaterials.2014.12.027.

Yuan, T. T. *et al.* (2018) 'Development of Electrospun Chitosan- Polyethylene Oxide / Fibrinogen Biocomposite for Potential Wound Healing Applications'.

Zhang, H. *et al.* (2013) 'Dual-delivery of VEGF and PDGF by double-layered electrospun membranes for blood vessel regeneration', *Biomaterials*, 34(9), pp. 2202–2212. doi: 10.1016/j.biomaterials.2012.12.005.

Zhang, W. *et al.* (2015) 'Vascularization of hollow channel-modified porous silk scaffolds with endothelial cells for tissue regeneration', *Biomaterials*, 56(August 2016), pp. 68–77. doi: 10.1016/j.biomaterials.2015.03.053.

Zhao, W. *et al.* (2017) 'Delivery of stromal cell-derived factor 1α for in situ tissue regeneration', *Journal of Biological Engineering*, 11(1), pp. 1–12. doi: 10.1186/s13036-017-0058-3.

Zomer Volpato, F. *et al.* (2012) 'Preservation of FGF-2 bioactivity using heparin-based nanoparticles, and their delivery from electrospun chitosan fibers', *Acta Biomaterialia*, 8(4), pp. 1551–1559. doi: 10.1016/j.actbio.2011.12.023.